Novel physics in two dimensional charge carrier structures

Lynass, Mark Ronald

Award date:
2006

Awarding institution:
University of Bath

Novel Physics in Two Dimensional Charge Carrier Structures

Anisotropic Magneto-transport at Landau-level Crossings in Aluminium Arsenide Quantum Wells and Coupled Two Dimensional Electron and Hole Systems

Submitted by Mark Ronald Lynass
for the degree of
Doctor of Philosophy
of the University of Bath
2006

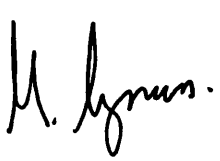

ProQuest LLC
789 East Eisenhower Parkway
P.O. Box 1346
Ann Arbor, MI 48106-1346

Abstract

This thesis discusses two projects. The first one concerns the growth and physics of high quality molecular beam epitaxy (MBE) grown AlAs wide quantum well (QW) structures. In contrast to conventional GaAs QW samples, electrons in AlAs are located at the symmetry X-point, they have large anisotropic effective masses (1.1 m_e for the longitudinal and 0.19 m_e for the transverse mass) and a large bulk Landé g-factor (1.96 in bulk and up to 10 in a QW). In perpendicular magnetic field the Zeeman energy is already comparable to the cyclotron energy, it is therfore easy to induce crossings between Landau levels with opposite spin and study interactions between them by rotating the sample in the magnetic field. Electrons in AlAs QWs can thus be used to study magnetism in reduced dimensions in a very controllable manner. This field is meanwhile known as quantum Hall ferromagnetism [1] and is rapidly developing.

At tilt angles where two Landau levels with opposite spin become degenerate in energy, a peak in the longitudinal resistance appears and the data reveal a large anisotropy of up to 400% i.e. if the direction of current flow with respect to the direction of the in-plane magnetic field is rotated by 90° then a factor of 4 change in the longitudinal resistance can be observed. The experiments carried out on Hall bar and van der Pauw samples oriented in various crystallographic directions indicate that the direction of the anisotropy depends on which two landau levels cross and on the in-plane B-field direction. Atomic force microscope (AFM) studies show an anisotropic surface roughness which surprisingly appears not to affect transport as previously thought [2]. In order to reveal details of ferromagnetic domain geometry within the sample, further studies were conducted on narrow Hall bars with various widths. These measurements show that below 3 μm the longitudinal resistance at the Landau level crossing strongly increases.

As a second topic, the preparation and study of closely-coupled two-dimensional electron and hole systems in semiconductor heterostructures using MBE and focused ion beam (FIB) techniques was conducted. Low density electron-hole (e-h) systems, in which the inter-layer and intra-layer particle separation is comparable, are of great interest because it is expected that the electrons and holes form spatially indirect excitons. These excitons are bosons and should, at low enough temperature undergo the 2D analogue of Bose-Einstein condensation, a topic of intense current interest (Nobel prize for physics 2001 [3]). The tech-

nological difficulties with the complex machinery used in this project has not allowed the fabrication of low density e-h systems with balanced carrier densities and independent contacts. Nevertheless, the principle of operation has been demonstrated and strongly coupled e-h systems with independent contacts and unbalanced densities have been prepared and characterised. Further optimisation of this system where the layer sequence is inverted is currently under investigation. Final samples have not yet been fabricated, but the optimisation and testing of the individual processing steps has been completed.

Contents

Introduction: Overview of the topics covered

In the research area of solid-state physics there have been many exciting breakthroughs over the past few decades, one of which was the discovery of the Integer Quantum Hall Effect (IQHE) by K. von Klitzing in the spring of 1980 and for which he was awarded the Noble prize in 1985 [4, 5, 6, 7]. Today, the von-Klitzing constant $R_{K-90} = h/e^2 = 25812,807\ \Omega$ is used by metrology institutes worldwide as a reference for the unit Ω since the effect exceeds the accuracy of the present SI system by nearly two orders of magnitude [8]. Apart from this very useful application, the discovery of the IQHE paved the way for further study and, in 1998, R.B. Laughlin, H.L. Stoermer and D.C. Tsui won the Nobel prize for their discovery and partial explanation of the Fractional Quantum Hall Effect [9]. Due to the richness of quantum Hall physics and the parallel developments of technology used to produce samples of increasing purity, a whole zoo of novel effects, some of which were theoretically predicted and some of which were completely unexpected, have been observed.

Many of the revolutionary discoveries have been due to technological advances, such as those seen since the development of molecular beam epitaxy (MBE). This thesis discusses two developments in the study of fundamental solid state physics through advanced MBE-grown semiconductor heterostructures. The first is the electronic transport in high quality AlAs quantum wells (QWs) and the second is the possible interaction effects between electrons and holes within strongly coupled 2D electron-hole systems.

AlAs quantum well structures and the quantum Hall ferromagnet

There have been reports of large anisotropic magneto-transport in two-dimensional electron systems (2DES) where two Landau levels with opposite spin are tuned to energetically coincide by adding an in-plane magnetic field component. The first of these papers utilised Si/SiGe heterostructures, where the opposite spin levels from two different valleys coincide [10]. This experiment considered transport in only one crystal direction. A further study of a high mobility $Al_xGa_{1-x}As$/-$GaAs/Al_xGa_{1-x}As$ wide QW structure with two occupied sub-bands has shown

similar effects [11]. Once more, transport was measured along only one crystal axis. Furthermore, theoretical investigations of these phenomena have been reported [2]. The anisotropic transport is ascribed to the formation of an anisotropic "ferromagnetic" domain structure, where current flows along the domain boundaries. In this thesis we discuss measurements on a 2DES where the electrons are confined to an AlAs QW using $Al_{0.45}Ga_{0.55}As$ barriers. In AlAs QWs with a width less than 55 Å, two in-plane valleys at the X-points of the Brillouin zone are occupied [12]. The large g-factor and thus the large Zeeman energy of AlAs X-point electrons makes this system very versatile, since many Landau level (LL) crossings from the same and from different valleys are achievable for moderate tilt angles. This system is thus of great interest because it provides an ideal system for studying ferromagnetism in two dimensions.

Coupled 2D electron-hole devices

Superconductivity was discovered by Onnes H.K. in 1911, three years after he liquefied Helium [13]. The origin of superconductivity remained a mystery until 1957, when Bardeen, Cooper and Schrieffer developed the BCS theory [14]. Cooper showed how two electrons in a superconductor could form a bound state despite their Coulombic repulsion by interacting with the lattice (the Cooper pair). Mott, in 1961, observed that electrons and holes under certain conditions will also form bound pairs (excitons) [15]. Since the total spin of an exciton is an integer and the attractive Coulomb interaction between electron and hole is much stronger than that of the phonon mediated electron-electron interaction, it is expected that a phase transition equivalent to Bose-Einstein condensation (BEC) will more readily occur. Despite the analogy with BCS theory [14], this phase was theoretically shown to be insulating. Subsequently, it was proposed that spatially separated electron-hole systems (i.e. indirect excitons) could form a superfluid condense through the 2D equivalent of the BEC phase transition . This superfluid state has not yet been directly observed. This project aims to study interaction effects in strongly coupled, low density 2D electron-hole systems, with the ultimate goal being the observation of the predicted superfluid phase.

Possibilities of realising two dimensional electron-hole systems in close proximity

It is possible to produce equilibrium two dimensional electron system (2DES) and two dimensional hole system (2DHS) in close proximity by way of InAs-GaSb heterostructures [16]. This is possible due to the large band offsets in these materials. Many experiments require separate contacts to each of the two layers and these contacts have not yet been realised in this material system. Further problems exist in these structures in that the intrinsic carrier densities (typically $> 5 \times 10^{-11}$ cm^{-2}) in the 2D layers are very high and they cannot be adjusted using gates. Since the ratio of inter-layer to intra-layer interaction needs to be large to observe coupling effects, lower carrier densities, which reduce intra-layer interactions, are more favourable and this is most likely the reason why coupling effects have so far not been observed in this system.

Another way of producing coupled electron-hole systems is by optical excitation of carriers in asymmetric double quantum wells (DQW) where the recombination life time is sufficiently long to let carriers thermalize but short enough to cause sufficient luminescence to make measurements. The application of an electric field over the DQW separates the charge carriers in space and allows the tuning of the luminescence lifetime. Indeed, recent luminescence measurements of electron-hole recombination have shown peculiar features [17, 18, 19, 20, 21] which were attributed to the existence of a condensed state, but this evidence is considered extremely controversial. Furthermore, the lack of separate electrical contacts to the electrons and the holes in this system make transport measurements impossible.

Using non-equilibrium techniques (i.e. using a interlayer bias to induce the desired band bending), it is possible to produce a 2DES coupled to a 2DHS in $Al_xGa_{1-x}As$/GaAs structures. A voltage needs to be applied between two layers that are separated by a (AlAs/GaAs superlattice) barrier which compensates the band bending between the p-doped and n-doped sides of the structure. The quality of the barrier material must be very high (i.e. leakage free), since the 2D systems only form when the large bias of order of the bandgap of the material, is applied. An additional difficulty is that the contacts to the bottom 2D system must overlap or be at least perfectly aligned with the barrier.

Outline of the thesis

The outline of the thesis is as follows. Part I is divided into three chapters; in the first one, background information is given about quantum mechanical band theory of 3D semiconductors, followed by a discussion of the Drude model. Next, the consequences of 2D confinement on the density of states without and with an applied perpendicular magnetic field are discussed. The present understanding of the integer quantum Hall effect is is given. In the second chapter the machinery used to fabricate the various 2D systems used in this thesis, is explained and a qualitative discussion of some of the growth details is given. Chapter three is devoted to the focused ion beam instrument that is used in the fabrication for electron-hole samples. The principles of operation are outlined and the fabrication of a custom build liquid metal ion source is described.

In part II, chapter 4 the AlAs bandstructure is described. AlAs is an indirect semiconductor with conduction band minima at the X-point of the Brioullin zone. These conduction band minima can be lower in energy than the Γ-point minima in $Al_xGa_{1-x}As$ for suitably chosen Aluminium content x. This allows the fabrication of AlAs quantum wells. The implications of the 2D confinement on the conduction band minima is discussed and it is explained why, in our wide AlAs quantum wells, the two in-plane valleys are occupied. Optimal growth sequence, sample layer structure and sample quality are determined and compared with results in literature. It is established that they are samples of superb quality. Next, the energy level diagram in a magnetic field is determined. From magnetoresistance measurements in tilted fields, the effective g-factor and the approximate valley splitting in the magnetic field are obtained. Chapter 5 studies the electronic transport in large magnetic fields at the tilt angle at which 2 levels cross. The various level energies determined in chapter four are used to identify the crossing levels. At the tilt angles at which two levels cross, a large spike in the longitudinal resistance is observed. It is thought that the spike is caused by backscattering across the Hall bar along so-called domain walls, i.e. the intersection that separates regions containing one of the two levels. Our most surprising observation is that the longitudinal transport is very anisotropic, i.e. it depends on the direction of current flow with respect to the direction of the in-plane magnetic field. Landau level crossings at ν=5, 6 and 7 are investigated and the results are compared with a theory that takes into account the non-flatness of the 2D system.

In part III our efforts to produce strongly coupled 2D electron-hole systems are described. Such systems are of interest, since at low and equal densities of the electrons and the holes, they are expected to form indirect excitons which at low temperatures should condense in a superfluid. The coupled 2D electron-hole systems are produced by a non-equilibrium technique, i.e. a bias of order of the bandgap of the GaAs, is applied between the p- and the n-side that are separated by a barrier. The FIB is used for structuring contacts to the lower 2D system during a MBE growth interrupt. In a first try, contacts to the lower 2D system were made by FIB implantation that selectively isolates certain areas in a lower p-doped layer. The sample design was optimised and samples from three wafers with high quality barrier were tested. Indeed, upon the application of a bias between the p- and the n-side of the sample, the simultaneous presence of a 2D hole gas and a 2D electron gas were established. Through transport measurements on the individual 2D gasses and through capacitance measurements, it was found out that low and equal densities could not be produced with this sample design. An unsuccessful attempt was made to use the FIB to directly write the p-contacts. Finally, it was decided to invert the structure, i.e. the 2DES is now the lower 2D gas. The focused ion beam with the home built liquid metal ion source was used to directly write the n-contacts during a growth interrupt. After overgrowth, this produced good contacts to the lower 2D electron system and it produced isolating barriers. Shallow contacts to the p-side of the sample were developed. The holes and the electrons were observed to accumulate at practically the same bias.

Part I

Background

Chapter 1

Two Dimensional Electron Systems and Quantum Hall Physics

Abstract

In bulk metals and semiconductors charge carriers are "free" to move in all three spatial directions. In a 2D system the electrons can only move in one plane and may not travel perpendicular to this plane. In this chapter we concentrate first on a review of the quantum mechanical band theory of 3D semiconductors, in order to describe their electromagnetic transport properties within the classical Drude theory. Afterwards we scale our description to 2D systems, where the transport is characterised by the Integer Quantum Hall Effect (IQHE), and we show why this effect cannot be explained by a classical theory. In the final section we will explain the present understanding of the IQHE.

1.1 Bulk semiconductor: The behaviour of charge carriers in the crystal lattice

The crystal structure of compound semiconductors, such as GaAs and AlAs, is the zincblende structure. This is similar to the diamond structure, but has a diatomic basis and therefore consists of two inter-penetrating face-center cubic (fcc) lattices. The offset vector between the two basis atoms is $(a_0/4)(\mathbf{x}+\mathbf{y}+\mathbf{z})$, where a_0 is the lattice constant and $\mathbf{x}$, $\mathbf{y}$, $\mathbf{z}$ are the orthogonal unit vectors in real space. It is often very useful to work in reciprocal space (or $\mathbf{k}$-space). The primitive reciprocal lattice vectors $\mathbf{b}_i$, $\mathbf{b}_j$ and $\mathbf{b}_k$ can be defined in terms of a given set of primitive lattice vectors of the fcc lattice in real space, $\mathbf{a}_i$,$\mathbf{a}_j$ and $\mathbf{a}_k$, by

$$\mathbf{b}_i = 2\pi \frac{(\mathbf{a}_j \times \mathbf{a}_k)}{V} \tag{1.1}$$

where i, j and k represent a cyclic permutation of the three indices 1, 2 and 3 and V is the volume of the primitive cell given by $(\mathbf{a}_1 \times \mathbf{a}_2) \cdot \mathbf{a}_3$. The reason for defining reciprocal lattice vectors in this way is because the electron (or hole) wave vector ($\mathbf{k}$) is a point in this reciprocal space.
The zincblende crystal structure with a set of primitive lattice vectors is shown in figure 1.1a). Fig 1.1b) shows the reciprocal lattice of the fcc lattice and the first Brillouin zone. The high symmetry points are denoted by Γ, X and L. The lines of high symmetry are labeled as Λ and Δ.

We will now discuss the use of quantum mechanics and the necessary approximations which are needed to calculate the electronic band structure. Firstly, the Hamiltonian of a perfect crystal can be expressed as

$$\begin{aligned}\mathscr{H} = &\sum_i \frac{p_i^2}{2m_i} + \sum_j \frac{P_j^2}{2M_j} + \frac{1}{2}\sum_{j'\neq j} \frac{Z_j Z_{j'} e^2}{4\pi\epsilon_0 |R_j - R_{j'}|} \\ &- \sum_{j,i} \frac{Z_j e^2}{4\pi\epsilon_0 |r_i - R_{j'}|} + \frac{1}{2}\sum_{i\neq i'} \frac{e^2}{4\pi\epsilon_0 |r_i - r_{i'}|},\end{aligned} \tag{1.2}$$

where p_i and P_j are the momentum operators of the ith electron and the jth nucleus respectively, m_i and M_j are the masses of the ith electron and the jth nucleus respectively. Z_j is the atomic number of the nucleus, r_i and R_j denote the positions of the ith electron and of the jth nucleus. The electronic charge is e and ϵ_0 is the dielectric constant in vacuum. Therefore, the first two terms of equation 1.2 describe the sum over the kinetic energies of the electron and nuclei

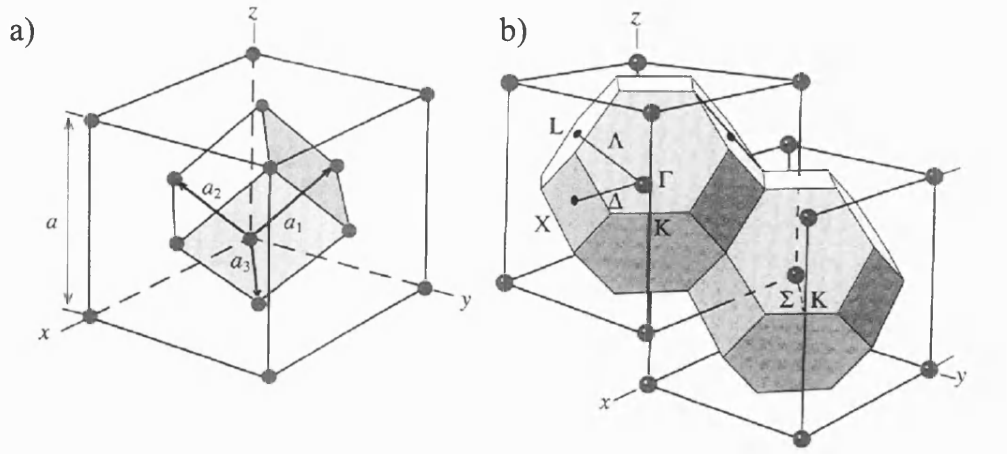

Figure 1.1: a) The fcc lattice showing a set of primitive lattice vectors. b) The reciprocal lattice of the fcc lattice and the first Brillouin zone. The high symmetry points are denoted by Γ, X and L. The lines of high symmetry are labeled as Λ and Δ.

respectively and the other three terms are the ion-ion, the ion-electron and the electron-electron interactions respectively.

To solve this Hamiltonian the assumptions of the Drude model will be used. Electrons which are located in completely filled orbitals are practically localised to the nucleus and therefore we can assume that these core electrons plus the nucleus form the *ion core*. We use the indices j, j' to denote the ion cores and i, i' to label the *valence electrons*, that is: electrons located in partially filled orbitals. If we further consider that the ions are much more massive than the electrons and therefore move much slower than electrons, then one can also assume that the ions are essentially stationary relative to the electrons. The above case corresponds to the Born-Oppenheimer approximation. The Hamiltonian of the perfect crystal in equation 1.2 can now be expressed as a sum of the three terms

$$\mathscr{H} = \mathscr{H}_{\text{ions}}(\mathbf{R}_j) + \mathscr{H}_{\text{e}}(\mathbf{r}_i, \mathbf{R}_{j0}) + \mathscr{H}_{\text{e-ion}}(\mathbf{r}_i, \delta\mathbf{R}_j), \tag{1.3}$$

where $\mathscr{H}_{\text{ions}}(\mathbf{R}_j)$ describes the ionic motion under the influence of both the ionic and electronic potential, $\mathscr{H}_{\text{e}}(\mathbf{r}_i, \mathbf{R}_{j0})$ is the Hamiltonian for electrons with the ions frozen in their equilibrium position $\mathbf{R}_{j0}$ and $\mathscr{H}_{\text{e-ion}}$ describes the electron-ion interaction. Since we will be looking at low temperature, the term of greatest

importance is that of the electron Hamiltonian, given by

$$\mathscr{H}_{\mathrm{e}} = \sum_i \frac{p_i^2}{2m_i} - \sum_{i,j} \frac{Z_{\mathrm{core}} e^2}{4\pi\epsilon_0 |r_i - R_{j0}|} + \frac{1}{2} \sum_{i \neq i'} \frac{e^2}{4\pi\epsilon_0 |r_i - r_{i'}|} \,. \tag{1.4}$$

If we assume that every electron experiences the same average potential $V(r)$, then the mean field approximation can be used, so that

$$\mathscr{H}_{1\mathrm{e}} \Psi_n(r) = \left(\frac{p^2}{2m} + V(r) \right) \Psi_n(r) = E_n \Psi_n(r) \,, \tag{1.5}$$

where $\mathscr{H}_{1\mathrm{e}}$ is the one-electron Hamiltonian, $\Psi_n(r)$ is the electron wave function and E_n is the electron energy in eigenstate n. To solve this for E_n, we need to know the potential $V(r)$. This can be obtained from first principles, however it is often obtained using semi-empirical methods. The calculation is still not a trivial matter and further simplification can be made, using symmetry arguments. The invariance of semiconductor crystals under certain translations, rotations and reflections helps us to reduce the complexity of band structure calculations.
A powerful tool to solve the Schrödinger equation 1.5 is given by the Bloch theorem. This theorem states that an eigenfunction of the Schrödinger equation for a periodic potential is given by the product of a plane wave $e^{ik \cdot r}$ times a function $u_k(k, r)$, as

$$\Psi_k(r) = e^{i(k \cdot r)} u_k(k, r), \tag{1.6}$$

where $u_k(k, r + a_0) = u_k(k, r)$ (i.e. $u_k(k, r)$ has the same periodicity of the lattice potential).
The relation between the crystal momentum k and the obtained eigenenergy $E(k)$ is known as the dispersion relation or the electronic band structure. An example of a plot of the dispersion relation, calculated via the pseudopotentials method, is shown in figure 1.2. There, the energy bands are plotted as a function of the wavevector $\vec{k}$; on the x-axis some specific values k are indicated, as $L, \Sigma, \Gamma, ...$ These values, already introduced in figure 1.1b, are defined as points and lines of high symmetry. As one can see from the figure, the same band energy might have several minima or maxima depending on the value of the wavevector. GaAs is a direct semiconductor, i.e. the primary maximum of the valence band and the primary minimum of the conduction band lie at the same wavevector.

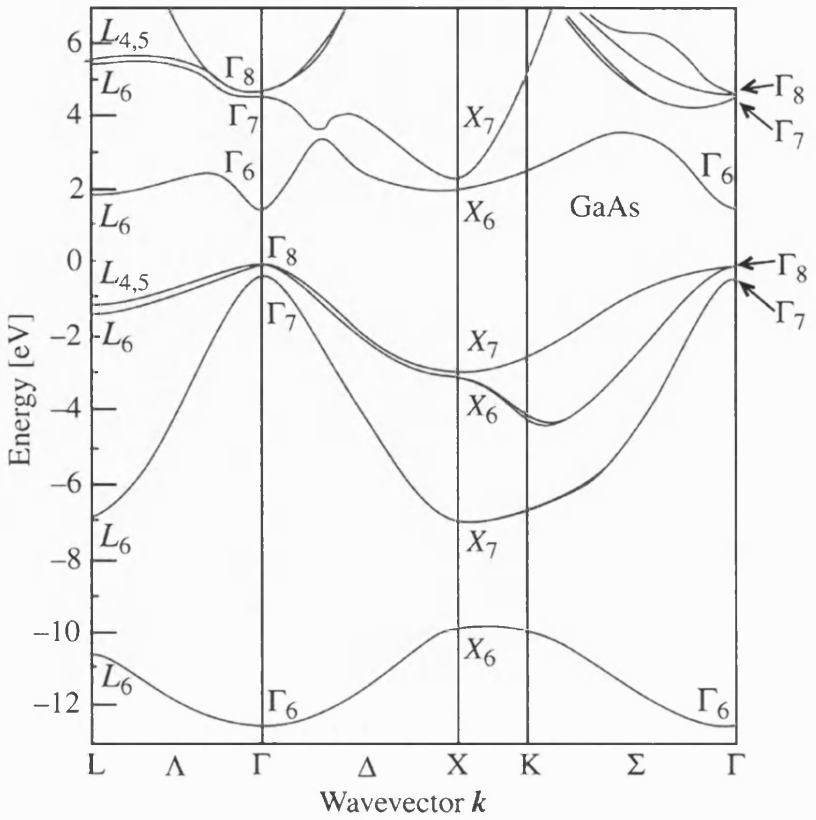

Figure 1.2: The electronic band structure for GaAs calculated using the pseudopotentials method. From this plot we can determine some of the important parameters which are involved in electronic transport through such a periodic lattice.

1.2 Reducing the dimensionality: From a bulk semiconductor to a two-dimensional electron system

Whenever the size of a bulk material becomes comparable to the wavelength of the electrons in its conduction band, the spatial confinement affects the system and quantum mechanical effects become predominant in the physics occurring in the system (quantum size effect). The consequences of this change to the geometry are, as we shall see, very profound and the resulting physics has made a large impact on semiconductor research.

In a 2D system with confinement in the z-direction (via infinite potential bar-

riers), the z-component of the wave vector will only have some fixed values, corresponding to different subband energies. Simultaneously the motion in the xy-plane is unrestricted. Taking k_x and k_y to be the components of the 2D vector $\mathbf{k}$ and plotting the allowed values of this vector produces a simple square lattice with sides of $2\pi/L$, where L is the length and the width of the 2D plane. The area of $\mathbf{k}$-space per $\mathbf{k}$-state is therefore $(2\pi/L)^2$. The number of allowed $\mathbf{k}$-states contained in the annulus with radii of k and $k + dk$ is then given by

$$g(k)\,\mathrm{d}k = \frac{2\pi k\,\mathrm{d}k}{(2\pi/L)^2} = \frac{L^2 k\,\mathrm{d}k}{2\pi}\,. \tag{1.7}$$

The energies of these states can be written as

$$\varepsilon = \frac{\hbar^2 k^2}{2m_e} + E_n\,, \tag{1.8}$$

where $\hbar$ is Planck's constant divided by 2π, m_e is the electron "effective" mass and

$$E_n = \frac{n^2 h^2}{8m_e d^2}\,, \tag{1.9}$$

where d is the width of the quantum well and n is the subband index. The density of states (DOS) per unit energy range $g(\varepsilon)$ in unit area is given by

$$g(\varepsilon)\mathrm{d}\varepsilon = 2g(k)\mathrm{d}k = \frac{m_e}{\pi\hbar^2}\mathrm{d}\varepsilon\,, \tag{1.10}$$

where the factor two arises from the two possible spin states of the electron. In figure 1.3 the density of states of a 2D system is plotted as a solid line as a function of the energy ε; since, as shown by equation 1.10, $g(\varepsilon)$ is independent of ε, the plot consists of a series of steps. The values E_n are defined as bound state energies. As comparison, in the figure the 3D case is also shown as a dotted line. As the width of the quantum well increases, the energies of the bound states become more closely spaced until finally the density of states increases with the square root of the energy as displayed by 3D electrons.

A 2DES can be experimentally obtained at the interface of a GaAs/AlGaAs heterojunction, as the one shown in figure 1.4. In fact, when GaAs and AlGaAs are put together, an offset in the conduction band bottom is formed. Doping AlGaAs with Si as donors, electrons from the donors find energetically favourable levels in the GaAs conduction band. However, since they are still attracted by the positive charge of the ionised Si donors, they accumulate close to the GaAs/AlGaAs interface. As the result, the electrons feel a triangular shaped

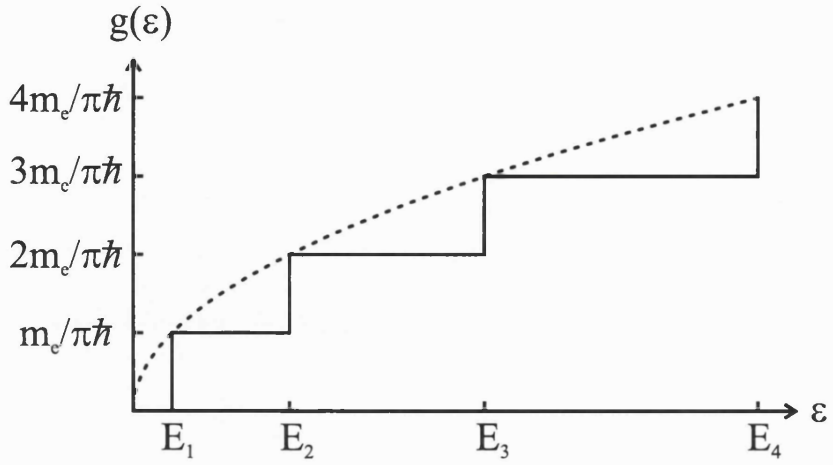

Figure 1.3: The density of states of a 2D system (solid line) consists of a series of steps. This is compared with the 3D case (dotted line) which shows a smooth monotonic increase. E_n are the bound state energies in 2D.

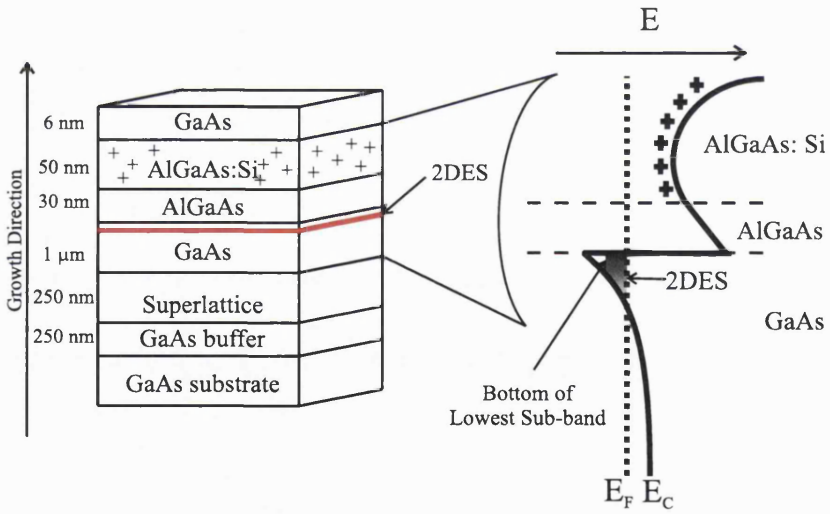

Figure 1.4: On the left side: Layer sequence of a typical modulation-doped GaAs/ $Al_{0.33}Ga_{0.67}As$ heterostructure; please note that the layers thickness are not shown to scale. On the right side: Sketch of the energy position of the conduction band minimum E_C through the layers. The Fermi level is denoted as E_F. The plus signs indicate the energetic position of the holes left behind by the electrons accumulated in the 2DES.

confining potential perpendicular to the layers' planes. Since the confining is so strong, the electrons are restricted to a thickness of a few tens of nanometers, which is comparable to the Fermi wavelength of the electron system.
The mobility of conduction band electrons in GaAs can be very high. However, if the electrons are provided by doping then the mobility is reduced due to scattering by ionised donors. This problem is partly overcome by putting the donors in a thin layer of $Al_xGa_{1-x}As \approx 500$ Å situated 300-600 Å away from the GaAs. The charge carriers are thus spatially separated from the donor atoms and therefore the mobility remains high.

1.3 The Hall effect: From classical to quantum theory

The history of the Hall effect goes back to a mistake made by Maxwell in his "Treatise on electricity and magnetism" [22]. Maxwell stated that "it must be carefully remembered that the mechanical force which urges a conductor... acts, not on the electric current, but on the conductor which carries it." Later, whilst studying a course on Maxwell's findings, Edwin Hall asked his professor Henry Rowland what he thought of Maxwell's statement [23]. Rowland's reply was that he "doubted the truth of Maxwell's statement" and that he had even tried an unsuccessful experiment to prove it. Rowland suggested to Hall that he should repeat the experiment but replace the conducting bar with a thin gold leaf film, hoping that this optimised setup would compensate for the weak magnetic field which was available in those days. The experiment was a success and in 1879 Edwin Hall discovered that, when a current carrying conductor is placed in a magnetic field, a voltage is generated in a direction perpendicular to both the current and the applied magnetic field.
Figure 1.5 shows a Hall bar indicating current I, magnetic field B and measurement positions of V_{xy} and V_{xx}. The underlying principle of the Hall effect is the Lorentz force. When a charge moves along a direction perpendicular to an applied magnetic field, it experiences a force orthogonal to its direction of motion and the magnetic field direction. When a constant current I is flowing in the sample in the x-direction, the charge carriers drift in the y-direction. However, the carriers cannot move very far in the y-direction before running up against the side of the bar. As they accumulate there, an electric field builds up that opposes

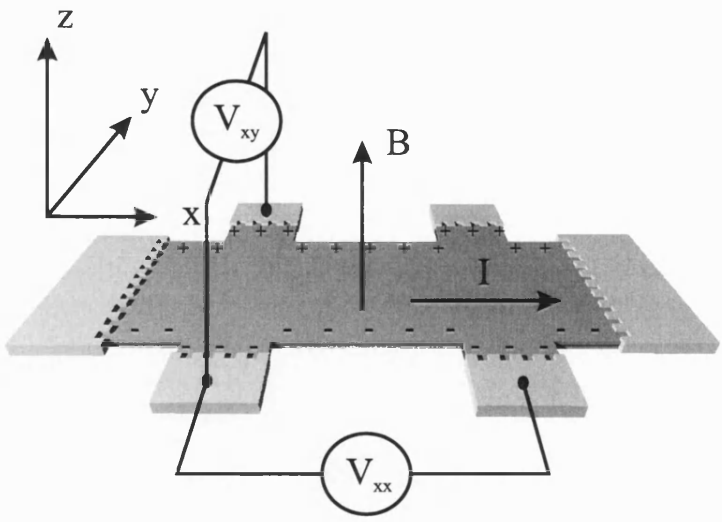

Figure 1.5: Diagram of a Hall bar indicating current I, magnetic field B and measurement positions of V_{xy} and V_{xx}

their motion and further accumulation. In equilibrium this electric field (Hall field) balances the Lorentz force. The voltage across the bar at equilibrium is V_{xy} (Hall voltage) and its magnitude is equal to IB/qnd, where I is the current, B is the magnetic field, d is the sample thickness, q is the charge of the carrier and n the bulk carrier density. Conventionally the sheet density $n_s = nd$ is used. In semiconductors the charge carriers can be positive or negative and therefore the polarity of the Hall voltage for n-type materials is opposite to that for p-doped semiconductors.

More recent technological developments allow lower temperatures and higher magnetic fields than in Hall's time. These conditions brought therefore to the breakdown of the classical theory underlying the Hall effect, opening the way to the experimental observation of purely quantum mechanical properties of the matters.
Let us start from the quantum theory: the equation of motion of a free electron in an uniform magnetic field is

$$-\frac{\hbar^2}{2m}\left(\vec{\nabla} - \frac{e}{i\hbar c}\vec{A}\right)^2 \psi = E_n(k_z)\psi\,, \tag{1.11}$$

where n is an integer. Applying the symmetric gauge, where $A_x = -\frac{1}{2}By$ and $A_y = \frac{1}{2}Bx$ (i.e. $\nabla \times \vec{A} = \vec{B} = (0, 0, B)$), the electron motion in the z-direction is

separated by the one in the xy-plane, so that

$$\psi(x,y,z) = \psi(x,y)\psi(z) = \psi(x,y)\frac{1}{\sqrt{L}}e^{ik_z z}\,. \tag{1.12}$$

The obtained Hamiltonian is therefore

$$\begin{aligned}\mathscr{H} &= \left(-\frac{\hbar^2}{2m}\frac{\partial^2}{\partial z^2}\right) + \frac{\left(i\hbar\partial_x + \frac{e}{2c}By\right)^2}{2m} + \frac{\left(i\hbar\partial_y + \frac{e}{2c}Bx\right)^2}{2m} \\ &= \frac{p_z^2}{2m} + \frac{p_x^2}{2m} + \frac{p_y^2}{2m} + \frac{e^2}{8c^2m}B^2\left(x^2+y^2\right) - \frac{eB}{2cm}(xp_y - yp_x)\,. \end{aligned} \tag{1.13}$$

Considering then the cylindrical coordinates (r,φ,z), the Hamiltonian becomes

$$\mathscr{H} = \frac{p_z^2}{2m} + \frac{1}{2m}\left(\frac{1}{r}\frac{\partial}{\partial r}\left(r\frac{\partial}{\partial r}\right) + \frac{1}{r^2}\frac{\partial^2}{\partial\varphi^2}\right) + \frac{m}{8}\omega_c^2 r^2 + i\hbar m\omega_c\frac{\partial}{\partial\varphi}\,, \tag{1.14}$$

where $\omega_c = \frac{eB}{mc}$ is the so-called cyclotron frequency. Once again, the electronic wavefunction can be factorised as

$$\psi(r,\varphi,z) = f(r)\psi(\varphi)\psi(z) = \frac{1}{\sqrt{2\pi}}f(r)e^{-il\varphi}e^{-ik_z z} \tag{1.15}$$

and the Schrödinger equation is now $\mathscr{H}f(r) = Ef(r)$. Defining

$$R(u) = \sqrt{u}f\left(\sqrt{\frac{2\hbar}{m\omega_c}}u\right)\,, \tag{1.16}$$

where $u = \frac{m\omega_c}{2\hbar}r^2$, the Schrödinger equation becomes

$$R'' + \left(\frac{\beta}{u} + \frac{1-l^2}{4u^2} - \frac{1}{4}\right)R = 0\,, \tag{1.17}$$

where

$$\beta = \frac{1}{\hbar\omega_c}\left(\varepsilon - \frac{\hbar^2 k_z^2}{2m}\right) + \frac{l}{2}\,. \tag{1.18}$$

This equation is now solvable and gives

$$R(u) = e^{-\frac{u}{2}}u^{\frac{|l|}{2}}\,\mathrm{F}\left(-n, |l|+1, u\right)\,, \tag{1.19}$$

where $n = \beta - \frac{1}{2}(|l|+1) \geq 0$ and F is the hypergeometrical equation. Converting

back this result in terms of $f(r)$, one obtains

$$f(r) = e^{-\frac{m\omega_c}{4\hbar}r^2}\left(\frac{m\omega_c}{2\hbar}r^2\right)^{\frac{|l|+1}{2}}\frac{n!l!}{(n+|l|)!}\mathrm{L}_n^{|l|}\left(\frac{m\omega_c}{2\hbar}r^2\right), \tag{1.20}$$

where $\mathrm{L}_n^{|l|}$ is a Laguerre polynomial.
Finally, the eigenenergies of an electron moving freely in an uniform magnetic field are

$$E_n = \frac{\hbar^2 k_z^2}{2m} + \hbar\omega_c\left(n + \frac{1}{2} + \frac{1}{2}|l| - \frac{1}{2}l\right), \tag{1.21}$$

where $n = 0, 1, 2, ...$ and $l = 0, \pm1, \pm2, ...$ In the case of $l \geq 0$, the energy levels are given as

$$E_n(k_z) = \frac{\hbar^2 k_z^2}{2m} + \hbar\omega_c\left(n + \frac{1}{2}\right) \tag{1.22}$$

and they are known as Landau levels, where n is defined as the Landau level index. Adding the Zeeman term in order to take into account also the electron spin, one can finally have

$$E_n(k_z) = \frac{\hbar^2 k_z^2}{2m} + \hbar\omega_c\left(n + \frac{1}{2}\right) \pm \frac{1}{2}\mathrm{g}^*\mu_B B_{\mathrm{tot}}, \tag{1.23}$$

where g^* is the effective Landé g-factor, μ_B is the Bohr magneton and B_{tot} the total magnetic field.

Whenever a large magnetic field is applied to a Hall bar containing a 2DES at low temperature, it is indeed possible to observe the quantisation of these energy levels. The experimental results are therefore very different from the predictions of the classical Drude model [24]. In the Drude model the longitudinal resistance ρ_{xx} is given by

$$\rho_{xx} = \frac{m_e}{n_s e^2 \tau} \tag{1.24}$$

and the Hall resistance ρ_{xy} by

$$\rho_{xy} = \frac{B}{n_s e}, \tag{1.25}$$

where τ is the average time occurring between two consecutive scattering events and n_s is the carrier density. Those equations would imply then that ρ_{xx} is a function that does not depend on the B-field and, on the other hand, ρ_{xy} depends linearly on the B-field. On the contrary, looking for example at figure 1.6, the experimental measurements show that the transverse resistivity ρ_{xy} of a 2DES

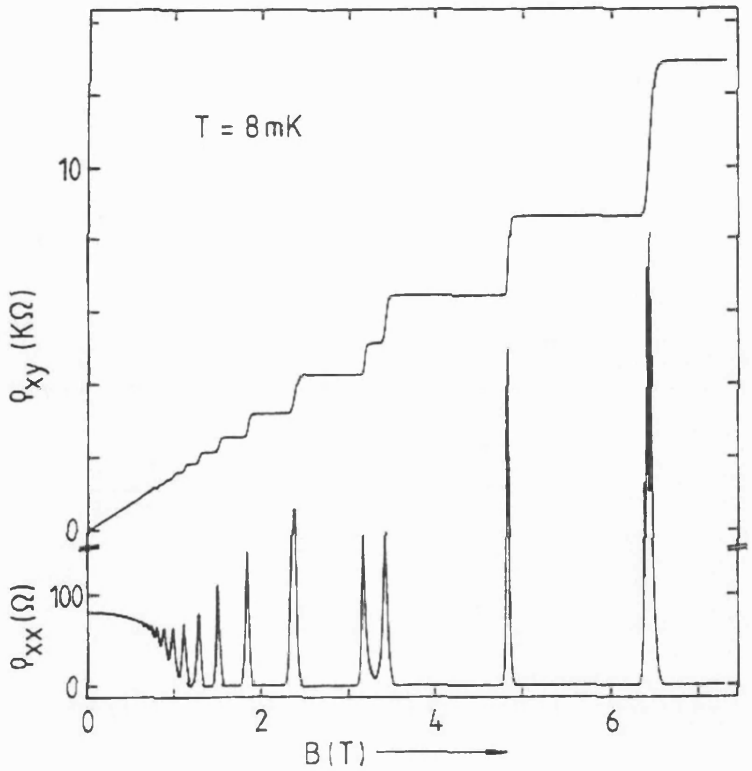

Figure 1.6: In high fields, ρ_{xy} increases in steps. Between the steps ρ_{xy} equals h/ie^2. In the region where ρ_{xy} is constant ρ_{xx} approaches zero [25].

(which is a measure of the Hall effect) in the high field region increases in a series of steps producing the so-called quantised Hall plateaux.
The value of ρ_{xy} at the plateau sections is a fractional multiple of an universal constant and is given by

$$\rho_{xy} = -\frac{h}{ie^2}, \tag{1.26}$$

where i is an integer and equal to the number of filled Landau levels below the Fermi energy. The longitudinal resistivity ρ_{xx} vanishes in the field region of these plateaux.

1.4 Electrical transport in the quantum Hall regime

To understand the existence of the quantised Hall effect, the single-electron picture that led to equation 1.22 is no longer sufficient; one must further take into

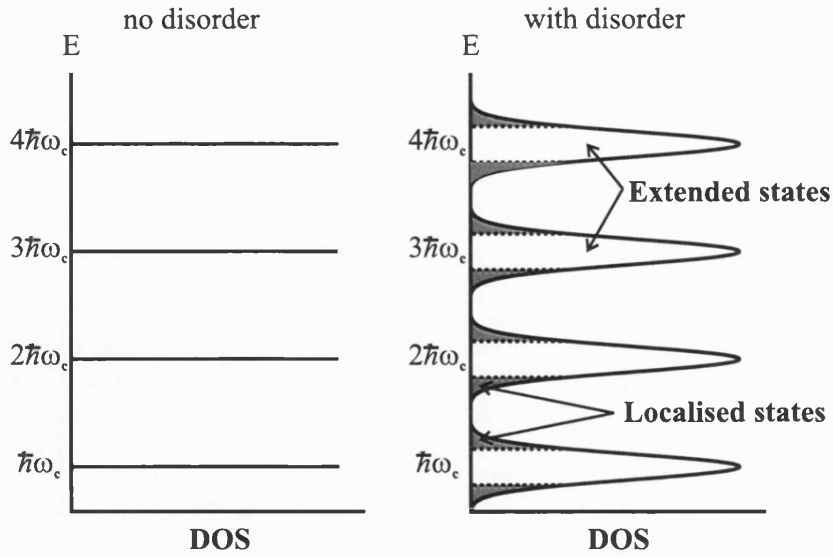

Figure 1.7: On the left are shown the Landau levels in an ideal sample with no disorder. On the right, the levels are broadened by the presence of disorder, leading to the formation of so-called localised and extended states. As the Fermi level passes through the extended states, the value of ρ_{xx} increases.

account the presence of disorder and Coulomb interactions.

In fact, the eigenfunctions obtained from equation 1.22 are highly localised around a semiclassical circular orbit of radius of the magnetic length l_B. The electron centers of orbit are in principle free to move, but normally an electric field would be needed to induce a current which will exist only if the electron wavefunctions become delocalised. The potential profile arising from the remote impurities, dopant atoms and Coulombic scattering broadens the Landau levels, as shown in figure 1.7. One distinguishes between two types of states: The extended states occupy a region close to the original Landau level energy and the localised states occupy the regions in between.

Since, in 2D systems, the Fermi energy depends linearly on the electron density and since the filling factor, in turn, depends on both the magnetic field and electron density, sweeping the magnetic field affects the value of the Fermi energy with respect to the filling factor. The Fermi energy as a result moves through the ladder scheme of the DOS diagram shown in figure 1.7, crossing regions of extended and localised states where the current either can or cannot flow. This picture explains the appearance of the plateaux in ρ_{xy} since as the density is increased (or as magnetic field is decreased) the localised states gradually fill up while the density of the extended states remains constant. For these densities (or magnetic field intervals) ρ_{xy} also remains constant and ρ_{xx} vanishes. Further-

more, Laughlin showed that, if the extended states are fully occupied, they carry the exact current to give equation 1.26 [26].

A good picture to describe this behaviour used to be that of current carrying edge states. The edge states originate from the assumption that, due to the spatial confining potential at the sample borders, the whole energy band structure of the 2DES is bent at its edge. Consequentially, the Landau levels are also bent and therefore they cross the Fermi energy. The point of intersection of the Landau and the Fermi level forms the position of the edge channel. The number of edge states is equal to the number of Landau levels below the Fermi energy and electrons with different Landau level index n and spin orientation move along different equipotential lines. This naive single-particle picture treats transport in terms of transmission and reflection matrices. This picture, however, fails to account for electron screening and its modification in strong magnetic fields.

The effect of screening was addressed qualitatively by Beenakker [27] and Chang [28] and then quantitatively by Shkloviskii and Chklovskii [29, 30, 31]. In order to explain the Quantum Hall Effect, the Thomas-Fermi approximation (TFA) was applied to the edge regions of the 2DES. The main hypothesis used here is that the confining potential at the edges $V(\vec{r})$ varies smoothly in the plane of the 2DES, so that its characteristic depletion length is much larger than the magnetic length l_B. In order to calculate the electron sheet density n_s, one has to consider

- the Poisson equation, linking the electron concentration to the electrostatic potential $\phi(\vec{r})$, and
- that the electrochemical potential has to be constant,

$$\mu^{\mathrm{elch}} = \mu^{\mathrm{ch}}(\vec{r}) - e\phi(\vec{r}) = \text{constant}\,, \tag{1.27}$$

  where the local chemical potential is a function of the local electron concentration $\mu^{\mathrm{ch}}(\vec{r}) = \mu^{\mathrm{ch}}(n_s(\vec{r}))$.

The electron sheet density obtained is

$$n_s(\vec{r}) = \int d\varepsilon\, D(\varepsilon)\, f\left(\frac{\varepsilon + V(\vec{r}) - \mu^{\mathrm{elch}}}{k_{\mathrm{B}}T}\right)\,, \tag{1.28}$$

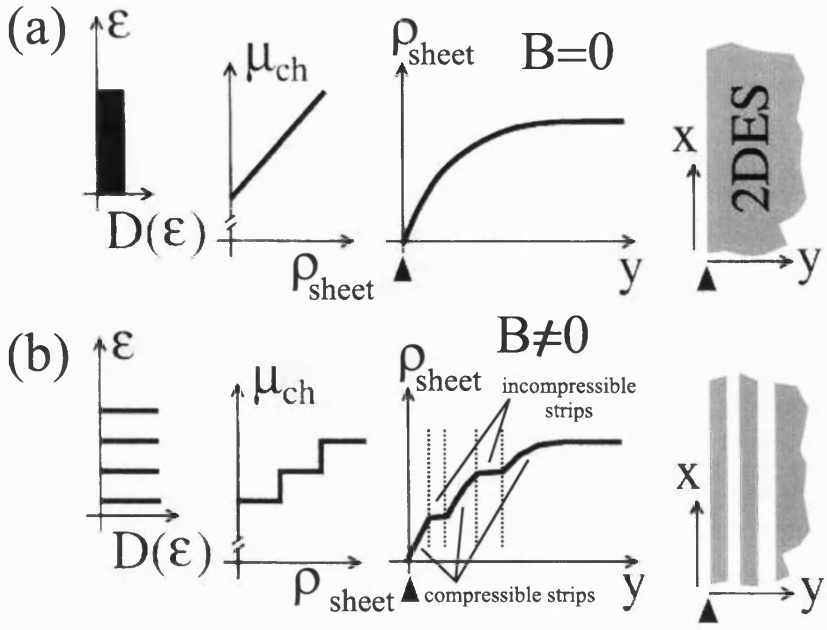

Figure 1.8: Schematic diagrams of the density of states $D(\varepsilon)$, the chemical potential $\mu^{\rm ch}$ and the electron sheet density $\rho(y)$. In (a) there is the case of zero magnetic field; in (b) the ones for B-field applied perpendicularly to the 2DES (*From* [32]).

where $f(\varepsilon) = [1 + e^(\varepsilon)]^{-1}$ is the Fermi function and

$$D(\varepsilon) = \frac{1}{2\pi l_B^2} \sum_{j=0}^{\infty} \delta\Big(E - (\hbar\omega_c(j + \tfrac{1}{2}) + g\mu_B B S_z)\Big) \tag{1.29}$$

is the density of states.

The results obtained from the TFA are shown in Fig. 1.8, taken from [32]. In (a), when the applied B-field is zero, the density of states $D(\varepsilon)$ is constant, leading to $\mu^{\rm ch}$ that is linear as a function of n_s. The sheet electron density profile is then obtained as a smooth function that, starting from the edge of the 2DES, increase towards the bulk. In (b) instead a magnetic field is considered, affecting the system through the formation of quantised Landau levels. As a consequence, also $D(\varepsilon)$ is discrete and $\mu^{\rm ch}$ becomes a step-like function with n_s, since it follows the filling of the LLs by the electrons. Finally, the electron density profile is no longer a smooth function, but it also shows regions of constant electron density.

Let us now consider the compressibility, defined as $\kappa = \left(\frac{\partial \mu^{\rm ch}}{\partial n_s}\right)^{-1}$. As long as a LL has to be filled , $\mu^{\rm ch}$ is constant; however, when a LL is completely filled, there is a discontinuous increase in $\mu^{\rm ch}$, with further increasing n_s. This implies that

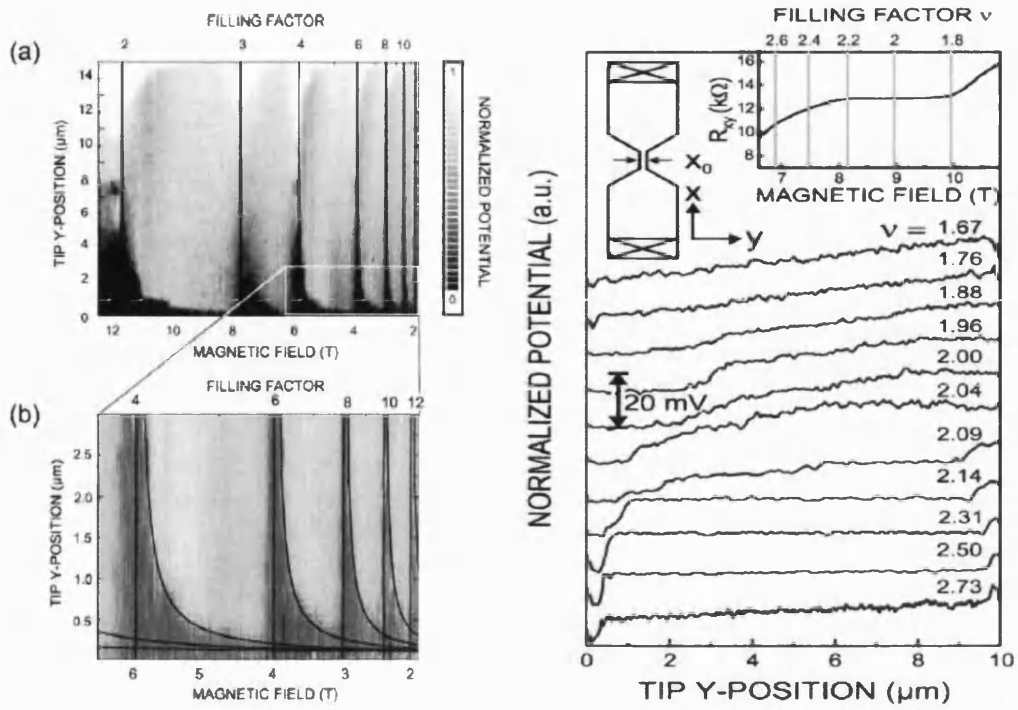

Figure 1.9: Scanning force microscopy (SFM) data taken from Ahlswede *et al* [33, 34, 35]. In a) and b) the normalised Hall potential profile in gray scale for filling factor $2 < \nu < 13$ are shown. Added are the center positions of the incompressible strips as expected from theory. On the right the normalised Hall potential profile for different magnetic fields around filling factor 2 is plotted. Here the overall voltage drop corresponds to 20 mV (RMS). The sample geometry and transport data are shown in the insets. The data indicates that current carrying incompressible channels form at the edge of the sample.

$\frac{\partial \mu^{\mathrm{ch}}}{\partial n_s} \to \infty$ and the system is said to be incompressible ($\kappa \to 0$), whereas before it was behaving as compressible ($\kappa > 0$). As shown in figure 1.8b, applying a magnetic field then plateaus in the n_s vs. $\vec{r}$ plot indicate the formation of incompressible strips, that separate the compressible regions from each other. Experimental studies using a Scanning Force Microscope confirm the existence of these compressible and incompressible regions as shown in figure 1.9.

1.5 Conclusion

In this chapter we introduced the theoretical background necessary for the rest of this thesis. We started with a description of the Hamiltonian of a bulk semiconductor (how to obtain and solve it); afterwards we reduced the dimensionality of the system to 2D and introduced energy quantisation. Next, the electronic transport through such a kind of reduced system was described using both a classical and quantum mechanical model.

Chapter 2

Molecular Beam Epitaxy

Abstract

There has been much investigation of the processes involved in the formation of crystalline epi-layers and there is not enough space in this thesis to discuss it all. A qualitative discussion of some important details is however required and it is given in this chapter. The ultra high quality samples used in this thesis were all grown by molecular beam epitaxy (MBE) [36]. In a MBE system, molecular beams of the constituent elements of a semiconductor and the dopant materials are directed onto a heated crystalline substrate. If the substrate conditions and beam fluxes are suitably chosen, the adatoms will preferentially grow on the surface producing new crystaline epi-layers. By interrupting the beams with mechanical shutters, different layers can be grown on top of each other with atomic precision. After a qualitative discussion of the crystal growth, the various improvements to the MBE system that were made by the author, are discussed.

2.1 Epitaxial growth

A layer of atoms adsorbed on a substrate is subject to two effects. The adatom-adatom interaction favours an interatomic spacing which is the natural spacing in a free standing adatom layer. The adatom-substrate interaction forces the

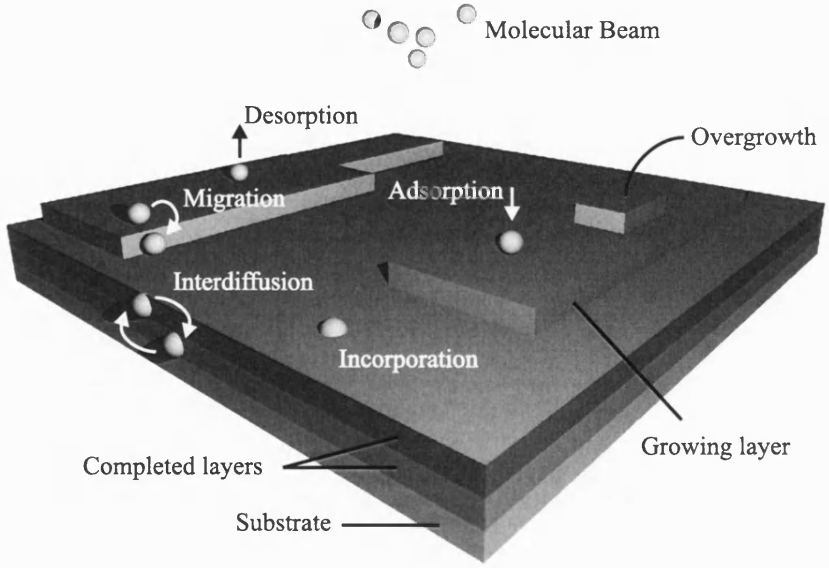

Figure 2.1: Adatoms arrive at the surface of the substate. A number of different processes (described in more detail in the text) are illustrated.

adsorbate towards the lattice constant of the substrate. An incommensurate structure is stabilised when the adatom-adatom interaction is stronger than the adatom-substrate interaction. Conversely, when the adatom-substrate interaction dominates, then a commensurate structure is stable and epitaxy [37] occurs. The first systematic investigation of epitaxy was carried out by L.Royer [38] as long ago as 1929. When adatoms arrive at the surface of the substrate a number of processes can occur as illustrated in figure 2.1. Adatoms can adsorb, migrate over the surface, interact with other atoms and form clusters or terraces, incorporate into the crystal, or desorb. An example of a terraced growth surface can be seen in the atomic force microscope (AFM) micrograph in figure 2.2. Which of the above processes dominates, depends primarily upon substrate condition, substrate temperature, type of incident material and flux.

Heterogrowth is the name give to the growth of one material on top of another type of material. Heteroepitaxy is usually divided into 3 growth modes schematically sketched in figure 2.3. The important growth mode within this project is Frank-Van der Merwe growth. This occurs when successive 2D *virtually* unstrained layers (due to a small lattice mis-match) are deposited. The second growth mode, known as Volmer-Weber growth, occurs when conditions exist such that the added material can reduce its free energy by increasing its surface area to allow a decreased interfacial area, producing droplet-like islands. Finally,

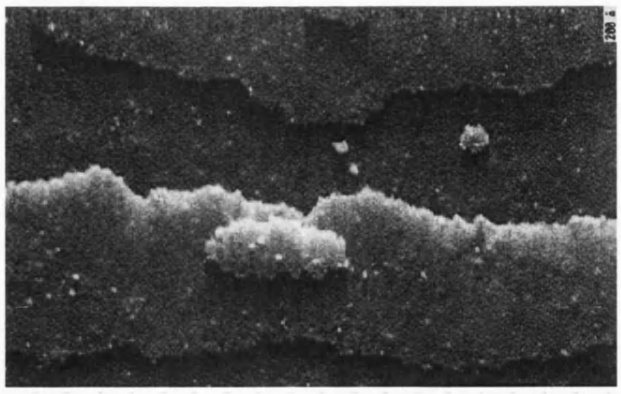

Figure 2.2: Atomic Force Microscope (AFM) picture with atomic resolution of a GaAs 4×4 reconstructed surface. Terrace formation is clearly visible.

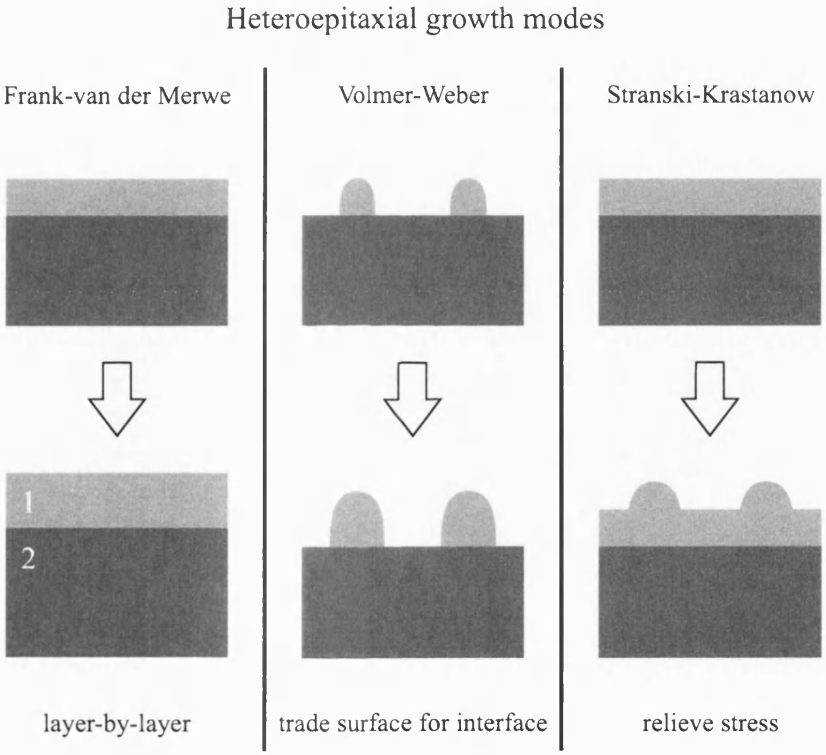

Figure 2.3: The different growth modes possible for MBE samples.

Stranski-Krastinow growth occurs when the substrate lattice spacing greatly mismatches the added material. Growth then starts with 3–6 monolayers, depending on growth parameters, of strained wetting layer growth before the formation of islands occurs. This last technique is used extensively in the production of self-assembled quantum dots.

The arrangement of atoms at a surface differs considerably from that in the bulk. Cleaving a highly covalently bonded body produces dangling bonds which affect the upper layers of the crystal. The surface undergoes both structural reconstruction and relaxation which leads to a reduction of surface energy. The ordering of the surface atoms depends on many factors such as crystal composition, crystallographic direction and temperature. At typical growth temperatures, the surface atoms of an As terminated (100) GaAs layer rearrange themselves into a what is called 2×4 reconstruction. Reflection high electron energy diffraction (RHEED) images with the electron beam pointed along the [011] and [01$\bar{1}$] crystal directions are shown in figure 2.4. The RHEED images along these directions are called the 2 fold and 4 fold patterns, respectively. In addition to primary lines, which correspond to the spacing between atoms on the surface, the 2 fold pattern has secondary lines with a spacing of half the primary line and the 4 fold pattern has lines with a quarter of the primary line spacing. These images imply that the surface atoms under normal growth conditions are arranged into surface structures with 2 times by 4 times the lattice spacing of the bulk material. If the surface becomes Ga terminated due to insufficient As flux, the surface reconstruction will change to a 4×2 pattern, which is similar to the 2×4 pattern except that it is spatially rotated by 90° such that the pattern from the [011] beam direction changes from the 2 fold to the 4 fold pattern. This method is used to calibrate the minimum As-flux required to maintain an As terminated surface. The highest mobilities are obtained with an As terminated surface yet with the lowest possible As flux. With growth conditions intermediate to the Ga-terminated and As-terminated surfaces, other reconstructions such as 3×1 and 4×6 can be observed.

The crystallinity of the surface can be estimated by observing how "spotty" the RHEED image appears. This spotty picture is observed when the surface becomes rough so that the 3D electron diffraction pattern becomes visible. This is generally an indicator that conditions in the chamber during growth are not optimal. RHEED intensity oscillations are also used to calibrate the growth rate; this is because as a new layer starts to form, the surface becomes rough since the monolayer is not full. This principle is best explained graphically by figure 2.5. In the upper section the surface is flat and the deviation in the scattering angle is almost zero and the RHEED signal has an average maximum. During MBE growth adatoms are introduced to the surface and RHEED intensity oscillates as a function of the layer filling. The growth rate calibration using the RHEED signal is very useful since the procedure can be completed in a short time just

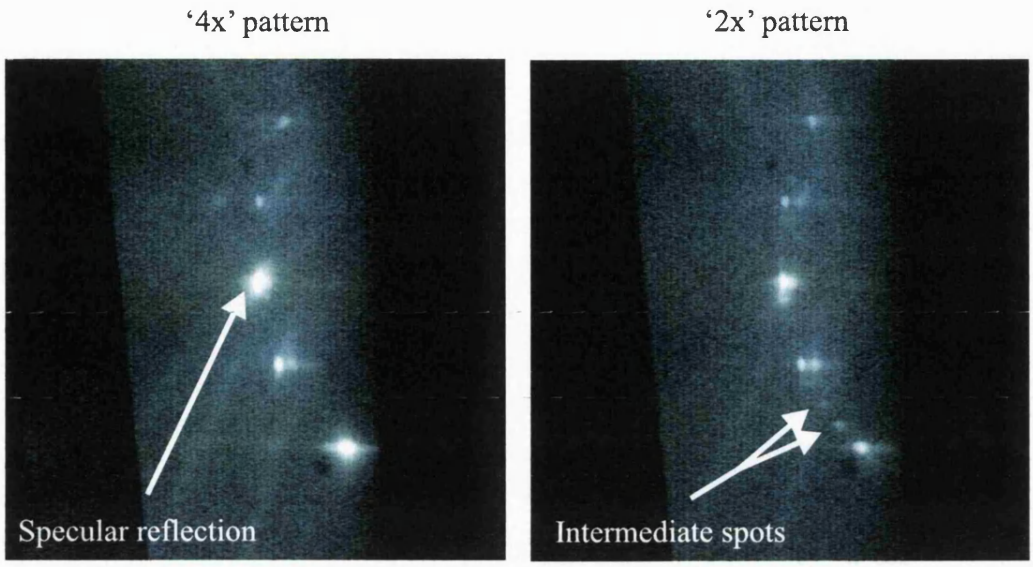

Figure 2.4: RHEED images of 4x (left) and 2x (right) patterns. With growth conditions intermediate to the Ga-terminated and As-terminated surfaces, other reconstructions such as 3×1 and 4×6 can be observed

before the real structure is grown.

Figure 2.6 shows the main components of the MBE growth chamber used in this thesis. The molecular beams are produced using effusion cells. It is critical that the source materials are of extremely high purity. The materials are refined a number of times in order to ensure high purity. It is also critical that the entire process be done in an ultra-high vacuum environment. The growth rates are typically on the order of a few Å/s ($\approx$ 1 monolayer/second) and the beams can be interrupted within fraction of a second by mechanical shutters, allowing atomically abrupt transitions from one material to another. The vacuum is protected from atmospheric gases entering during the loading of samples by using a series of three chambers (loadlock, buffer and growth chambers) each with increasing vacuum quality. Each chamber incorporates a heating stage with temperature control which allows the preheating of samples to remove surface water and impurities introduced during unpacking and loading. Samples are transferred from chamber to chamber, using magnetically coupled transfer rods, to the growth chamber where the sample holder is placed on a continual azimuthal rotation (CAR) manipulator. The CAR rotates on two axes, so the sample can be rotated from loading position to growth position. The second axis of rotation allows the sample to be rotated during growth, this improves the homogeneity of the layers

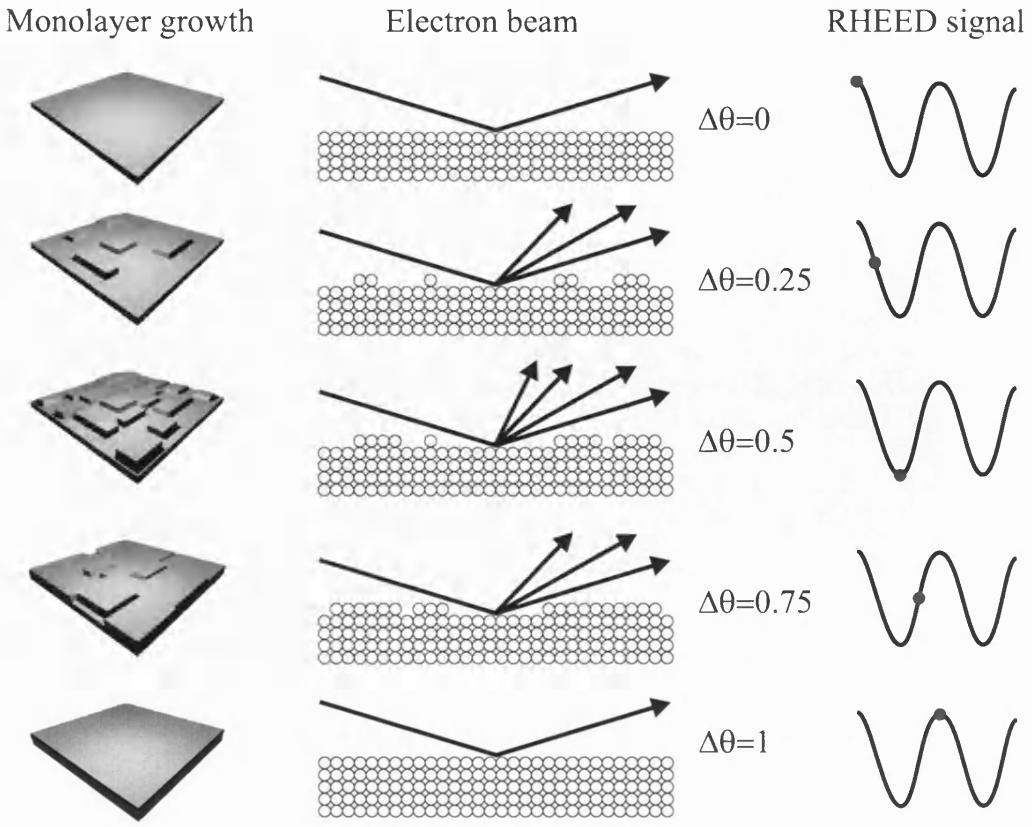

Figure 2.5: Schematic picture of the reflection of the high energy electrons. At the start of the growth process no adatoms are on the surface, the scattering of electrons on the surface is at a minimum and the RHEED signal intensity at a maximum. During MBE growth adatoms are introduced to the surface, the RHEED intensity oscillates as a function of the layer filling and is maximum when the monolayer is completely full.

as it averages the incident fluxes reaching the surface. The CAR is equipped with an ion gauge on the opposite side with respect to the sample. This gauge is used to measure the beam equivalent pressure (BEP) of the sources. A thermocouple is situated at the heating filament and is in thermal contact with the substrate. The temperature measured at the thermocouple is compared with that obtained from the pyrometer. The pyrometer senses infrared radiation. As the bandgap of GaAs is temperature dependent, the measured infrared absorption edge is used to determine the substrate temperature.

A liquid nitrogen cooled cryoshroud is located between the chamber walls and the CAR, with a further cryoshroud in the area surrounding the effusion cells. These act as an effective pump for many of the residual gasses in the cham-

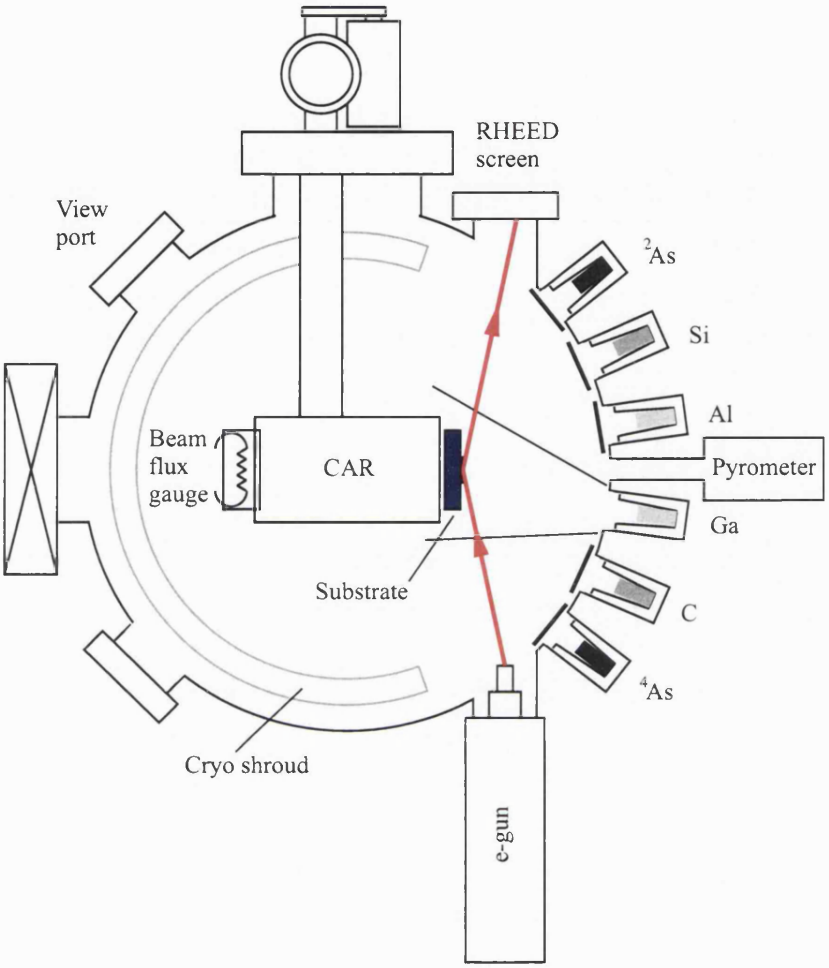

Figure 2.6: Main components of the MBE system used for sample growth by the author. The system consists of a stainless steel vacuum vessel with liquid nitrogen cooled cryo-shrouds. The substrates are mounted on a heatable double rotation stage (CAR). Various molecular beams can be directed onto the substrate from thermal evaporation sources. Substrate temperature is measured with a pyrometer and reflection high energy electron diffraction is used to monitor and calibrate growth. Not shown are the various pumps on the system, the mass spectrometer, the load-lock, the buffer chamber and the connection to the focused ion beam.

ber. Furthermore, the cell shroud prevents thermal crosstalk between cells. The residual gases in the chamber are monitored by a quadrupole mass spectrometer (QMS) situated near the substrate. This is also useful after chamber opening procedures to check for leaks. The background pressure is monitored by an ion gauge situated in the sump of the chamber. The effusion cells are independently heated until the desired material flux is achieved. Changes in the temperature of a cell as small as 0.5 °C can lead to flux changes on the order of one percent, so Tungsten-Rhenium thermocouples with a zero point device are used to measure the cell temperatures. The current through the cell heating elements is controlled using highly stable proportional, integral, and derivative (PID) control loops. The surface of the substrate can be observed at all times using the RHEED system, providing information such as growth rate, surface reconstruction and deoxidation temperature.

The production of good quality structures is strongly dependent on the quality of the vacuum in which these structures are produced. Much work has been carried out on improving the quality of these vacuum chambers. The MBE growth of GaAs and related compounds takes place under ultra high vacuum (UHV) conditions, typically $< 10^{-7}$ millibar, since it is desirable to grow samples containing a low percentage of impurities. If the quality of the vacuum is too low, after a short period of time the surface of the sample is covered with impurity atoms and cannot be properly characterised. This problem can in many cases be reduced when the growth surface is hotter than the other surfaces in the vacuum. However, occasions occur when the substrate must be cooled for low temperature processing or for transfer to other processing chambers and therefore the vacuum quality becomes extremely important.

The behaviour of a vacuum system is characterised by three parameters: pressure P conventionally measured in mbar (or traditionally in Torr), volumetric flow S in units of litres/second and gas throughput Q in torr litres/second. Pumping systems are normally designed to produce constant pumping speed within a given pressure range. Initially during pumpdown this speed is maintained until the outgassing rate of surfaces in the vacuum reaches some minimum value. The vacuum is then at base pressure. The materials used in the construction of all components in the UHV system are chosen to have a low outgassing rate to allow optimum base pressure. The base pressure of our system has been improved by approximately a factor of 10 by baking the system at 200 °C for several weeks. Care was taken to heat and cool the system slowly to prevent leaks (stainless

steel expands by approximately 0.5% upon a 100 ° C increase in temperature). The baking process is effective in removing weakly bonded surface water and hydrocarbon molecules producing a better base pressure. Moreover, it has been shown that by baking stainless steel for $>$ 100 hours at 200 °C its outgassing rate is considerably reduced [39].

The pumping systems installed on MBE chambers usually consist of an oil-free pre-vacuum system in conjunction with a system for pumping in the UHV pressure range. There are many different types of pumps available all with their own advantages and drawbacks. The MBE system used to produce the samples in this thesis is equipped with a rotary pre-pump which drops the pressure to approximately 10^{-3} torr at which point the UHV pumping system takes over. The chamber is also equipped with a Meca 2000 ion getter pump. Sputter ion pumps operate by ionising gas within a magnetically confined cold cathode discharge. Burial is the basic means of pumping heavy noble gases. Ions neutralised via glancing collisions with a sputter cathode impact the pump wall and are coated with sputtered titanium.

The chamber of our MBE system has meanwhile been equipped with a second CTI cryo-torr8 cryopump. These pumps create a vacuum by simply condensing and freezing most of the gases that are in the vacuum chamber. The pumps consist of two stages. The upper stage has an integral radiation shield which protects the pump from thermal loads produced by the vacuum chamber. It operates typically between 60-90 K and captures mostly water molecules. The second stage operates between 10-20K. This captures the O_2, N_2, CO, CO_2 and Ar molecules. Activated charcoal is bonded to the second-stage condensing array. The higher vapour pressure gases such as H, H_2, He and Ne are collected by the carbon. The amount of material the carbon can hold is limited and since these higher vapour pressure gasses are not frozen, from time to time the cryopumps have to be regenerated, i.e. pumped empty while they are at room temperature.

The chamber has a further Ti sublimation pump. This pump sublimates a small amount of metal from a 85% Ti 15% Mo filament at regular intervals into the chamber and is used to pump chemically reactive getterable gases. Ti pumps have high pumping speeds at pressures below 10^{-6} Torr and are inexpensive.

At the start of this project the quality of the vacuum was insufficient to produce good samples. A second cryopump was added to the system to increase pumping

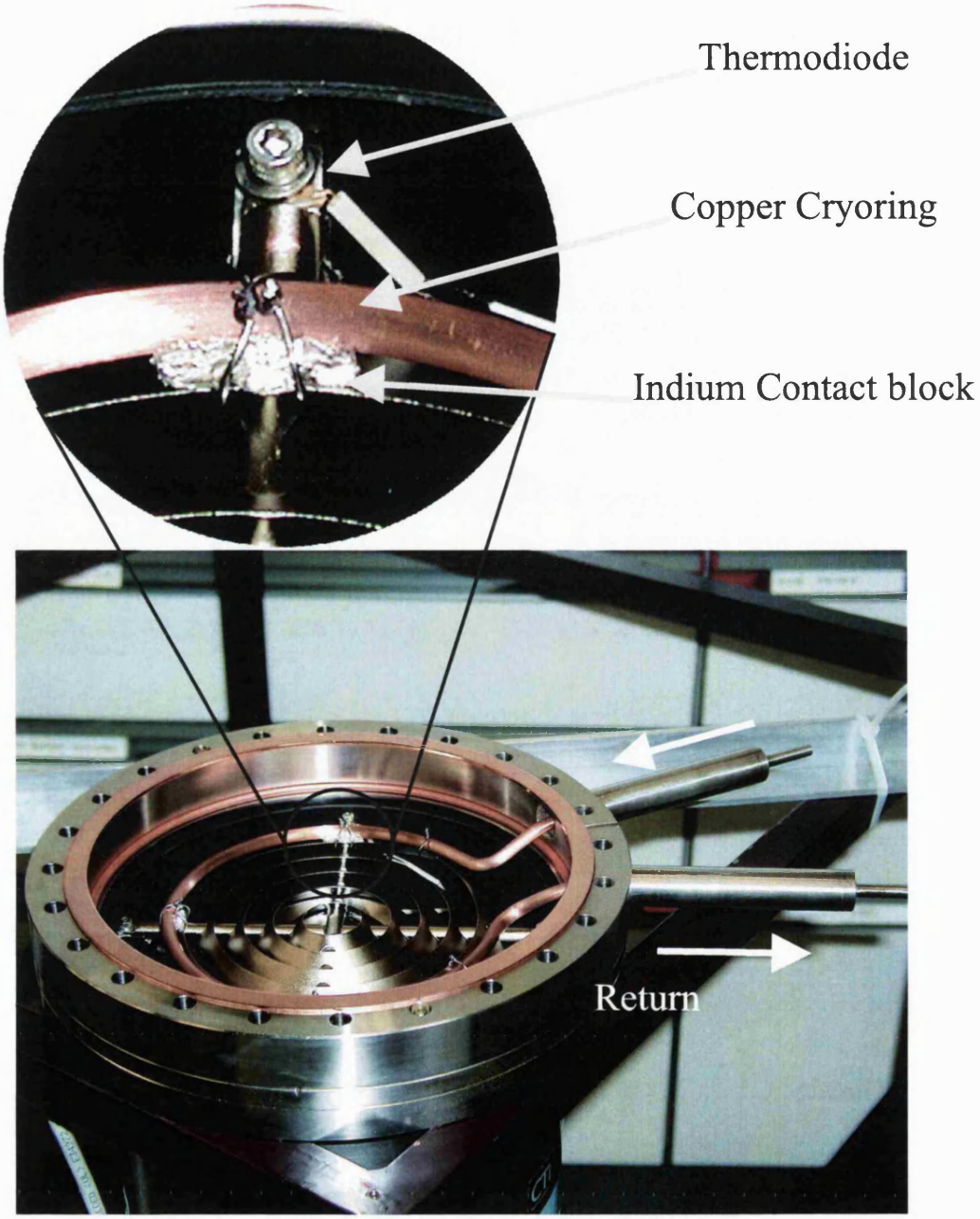

Figure 2.7: The cryopumps were modified with a liquid nitrogen cryoring. This keeps the cryopump at pumping temperature during elevated temperature bakeout procedures. The copper ring is in thermal contact through the use of indium contact blocks to the upper stage of the cryopump. Liquid nitrogen is forced through the 6 mm diameter tube which provides sufficient cooling power to keep the pump cold even when the growth chamber is at 200°

power. One problem with the use of cryopumps is that the standard radiation shielding is insufficient to protect the pump from radiation during baking of the chamber at elevated temperatures. When the MBE chamber is heated above 80 °C the lower section of the pump heats up and this prevents the removal of residual gasses from the chamber. The pump actually releases gas at these temperatures. Both pumps on the system were therefore modified with a cryoring that is in thermal contact with the upper stage of the pump via Indium blocks. This is shown in figure 2.7. Liquid N_2 was forced to flow through the 6 mm diameter cryoring providing sufficient cooling to allow the pump to be operated with the chamber temperature in excess of 200 °C. Furthermore, the ion-getter pump on the system has been renovated because it no longer reached pressures below 5×10^{-10} bar. The active elements were removed, etched, cleaned, dried, baked and remounted. After long delays, the above efforts resulted in a factor 2.5 better base pressure. More importantly, the residual C contamination decreased by more than a factor of 10. This resulted in factors of 8 and 3 increase in mobility for 2D AlAs and 2D GaAs electrons respectively.

Further improvements were made to the UHV transfer system that connects the MBE to the focused ion beam implantation machine. A new buffer chamber was installed and equipped with a cryopump. Both the buffer chamber and the transfer system were baked at 200 °C for 2 weeks. The new buffer chamber has a vacuum better than 10^{-10} Torr and the UHV-tunnelsystem a vacuum better than 10^{-9} Torr, i.e. both vacuums are more than an order of magnitude better than before. The improvements to the transfer system and middle chamber were very important for the production of coupled electron-hole samples, since the wafer is transfered through this system twice during the growth interruption.

Chapter 3

Focused Ion Beam Technology

Abstract

A Focused Ion Beam (FIB) is an instrument that allows the implantation of designated areas of a sample with the desired ion species and implantation energy. In this project a FIB is used to produce separate contacts to the lower layer of the 2DES/2DHS samples by either implanting directly the contact area with dopant material or by compensating an already doped bottom layer to provide isolation in specific areas. In this chapter we discuss the principle of operation of the FIB. Furthermore, because a commercial stable FIB source for Au/Si/Be ions does not exist, the fabrication of a custom built source is described.

3.1 The focused ion beam instrument

The prototype Canion 31Z FIB instrument from *Orsay Physics* used in this work (see figure 3.1a) can provide a stable and intense beam of Ga ions for implantation. In the initial stages of this work, this source was used to make certain areas in a doped layer insulating. At a later stage, it was found out that instead of insulating a doped layer locally, the best way to proceed was to write the contact areas directly. For this another source was needed, since other ions are needed for the fabrication of contacts to 2DEG/2DHG samples. These ions are produced

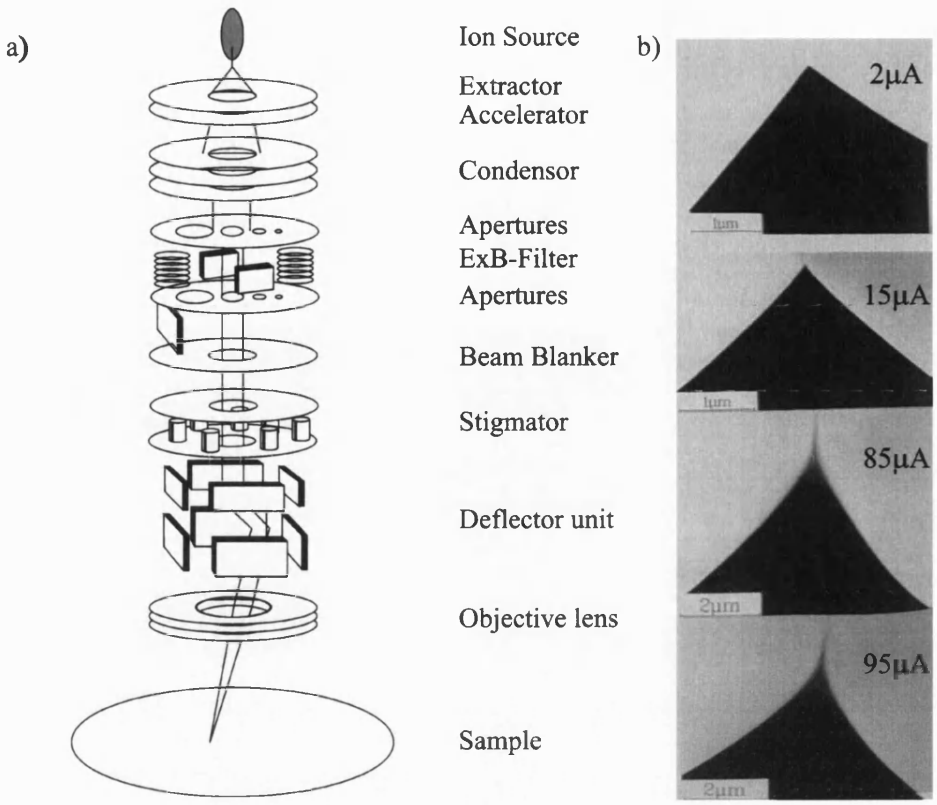

Figure 3.1: a) Schematic diagram of the FIB instrument showing the main components of the system. b) High voltage transmission electron micrographs showing the development of the Taylor cone with increasing beam current from top to bottom. Note the large deflection of the beam for large currents.

from a custom made Au/Si/Be liquid metal ion source (LMIS), since a commercial source with this kind of material is not available.

The source material in our custom built source is a eutectic alloy of Au, Si and Be which allows both n-type and p-type implantation. The Au allows visible alignment marks to be written (see figure 3.2). The alloy is resistively heated until it becomes liquid and an extraction voltage of $\approx$ 5 kV is applied to the extraction plate. A cone shaped plasma (Taylor cone) is produced at the tip of the LMIS (see figure 3.1b). The ions in the plasma are accelerated to the operation energy (10-30 kV for mono charged ions). The ion beam is then focused by two electrostatic asymmetric lenses in the condenser, which also compensates for Taylor cone deflection. The probe current can be selected using a series of mechanical acceptance apertures or can be completely closed off using the beam blanker. The E $\times$ B filter (so called Wien filter) allows the required ion

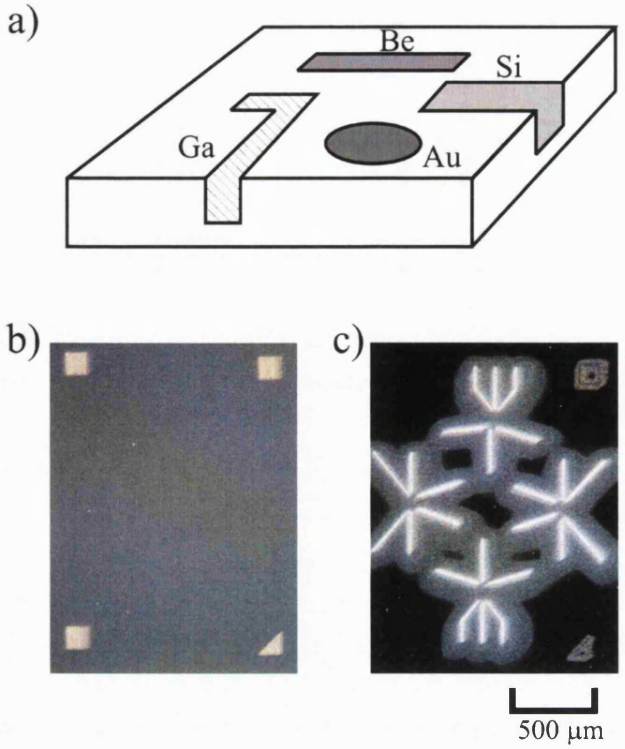

Figure 3.2: a) It is possible to implant ions of different type in close proximity to each other. This allows different areas in the sample to be selectively doped. b) Photomicrograph of a sample after FIB implantation of Si for contacts (not visible) and Au for alignment marks after MBE overgrowth and rapid thermal annealing. c) A test sample implanted completely with Au at high dosage used to check implantation area.

species to be selected. The electrostatic octupole allows astigmatic correction of the beam. The deflection unit allows the rastering of the beam for secondary electron imaging and is controlled by an adapted scanning electron microscope imaging system. The deflection unit also provides the steering of the beam across the sample during implantation using the proxy writer system (software by Raith GmbH). The FIB incorporates a coaxial optical microscope and X-Y movement stage allowing easy sample loading, alignment and setup. An integral Faraday cup allows the measurement of the probe current close to the sample. During typical process protocols, a sample is implanted with between 6-8 structures with different beam intensities.

3.2 The liquid metal ion focused ion beam source

The Au/Si/Be ion source as supplied by *Orsay Physics* was not usable since the beam current was very unstable (even on the timescale of minutes). Since there are no other commercial sources available, the FIB sources used in this project were custom made by the author. The process of producing a source with a high and constant intensity is not a trivial matter; the geometrical parameters such as tip curvature and tip-extractor spacing are extremely important and many refinements are necessary to produce sources with high quality. The LMIS used in this thesis was fabricated by R. Muelhe and the author at the Swiss Federal Institute of Technology (ETH) in Zurich. The source material must be of a high purity, because doping concentration is calibrated from the beam current and any unknown contamination in the source material would make accurate implantation impossible. Furthermore, contamination of the vacuum system could occur by introducing compounds which are not compatible with high mobility MBE growth. The purity is tested using a time of flight mass spectrometer during the source fabrication. The base and electrical connections are made on a commercial electron microscope cathode. The cathode is removed from the base plug until only the electrical pin connectors remain. Then a new Tungsten heating element hairpin is formed from 200 μm drawn wire with the correct shape (see figure 3.3a) to encourage good flow of material before the emitter (300 μm wire) is spot welded to it. Figure 3.3b shows the hairpin and attached emitter; figure 3.3c shows the finished source. The hairpin-emitter assembly is then welded to the cathode electrical pins and then all welds are checked using a microscope. The emitter is cleaned, polished and roughly cut to size using an electrochemical etch process (ECEP) with NaOH. The ECEP is a very versatile tool for processing thin wires since the etch parameters such as etch rate and etch profile can be easily changed by varying the bias voltage. The emitter length is carefully measured and then precisely cut to the correct length in accordance with the required beam characteristics. The tip of the emitter must also have the correct curvature and surface morphology. Therefore in the final steps, the tip is sharpened, rounded and then roughened. The tip roughening produces grooves and pits on the surface (see SEM picture in figure 3.4) which have be shown to improve beam stability. After construction, the source emitter must be out-gassed in a vacuum better than 1×10^{-7} mbar. The tip can now be wetted (i.e. loaded with material). To this end the source is now placed in a UHV chamber equipped with electrical connections and an extractor plate and the correct amount of source material

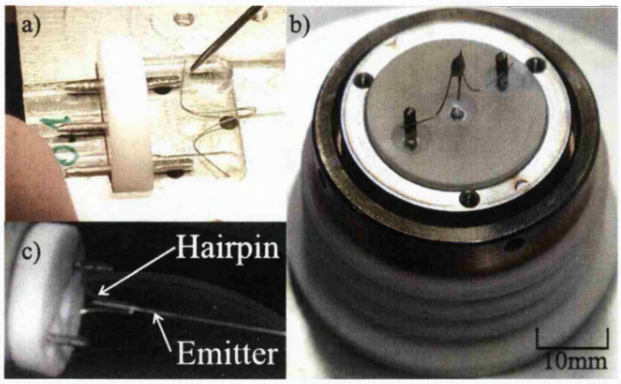

Figure 3.3: a) The forming of the Tungsten heating hairpin. The hairpin is mounted in a Al jig so welding is possible. The Al plate is the lower section of the jig, it has three holes through which the welding takes place. b) The hairpin with the uncut emitter tip welded in place. c) The finished source after wetting and testing.

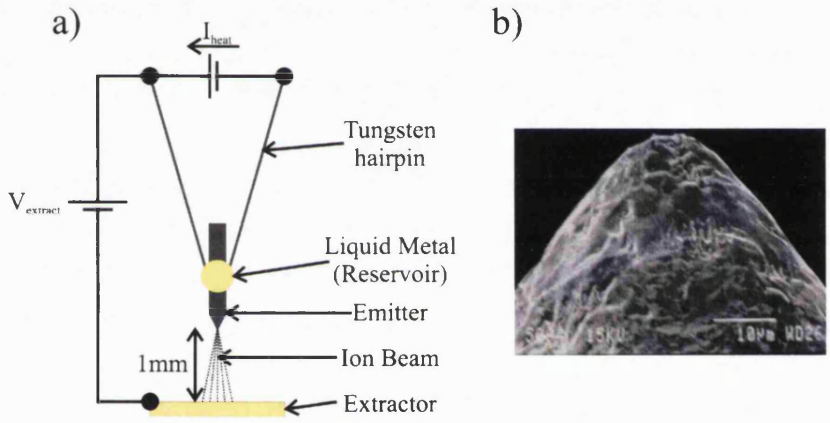

Figure 3.4: a) The main features of the custom built FIB source. b) Scanning Electron Micrograph of the roughened, wetted LMIS emitter tip showing pitting and grooving.

is placed on the hairpin-emitter weld point. The UHV system is pumped down and the hairpin is heated by passing a current through it and the source material is melted and then cooled. The source is now rotated into the vertical position and heated again. The liquid droplet must be correctly positioned on the emitter by applying an electric field and if necessary by using some mechanical tapping. Correct positioning of the source material is necessary to ensure beam stability and long source lifetime. The extraction voltage and heater operating power are determined. The source material purity is then checked using a time of flight mass spectrometer. This instrument is fitted with a window through which the source can be observed during operation. It additionally allows the use of a pyrometer

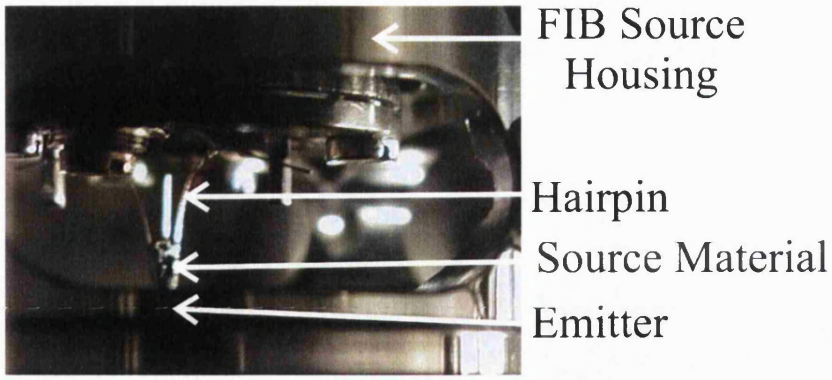

Figure 3.5: View of the finished FIB source through the viewport of the mass spectrometer. A pyrometer can be used to accurately measure the temperature of the hairpin and source material. This allows easy calibration of the power requirements of the source.

for temperature measurements (see figure 3.5). After the successful test of source material quality, the source is then transfered to the operational housing and the tip-extractor spacing and deflection are adjusted to optimum values. The final testing and tuning could then be safely conducted in the Orsay Physics column in Stuttgart.

3.3 Conclusion

The FIB is a very versatile tool for the selective doping of semiconductor microstructures. In conjunction with MBE growth, different layers in the growth sequence can be selectively implanted and overgrown. In this chapter the principle of operation of the prototype Canion 31Z FIB instrument from *Orsay Physics* was introduced. For this project a suitable commercial FIB source was not available, therefore the construction and testing of the Au/Si/Be LMIS was described.

Part II

Electronic Magneto-transport in Aluminium Arsenide Two-dimensional Systems

Chapter 4

AlAs Quantum Wells

Abstract

AlAs is generally employed as a barrier material in structures utilising $Al_xGa_{1-x}As$ alloys. This chapter is however concerned with structures which are instead designed to confine electrons to the AlAs layer. We start by introducing the conduction band structure bulk AlAs and then explain how the 2D confinement of electrons in AlAs is achieved using $Al_xGa_{1-x}As$ as a barrier material. We discuss the MBE growth sequence, growth parameters and quality of the samples. The Fermi surface of electrons in AlAs is ellipsoidal and their effective mass is thus anisotropic. This makes a large impact on the transport properties. We discover in fact that the occupation of electronic states in AlAs quantum wells is dependent on the width of the well and that it is due to the biaxial strain caused by the tiny lattice mismatch of AlAs to $Al_xGa_{1-x}As$. The final section of the chapter discusses the energy level structure with a magnetic field applied.

4.1 AlAs band structure

AlAs, like GaAs, has a Zincblende crystal structure, but in contrast to GaAs, the conduction band minimum lies at finite **k**-vector which characterises it as an indirect semiconductor. The band structure can be calculated as discussed in

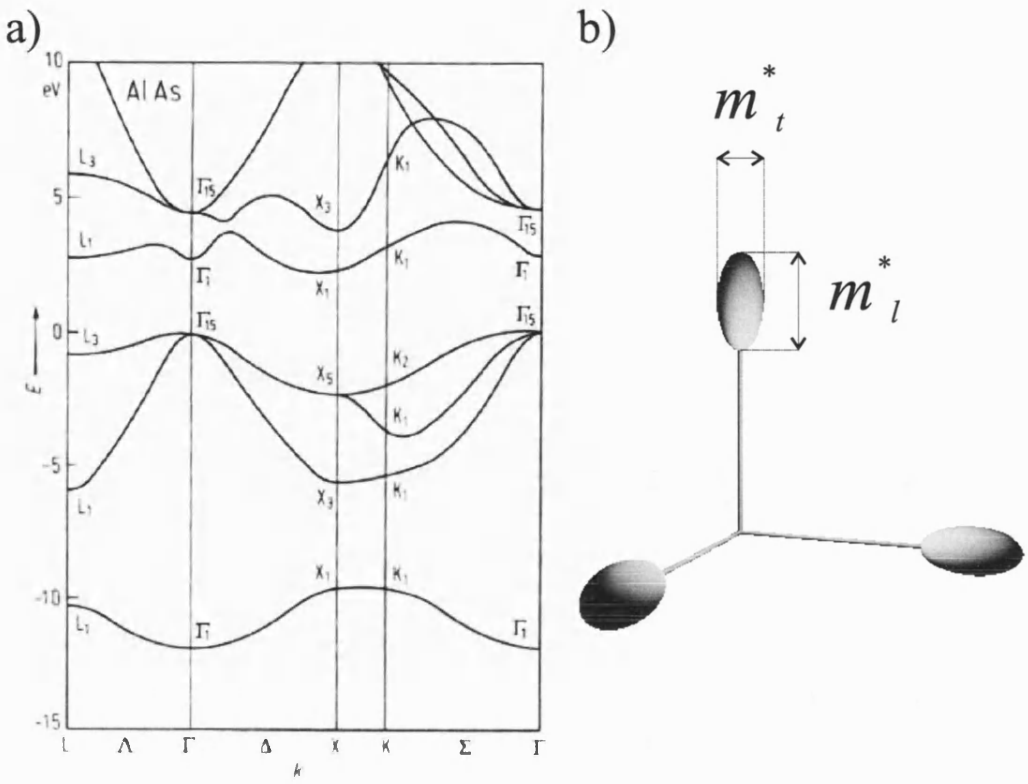

Figure 4.1: a) The dispersion relation for AlAs calculated using minimal basis orthogonalised linear combinations of atomic orbitals method. b) The Fermi surfaces of bulk AlAs showing 3 ellipsoids of revolution. The anisotropic effective mass arises from the non-spherical Fermi surface. The transverse mass m_t^* and the longitudinal mass m_l^* are indicated.

Chapter 1 and is shown in figure 4.1a [40]. Due to crystal symmetry, bulk AlAs has a sixfold degenerate conduction band minimum near the X-point of Brillouin zone. Since the Fermi surface ellipsoids lie half within the first Brillouin zone, they can equivalently be thought of as effectively 3 full ellipsoidal Fermi surfaces (see figure 4.1b). The effective mass is proportional to the inverse of the second derivative of the energy dispersion in **k**-space, hence the effective mass (m^*) in AlAs is anisotropic. In experiments, the effective mass can be determined by cyclotron resonance. In AlAs the transverse effective mass is $m_t^* = 0.19\mathrm{m}_e$ while the longitudinal mass $m_l^* = 1.1\mathrm{m}_e$. The cyclotron effective mass m_c^* for [001] and [010] valleys with magnetic field parallel to [100] becomes $m_c^* = \sqrt{m_l^* m_t^*} = 0.46m_e$ [41]. While the m_c^* of the [100] valley is $m_c^* = m_t^* = 0.19m_e$ These values are much larger than the *isotropic* effective mass of GaAs $m^* = 0.067\mathrm{m}_e$. The effective Landé g-factor of AlAs $g^* = 1.989$ [42] is also larger and has a different sign than that of GaAs $g^* = -0.44$.

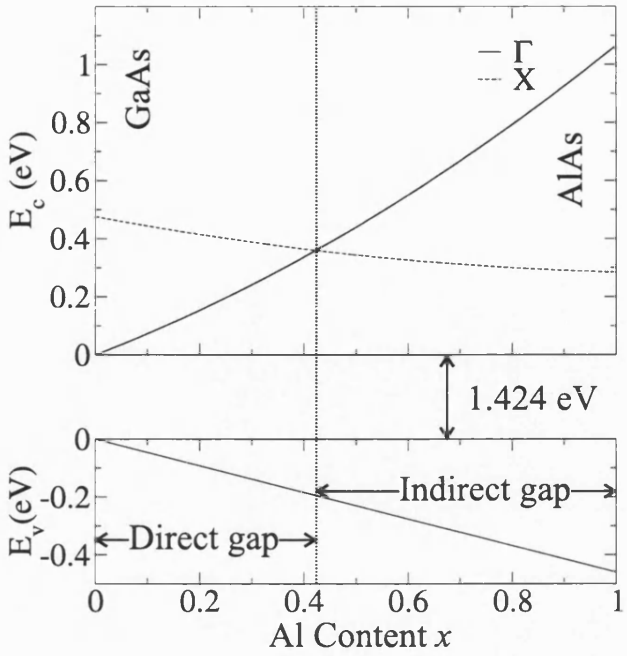

Figure 4.2: The variation of the Γ and X conduction band minima and valence band edge in $Al_xGa_{1-x}As$ alloys as a function of Aluminium content x. For values of x greater than 0.43 the alloy becomes an indirect semiconductor. This figure is a useful tool when designing structures since the bandgap can be simply chosen by specifying the x content.

Figure 4.2 shows the conduction band minima (upper section) and the valence band maxima (lower section) as a function of Aluminium content x. The X-valley conduction band minima in AlAs can be lower in energy than the Γ-point conduction band minimum of $Al_xGa_{1-x}As$ [43]. To confine electrons in an AlAs layer, we use $Al_{0.45}Ga_{0.55}As$ as the barrier material. This Al concentration was selected because at this point the band discontinuity between the X conduction band minimum in AlAs and X conduction band minimum in $Al_xGa_{1-x}As$ is at a maximum (70 meV) and therefore the confinement potential of the quantum well structure is largest.

The growth sequence and growth parameters were optimised to produce high electron mobility. Contrary to what is usually considered to be the best method to grow high mobility samples, a relatively low growth temperature of the deoxidation temperature $T_{ox} + 25°$is used. This ensures a reduced segregation of Si with the growth front. To compensate any ill effects from the reduced surface mobility of adatoms due to low growth temperature, the growth rate of the AlAs layers was also reduced to only 0.4 monolayers/second. This allows more time

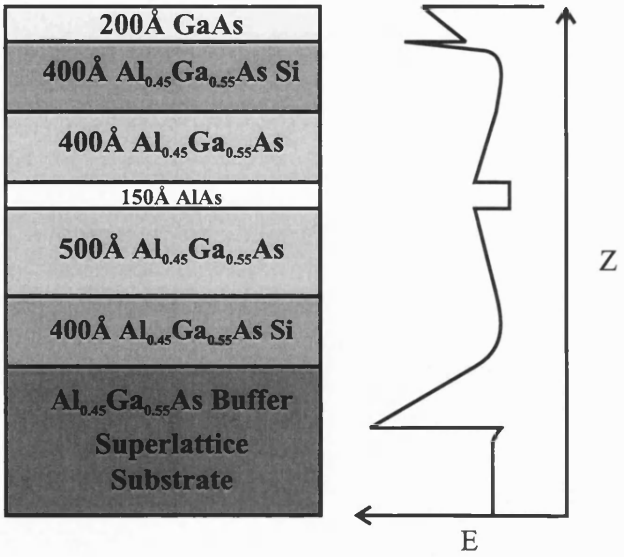

Figure 4.3: The MBE grown layer sequence which is grown on a (100) orientated GaAs substrate. The sequence consists of a 15 nm AlAs layer grown between upper and lower $Al_{0.45}Ga_{0.55}As$ spacer layers. Si modulation doping layers are grown on either side of the spacers and provide the carriers to the quantum well. To the right is shown conduction band structure schematic of the AlAs quantum well structure.

for the adatoms to find equilibrium positions at lattice sites and thus improves crystal quality. The modified growth parameters allow us to dope the quantum well on both sides and to grow larger spacer layers between the doping regions and the quantum well whilst still maintaining a high electron density.

Figure 4.3 shows the growth sequence and the schematic band structure of the samples used in this thesis. The structure is grown on a (100) orientated GaAs substrate with superlattice and buffer layer and consists of a 15 nm AlAs QW layer grown between upper and lower $Al_{0.45}Ga_{0.55}As$ spacer layers with 400 Å and 500 Å thickness respectively. Si doping layers (Si $=4 \times 10^{18}$ cm^{-3}) with thickness of 400 Å are grown on either side of the spacers. Figure 4.4 shows examples of the structures used the measurements. The upper section shows Hall bars orientated along various crystal directions. Below is shown the sample containing Hall bars with various widths. To demonstrate the quality of the samples we have measured the electron mobility versus carrier density for two of our samples and compared the results with the best data found in the literature [44]. Figure 4.5 shows that our samples are of very high quality. Furthermore, the high quality of our samples can be seen from figure 4.7 which shows ρ_{xx} and R_{xy} measured on a Hall bar sample at T=40 mK. The data clearly show the integer and fractional

Sample before cleaving
and bonding

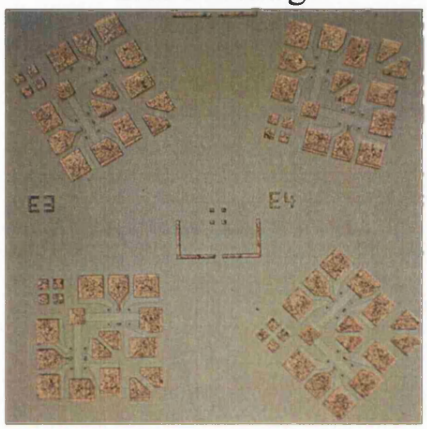

Samples mounted
and bonded in the die

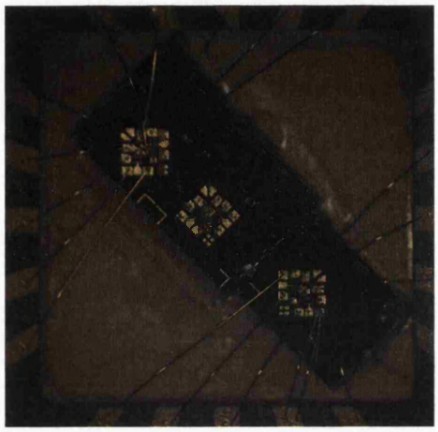

Hall bar samples
with widths of 1-10 μm

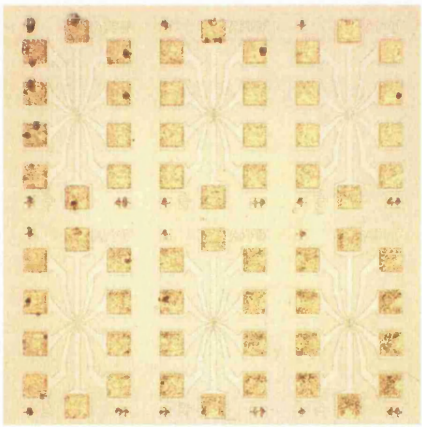

Figure 4.4: Top left shows the L-shape Hall bar structures orientated along various directions. Right shows two selected samples mounted and bonded in the die. The lower section shows a sample with Hall bars of various widths.

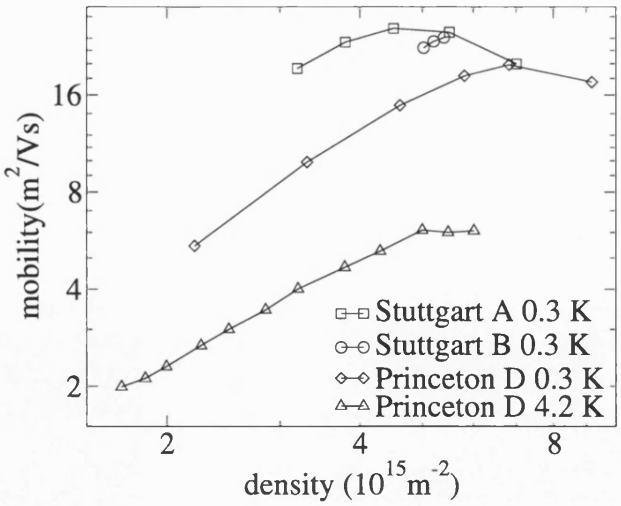

Figure 4.5: Electron mobility versus carrier density of different high quality AlAs quantum well samples (A,B) used in this thesis compared to values obtained from literature [44] (D). This method is often used to display sample quality.

quantum Hall effects with zeros in ρ_{xx} and quantised plateaux in the R_{xy}.

4.2 The effective mass of X-valley electrons in AlAs wide quantum well structures

We now consider the effective masses of electrons confined in the QW. Since the confinement in 2D breaks the symmetry of the electron energy levels, the threefold degeneracy is also broken. This results in the formation of two levels, one level with a degeneracy of two and the other with a degeneracy of one. This arises because the subband energy is determined by the effective mass of electrons in the direction of confinement (here the growth direction). For electrons in the out of plane valley this mass is $m_l^* = 1.1m_e$ and for the electrons in the two in-plane valleys, it is $m_t^* = 0.19m_e$. Since m_l^* is substantially larger than m_t^*, it is expected that the lowest energy level, or ground state, should be that of electrons in the out of plane valley. Surprisingly, however, the temperature dependence of the Shubnikov-de Haas oscillations in 7.5 nm wide AlAs QW superlattice structures [41] indicates that the effective mass of electrons moving in the xy-plane is 0.55 m_e. This corresponds well to the cyclotron mass of electrons from the in-plane valleys and thus indicates that in 7.5 nm wide QWs, the in-plane

valleys are lowest in energy. Furthermore, the observed factor of two difference in the electron concentration measured by Hall measurements or by SdH oscillations in this experiment (where valley splitting was not resolved) can be explained, since when the two in-plane valleys are occupied the ground state has a degeneracy of two. Other experiments on AlAs QWs with varying QW width and barriers of $Al_{0.45}Ga_{0.55}As$ have shown that the X_z valley is not populated for quantum wells wider than 4.5 nm, while for narrower QWs the in-plane X_y an X_x valleys are not populated [45]. This reveals that there is a crossover in the energies of X_z and X_{xy} valleys.

One candidate for the cause of this energy crossover is a strain induced energy shift due to the lattice mismatch of GaAs to AlAs. Even though this mismatch is small (on the order of 0.12%), it has been shown that this can produce an energy shift which is enough to explain the crossover in the lowest energy states [41]. The strain induced energy shift of the X-valley energy levels ΔE_{strain} can be estimated using the deformation potential

$$\Delta E_{\text{strain}} = -E_2(S_{11} - S_{12})\sigma \tag{4.1}$$

where $E_2 \approx 5.5$ eV is the shear deformation potential, $S_{11} \approx 1.3 \times 10^{-12}$ cm^2/dyn and $S_{12} \approx -0.39 \times 10^{-12}$ cm^2/dyn are the elastic constants and $\sigma \approx 2.2 \times 10^9$ dyn/cm^2 is the stress. This gives an estimated energy shift of $\Delta E_{\text{strain}} \approx 19$ meV. It must also be noted that, due to biaxial compression, the levels for the X_y and the X_x-valley need not necessarily have the same energy. The structures discussed in this thesis, in fact show significant valley energy splitting, as we shall see in the following sections.

To calculate the ground state subband energy of electrons in a QW one must solve the Schroedinger equation for a particle in a box. First, we consider the simple case of the electron confined to a box with infinite potential barriers. In this case the wavefunction of the electron must be zero in the barriers, which gives the boundary conditions $\psi(x = 0) = 0$ and $\psi(x = a) = 0$, a being the well width. These boundary conditions can be satisfied by choosing $\psi = sin(kx)$, which gives $sin(ka) = 0 = sin(n\pi)$ thus $k = n\pi/a$. The subband energy E_n is then given by

$$E_n = \frac{\hbar^2\pi^2 n^2}{2m_z a^2}, \tag{4.2}$$

where m_z is the effective mass in the direction of confinement. The subband energy E_n is thus proportional to the inverse of the mass in the direction of

confinement.

To calculate the ground state energy in a real semiconductor QW accurately, we should take into account that the barrier height V_0 is now finite and equals the conduction band offset. This means that the electron wavefunction can now penetrate the barrier. Since the barrier penetration *effectively* increases the well width, the finite barrier QW energies are lower than those in a infinite barrier well. The ground state solution for a finite potential well is in lowest even parity state and can be expressed as:

$$\alpha = ktan\left(\frac{ka}{2}\right) = \sqrt{\frac{2m_z(V_0 - \frac{\hbar^2 k^2}{2m_z})}{\hbar^2}} \tag{4.3}$$

where V_0 is the conduction band offset. Both sides of the equation are dependent on E and the equation is transcendental and thus cannot be solved analytically. One way to estimate the ground state energy is to use the energy obtained from the infinite potential well as in Equation 4.2 to produce a trial attenuation factor α. This α can then be refined by iteration to obtain the effective well width and a numerical solution of the energy. Figure 4.6 shows the calculated subband energies using this method (taking $m_t^* = 0.19\mathrm{m}_e$ and $m_l^* = 1.1\mathrm{m}_e$ with a conduction band offset of 70 meV [46]) as a function of well width, including the estimated energy shift of 19 meV as given by Equation 4.1 [41]. This gives an estimate of the crossover of X_z and X_{xy} valley energies at 47.5 Å. Since our samples are 15 nm wide QWs we can safely assume that the in-plane X_y an X_x valleys are lowest in energy.

Two valley occupancy in our samples is confirmed in two ways. First the low magnetic field transport displays a positive magnetoresistance (PMR), shown in the inset of figure 4.7. PMR can have a number of both quantum mechanical and classical origins. However, it is most likely that this PMR arises from classical two band transport where each of the two occupied valleys in the QW behaves as a separate channel with different mobility and/or density. Second, the Shubnikov de Haas oscillations shown in the inset of Figure 4.7 exhibit a clear beating pattern indicating the existence of more than one occupied subband. This data also indicates that the subband energies (or effective masses and g-factors) of the two valleys are not the same.

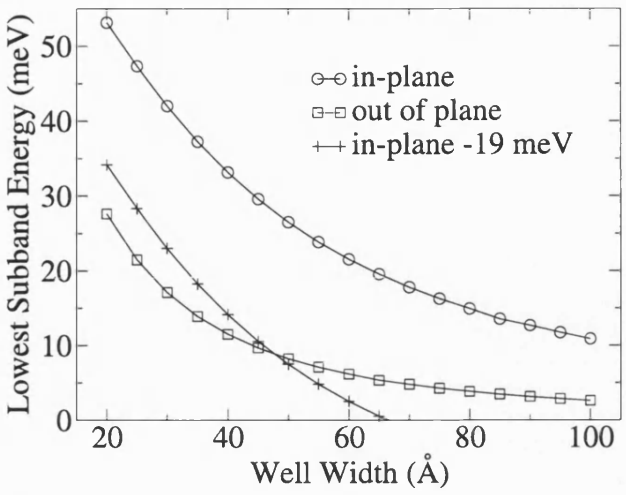

Figure 4.6: Subband energies versus QW width calculated using $m_t^* = 0.19\mathrm{m}_e$ and $m_l^* = 1.1\mathrm{m}_e$. Data for m_t^* is also shown with a strain induced energy shift of 19 meV. The crossover of ground state levels takes place at 47.5 Å indicating that for wide QW structures the in-plane X_y an X_x valleys are lowest in energy.

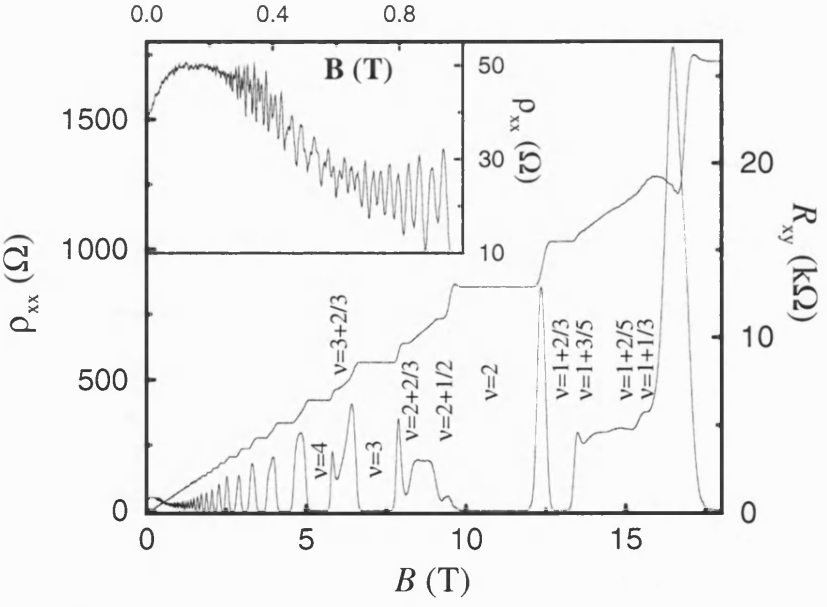

Figure 4.7: ρ_{xx} and R_{xy} measured on a Hall bar sample at T=40 mK. The data clearly show the integer and fractional quantum Hall effects with zeros in ρ_{xx} and quantised plateaus in R_{xy}. In the low magnetic field plot (see inset) a strong PMR and beating in the SdH oscillations are observed which indicate two valley occupation.

4.3 Landau level scheme in two valley AlAs quantum well structures

Figure 4.8 shows a diagrammatic view of energy levels in a magnetic field which are important in our system. From the left we see that there are two Landau levels separated by an energy $\hbar\omega_c$ and given the indices N and N+1. These two levels are split due to the magnetic field by $g^*\mu_B B_{\text{total}}$ giving two spin levels per Landau level. On the right each level is split again due to the valley splitting. To identify specific levels we will use the nomenclature $< N, X, S >$, where N is the Landau level index, X is the valley index and S is the spin index having the value of $\uparrow$ or $\downarrow$.

We identify here that Zeeman energy is B_{total} dependent, while the cyclotron and valley splittings are $B_\perp$ dependent [47]. By including an in-plane component of the magnetic field we can change the Zeeman term and keep $B_\perp$ the same. This allows us to tune the position of energy levels in the system so that it is possible to bring energy levels with different spin into coincidence. Figure 4.9 shows examples of different crossings which are possible. In our experiments we can easily introduce the in-plane component of the B-field by tilting the sample away from the perpendicular using a sample rotator which has a 90° span. Because of the large g-factor and large cyclotron mass in AlAs QWs, many Landau level crossings are accessible within the experimental range.

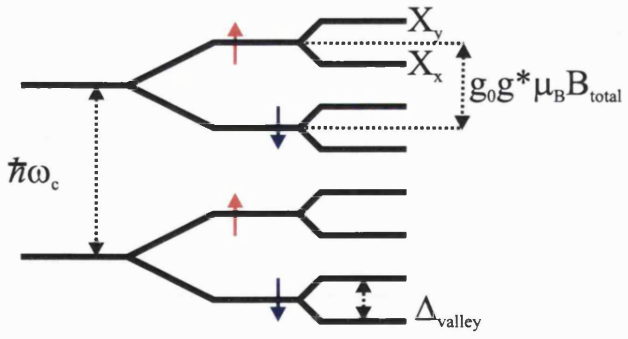

Figure 4.8: Schematic diagram of the relevant energy levels in wide AlAs quantum wells in a magnetic field. On the left the levels are split by the cyclotron energy. In the centre each Landau level is split by the Zeeman energy and on the right, each of the spin split Landau levels is split again by the valley splitting (Δ_{valley}).

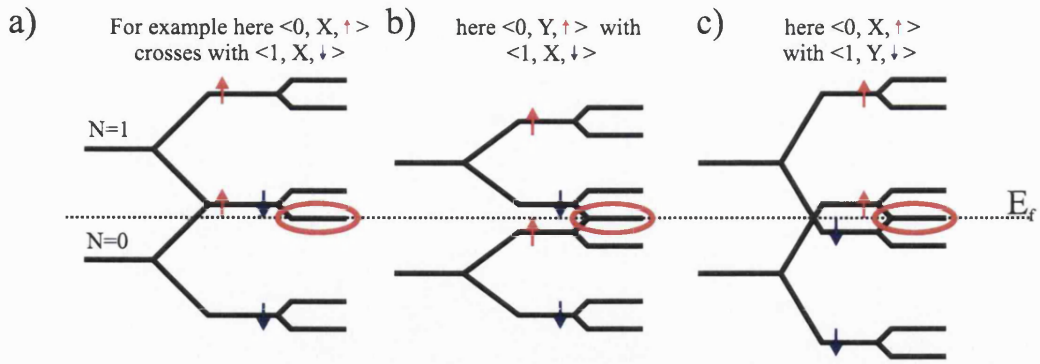

Figure 4.9: Schematic diagram showing some examples of different crossing types which are possible by introducing an in-plane B-field component. The crossing points are indicated by the ellipse at the Fermi energy.

4.4 Tilted field measurements in low magnetic field

In figure 4.10 we see a colour plot of the magnetoresistance ρ_{xx} (blue and red represent small and large values of ρ_{xx} respectively) versus $1/\sin\theta$ and filling factor ν. This plot was made by taking magnetoresistance traces at 120 different angles θ. Coincidences of energy levels are identified from increases in the minimum of ρ_{xx} at integer filling factor that occur at particular tilt angles. The data can be analysed by using a general model for the energies of a two-valley system, the level energy of one valley being given by

$$E_1 = \left(N + \frac{1}{2}\right)\frac{\hbar e B_\perp}{m^*} \pm \frac{1}{2} \mid g^* \mid \mu_B \frac{B_\perp}{\sin\theta} + \frac{\Delta_{\text{valley}}}{2} \tag{4.4}$$

and that of the second valley by:

$$E_2 = \left(N' + \frac{1}{2}\right)\frac{\hbar e B_\perp}{m^*} \pm \frac{1}{2} \mid g^* \mid \mu_B \frac{B_\perp}{\sin\theta} - \frac{\Delta_{\text{valley}}}{2} \tag{4.5}$$

where E_1 and E_2 are the energies of the two coinciding levels, N and N' their respective Landau level indices and g^* the effective g-factor. By fitting the coincidences of energy levels from the same valley (that occur at odd filling factor), we can determine the Zeeman energy (in the units of the cyclotron energy) or $\mid g^* \mid m^*$. Similarly from the coincidence of energy levels of different valleys (that occur at even filling factor) we can determine $m^*\Delta_{\text{valley}}$.

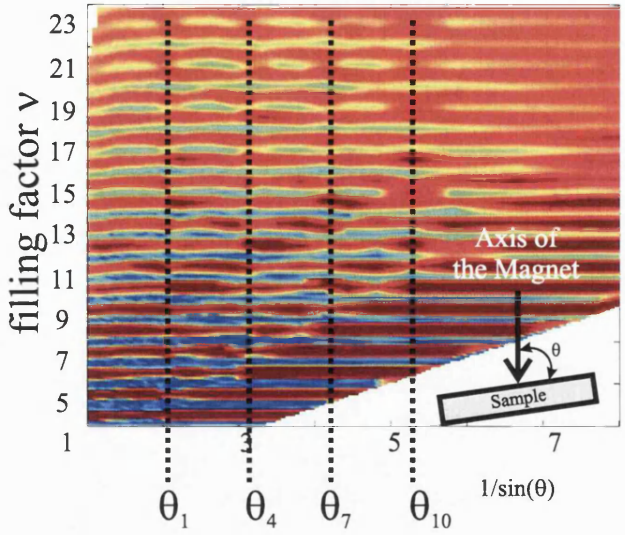

Figure 4.10: Colour plot of the magneto resistance ρ_{xx} versus $1/\sin\theta$ and filling factor ν. The colour scale shows high resistance in red and areas of low resistance are shown in blue. The inset shows θ relative to the sample. Landau level crossings are identified by an enhancement of ρ_{xx} at integer filling factor. This is clearly visible especially for the higher filling factors, i.e. $\nu = 23$ and $\nu = 21$

First, we will consider the crossing of levels from the same valley. These occur at odd filling factor at angles θ_1, θ_4, θ_7 and θ_{10} as indicated in the figure 4.10. The Zeeman energy in the units of the cyclotron energy for these crossings is given by:

$$\mid g^* \mid m^* = \frac{\hbar e \sin\theta}{\mu_B}(N' - N) \tag{4.6}$$

Figure 4.11 shows a plot of data obtained from Figure 4.10, for coincidences of same valley crossings. $\mid g* \mid m^*$ is shown versus filling factor ν for θ_1, θ_4, θ_7 and θ_{10}. The band value of $|g^*_{\text{band}}|m^*$=0.916 [42] and the mean of the enhanced values of $m^*|g^*|$=1.945 are indicated. At high filling factor, $|g^*|m^* \approx$ constant. For lower filling factors, it increases a little. Furthermore, $|g^*|m^*$ is significantly enhanced over the full range of filling factors (by more than a factor of 2) compared to its band value.

Using the same data and interpolating $|g^*|m^*$ to the even filling factors we can determine the value of the valley splitting Δ_{valley}. We limit the study to the region where $|g^*|m^*$ is constant using angles of θ_2, θ_3, θ_5 and θ_6 at which the energy levels from different valleys cross. In our data these crossings are not as clearly visible as in ref [47], but nevertheless with the use of Equations 4.4 and

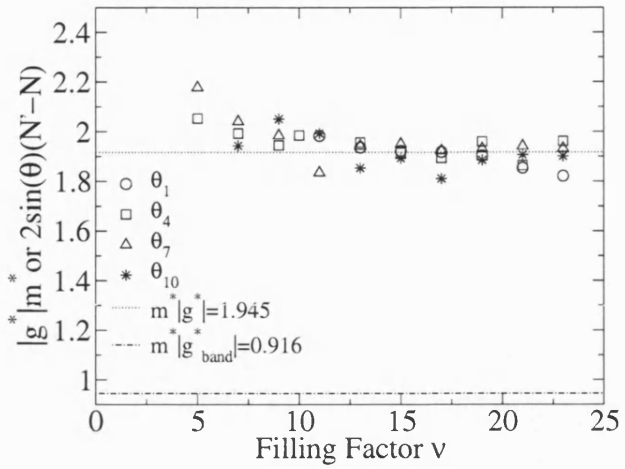

Figure 4.11: Plot of $|\ g^*\ |\ m^*$ versus filling factor ν for θ_1, θ_4, θ_7 and θ_{10}. Also shown is the band value of $|g^*_{\rm band}|m^*$=0.916 [42]. Over the entire range of filling factors, $|\ g^*\ |\ m^*$ is significantly enhanced compared to the band value. In the high filling factor range, g* | m^* | remains approximately constant and equals 1.945.

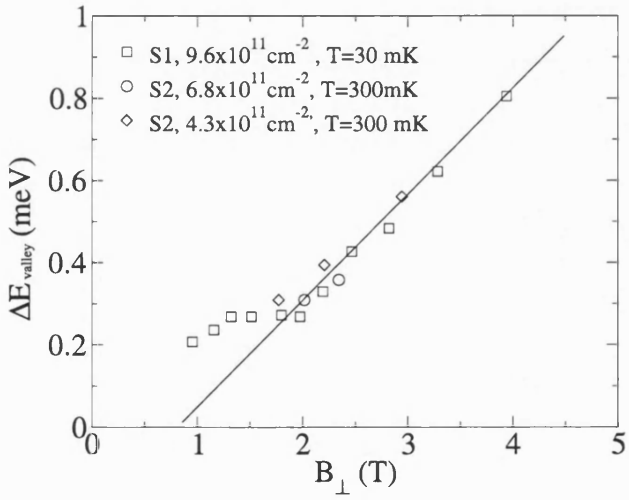

Figure 4.12: Valley splitting $\Delta_{\rm valley}$ for different samples S1 and S2 with different densities versus $B_\perp$. For $B_\perp$ greater than 1.5 T the data displays a linear behaviour and the least squares fit shown by the solid line gives $\Delta_{\rm valley} = -0.22 + 0.25B_\perp$ assuming m^*=0.46 [47].

4.5 we obtain

$$(N - N')\hbar e = \frac{m^*\Delta_{\rm valley}}{B_\perp} \tag{4.7}$$

We assume $m^* = 0.46$ and that $m^*|g^*|$ is constant as determined above and has a value of 1.945. Now that $\Delta_{\rm valley}$ and g* have been obtained it is possible to identify which levels are crossing. Figure 4.13 shows the positions of the resistance

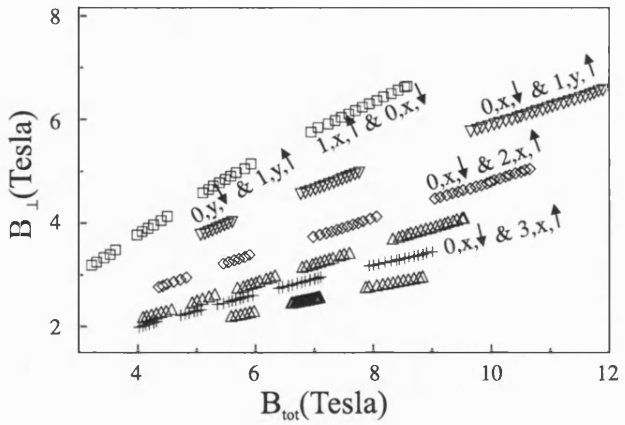

Figure 4.13: Position of various Landau level crossings in the ($B_\perp$,B_{tot}-plane

maxima in $B_\perp$,B_{tot}-plane as the sample is tilted. At low filling factor few Landau levels are below the Fermi energy, it is therefore possible to deterimine exactly which levels are crossing.

In figure 4.12 Δ_{valley} does not vary with coincidence angle (for values above 1.5 T) and is therefore independent of $B_{||}$. This dependence on only $B_\perp$ suggests that electron-electron interaction is responsible for its behaviour, however the enhancement would then be expected to inversely scale with the magnetic length, i.e. $\propto \sqrt{B_\perp}$, which is clearly not the case.

4.5 Conclusion

In this chapter we introduced the band structure and valley characteristics of AlAs electrons and how in this material confinement in two dimensions can be achieved. We described how biaxial strain due to the tiny lattice mismatch makes the occupation of electron levels dependent on QW width. The growth details and sample layer sequence were outlined. The characterisation of the samples was conducted by measuring mobility versus carrier density and indicated that the samples used in this thesis are of superb quality. The Landau level structure and Landau level crossing tilted field magnetic field measurements were used to obtain $|g^*|m^*$ and the valley splitting.

Chapter 5

The Ising Quantum Hall Ferromagnet

Abstract

Our experiments conducted on high mobility AlAs samples show peculiar features when two Landau levels are degenerate in energy. The Landau levels are brought into degeneracy by adding an in-plane magnetic field which increases the Zeeman energy. Besides the disappearance of the minimum in the longitudinal resistance at integer filling factor, the appearance of a large spike in the longitudinal magneto-resistance close to integer filling factor is observed. At the lowest temperatures these spikes show hysteretic effects, i.e. their position and amplitude are different for sweeping the magnetic field up and for sweeping it down. The spikes in the resistance are believed to be due to enhanced backscattering of electrons across the sample along so-called domain walls, that separate regions with the first Landau level at the Fermi energy from regions with the second Landau level at the Fermi energy.

Moreover, the transport of electrons at the resistance spike is very anisotropic, i.e. the amplitude of the spike can change by a factor of 4 when the direction of the in-plane field with respect to the current is changed. One theory correlates the non-flatness of the quantum well in the direction of the in-plane magnetic field to this resistance anisotropy. We investigate three Landau level crossings

with transport along various crystal axis, one at ν=5, one at ν=6 and the last one at ν=7. Whereas the first crossing seems to confirm the theory, our subsequent measurements (at ν =6, 7) indicate that more ingredients are needed to explain the puzzling experimental results.

Introduction

Recent experiments conducted on high mobility samples in high magnetic fields, where two Landau levels are degenerate in energy, have shown very surprising new phenomena. Besides the disappearance of the minimum in ρ_{xx} at integer filling factor, in high mobility samples a huge spike in the longitudinal resistance near integer filling factor is also observed. Moreover, at the lowest temperatures, these spikes display hysteretic effects, i.e. their position and amplitude depend on whether the magnetic field is swept up or down. Due to the close analogy with these effects that we and others observe to the behaviour of conventional itinerant electron ferromagnetism [48], the name Quantum Hall Ferromagnetism (QHFM) was coined to label these systems. Anomalous behaviour of these phenomena, such as the onset of hysteresis at temperature much below T_c and the surprising appearance of strong anisotropic behaviour, warrant a thorough investigation.

QHFM occurs when two different Landau levels, distinguished by the cyclotron energy, spin energy, or valley energy, are brought into energetic alignment and the Landau level filling factor is close to integer values [49]. The study of this phenomenon in an AlAs QW structure greatly reduces the complexity since the interactions of electrons with the host material are almost completely contained in the effective mass m^* and effective g-factor g^*. Moreover, because of the favourable ratio of the Zeeman energy to the cyclotron energy, many Landau level crossings can be studied at moderate tilt angles of the sample in the magnetic field. There have been several theoretical works which have discussed QHFM systems and characterised them as either easy-plane (XY), isotropic (Heisenberg) or easy-axis (Ising) ferromagnets [49]. Our AlAs 2DES at the Landau level crossings, as we shall later see, is an easy-axis (Ising) ferromagnet.

5.1 Mean field theory of an Ising system

5.1.1 Discrete symmetry

In group theory, the simplest discrete group is Z_2 with two elements, the identity and an element whose square is the identity. Hamiltonians which are invariant under Z_2 are said to have Ising symmetry. This Ising symmetry is broken in any phase transition in which there are only two equivalent ordered states which are characterised by order parameters that differ only in sign. The order parameter m_z (the z-component of the magnetisation) can be either negative or positive, but the magnitude is fixed by the thermodynamic equilibrium obtained by the equations of state.
To calculate the electron energy E we need to evaluate

$$E =< \mathscr{H} >= Z_m^{-1} \mathrm{Tr}_m e^{-\beta \mathscr{H}} \mathscr{H} , \tag{5.1}$$

where Tr_m is a trace over all configurations with fixed m and $Z_m = \mathrm{Tr}_m e^{-\beta \mathscr{H}}$ [50]. The evaluation of this average would give the exact solution to the Ising model as obtained by Onsager [48].

5.1.2 The Bragg-Williams model

The Bragg-Williams theory approximates $< \mathscr{H} >$ by replacing the spin variable σ_l in the Ising Hamiltonian

$$\mathscr{H}_{Ising} = -J \sum_{<l,l'>} \sigma_l \sigma_{l'} \tag{5.2}$$

with the position independent average m. The Bragg-Williams model can be applied to a system comprising of two energies with respective fillings of f_1 and f_2. The magnetisation is defined as $m_z = f_1 - f_2$ so that, when f_1 is fully occupied, $m_z = 1$ and, when f_2 is fully occupied, $m_z = -1$. The electron energy can be written as $E(m_z) = bm_z - \frac{1}{2}Jm_z^2$, where b is an effective magnetic field that includes both single-particle Landau level splittings and interactions and J is the effective interaction strength or effective Ising interaction [49]. The free energy of the 2DES is given by $F(b, m_z) = -TS(m_z) + E(b, m_z)$, where $S(m_z)$ is

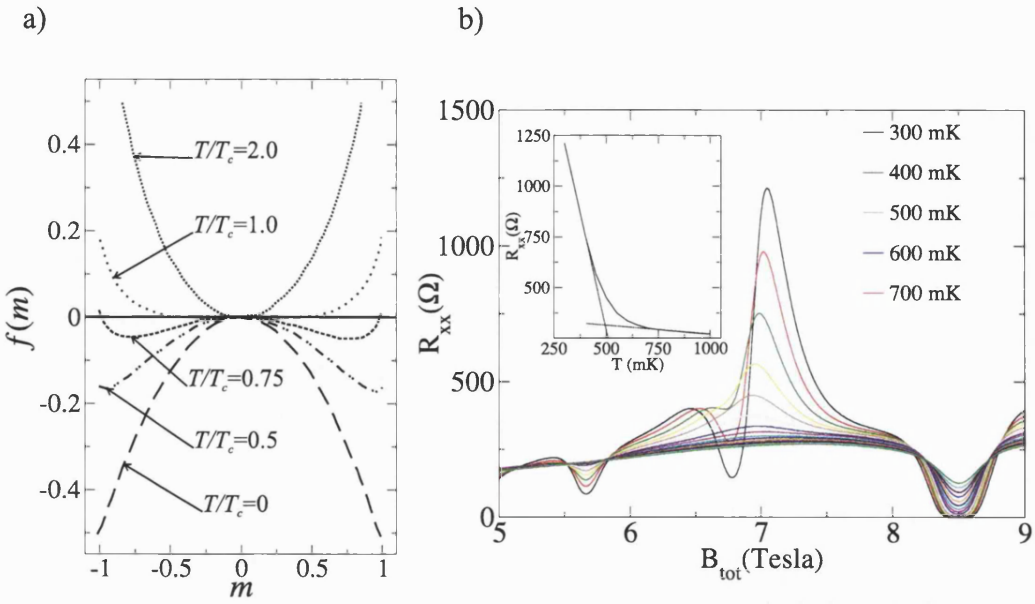

Figure 5.1: a)Bragg-Williams free energy as a function of order parameter for different values of T/T_c. For $T > T_c$ there is a single broad minimum at $m = 0$ [50]. As the temperature is decreased below T_c, two minima appear with the same free energy at $\pm m$. At $T = 0$, the minima in the free energy occur at $m = \pm 1$. The plot indicates that below T_c the symmetry of the system is broken, since now there are two levels with the same free energy which minimise $f(m)$. b) The main figure shows a series of magnetoresistance traces at different temperature for an AlAs 2DES that has been tilted to the coincidence angle of two pseudospin levels. A large peak occurs at low temperature. The inset plots the peak maximum versus temperature. The gradient of the curve changes at around 500 mK, which gives an estimate for T_c.

the mixing entropy of the two phases and T is the temperature. If we minimise F with respect to m_z, for every b and T we obtain the equilibrium magnetisation. For $T < T_c$ (known as the Curie temperature) two different magnetisations m_z minimise F and the system divides into magnetic domains. Figure 5.1 shows a plot of the Bragg-Williams free energy as a function of the order parameter m, for various temperatures. The data for $T > T_c$ display a single broad minimum at $m = 0$. For values of T below T_c a two fold minimum occurs at finite $\pm m$. In the limit of $T = 0$, the minima occur at $m = \pm 1$.

This Bragg-Williams model can be applied to the QHFM by using a pseudospin label to distinguish the crossing Landau levels. In our sample, energetic alignment of Landau levels with different spin indices at $T = 0$ will always give a ground state of magnetisation $m_z = 1$ or $m_z = -1$ everywhere, which identifies that we

have an Ising type QHFM [49]. In the above section, we have shown that domain formation is expected for temperatures less than T_c. To test the model, we have measured the magneto-resistance for different temperatures at the coincidence of two pseudospin levels; this is shown in Figure 5.1b). As the temperature is increased, the peak amplitude decreases. The inset of the figure shows the peak maximum as a function of temperature. The gradient of the curve changes at $\sim$ 500 mK, which corresponds favourably with the value of T_c for a similar set of sample parameters calculated by Jungwirth *et al* [49].

5.2 Hysteresis of the resistance spikes

Further studies of the resistance spikes conducted at lower temperatures show hysteresis effects. Figure 5.2a) and b) plot measurements conducted at 25 mK. On the left we see the longitudinal resistivity at a coincidence of two Landau levels versus the perpendicular component of magnetic field around $\nu = 5$ for increasing magnetic field (shown in black) and for decreasing magnetic field (shown in red). A clear hysteresis in both position and in amplitude of the spike is seen. The occurrence of hysteresis is expected only for an easy-axis Ising QHFM and these measurements thus confirm that transitions in our samples are of the Ising type as described by [49]. Figure 5.2c) plots temperature dependent data around ν=3 taken from [51]. Here the AlAs 2DES is single sided doped and has a lower density. Once more a strong hysteresis is observed albeit only in amplitude of the spike. Why there is no hysteresis in the position of the spike remains unclear.

A further observation which complicates the understanding of the data is that the hysteresis is observed only at low temperature. Measurements at elevated temperatures of 250 mK show no or very small hysteresis. At these temperatures the crossing of Landau levels is still clearly visible and therefore the system must be at a temperature below T_c. However, the absence of hysteresis indicates that further changes in the system occur at temperatures much below T_c. The onset of hysteresis at temperatures lower than the Curie temperature shows that metastability must be 'frozen' into the system as the temperature is decreased. Other authors report that the strength of the hysteresis depends also on sample cooldown [51]. For all data shown in the following sections the measurement temperature is 250–270 mK, therefore this hysteresis behaviour is not important.

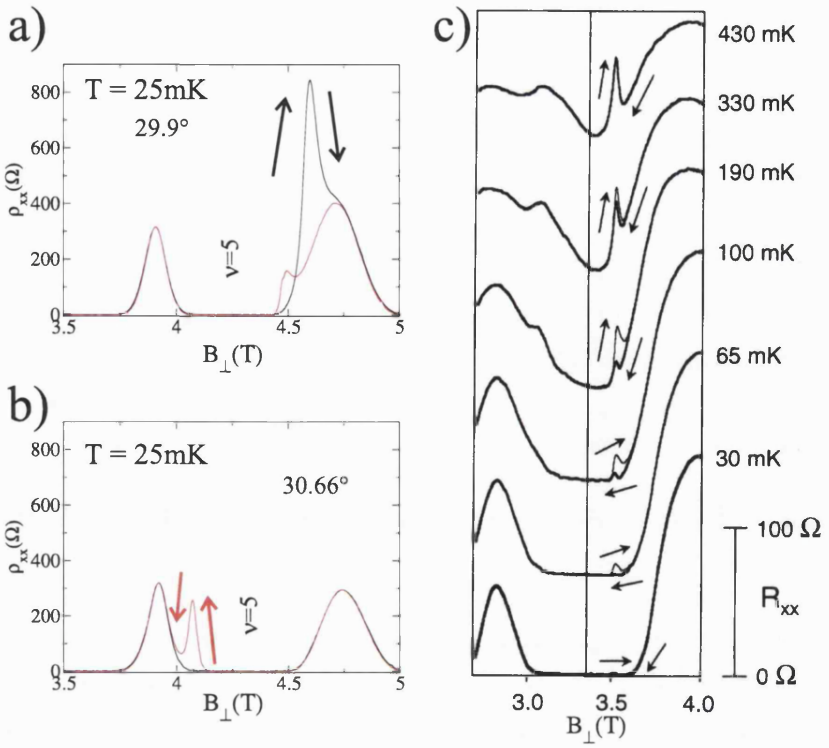

Figure 5.2: a) and b) show Landau level crossings around ν=5 for two different tilt angles. A strong hysteresis is clearly visible in both amplitude and position as the sweep direction is reversed. c) Temperature dependent data taken from [51] that show how the hysteresis disappears with increasing temperature.

Moreover, we have verified experimentally that the results obtained on different cooldowns reproduce. This allows the comparison of data obtained on different cooldowns.

5.3 The Origin of the resistance spikes at Landau level crossings

A highly simplified but helpful picture to understand how resistance spikes occur is outlined in figure 5.3. In a) initially the system has only one Landau level at the Fermi energy. As the sample is tilted further, while the perpendicular component of the magnetic field is kept constant, the Landau level crossing occurs, i.e. two Landau levels become degenerate. At the crossing (shown in b), the

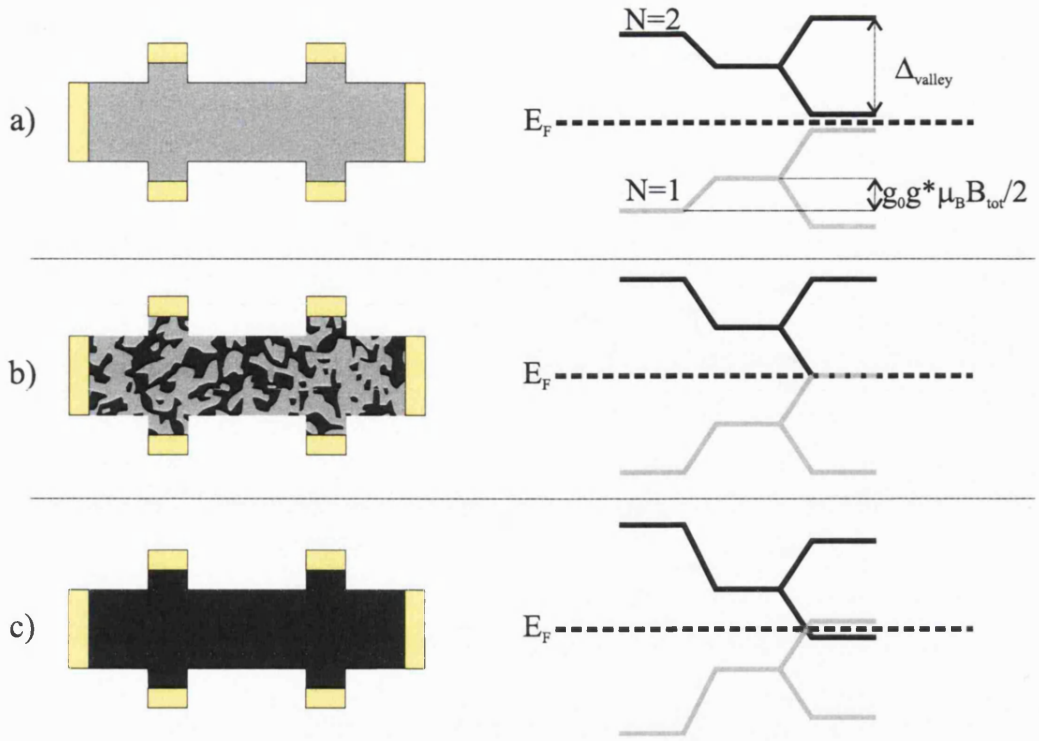

Figure 5.3: a) Initially, the system has only one Landau level at the Fermi energy. As the sample is tilted while keeping the perpendicular component of the magnetic field constant, the Landau crossing occurs, since the levels become degenerate. b) At the crossing the 2DES breaks up into domains, i.e. regions with one Landau level at the Fermi energy and regions with the other Landau level at the Fermi energy. As a consequence, the backscattering probability is greatly enhanced. In c) the sample is tilted further until again only one Landau level occupies the 2DES. This simple picture shows that at the crossing, the dissipation in the system can be large due to the complicated current paths originating from the existence of domain boundaries.

2DES breaks up in to domains; some areas in the sample have Landau Level 1 at the Fermi energy and others have Landau level 2. The backscattering probability is greatly enhanced due to the complicated domain morphology sketched in b). In c) the sample is tilted further until Landau level 2 occupies the entire 2DES. This simple picture shows that at the crossing, the dissipation in the system can be large due to the complicated current paths originating from the existence of domain boundaries. This most likely causes the elevated resistances. The exact origin of the resistance spike is believed to be due to scattering processes in the vicinity of the domain wall. However, the details of the process are still under debate. There are a number of theoretical works which address the problem of

how dissipation occurs.
One theory suggests that the resistance enhancement is due to charge transport of 1D quasiparticles in long domain wall loops [49]. In this paper a Self-consistent random phase approximation/Hartree-Fock theory is applied to microscopically determine properties of the ground state and domain wall excitations. The theory states that domain wall loops support one-dimensional electron systems which may carry charge. The theory is able to account quantitatively for the experimental Ising critical temperature and to explain qualitative characteristics of the resistive hysteresis loops. Others speculate that the dissipation occurs as electron go through the domain walls [52]. In this paper they study spin textures in a quantum Hall Ising ferromagnet. Domain walls between ferromagnetic and unpolarised states at ν=2 are analysed with a functional theory supported by a microscopic calculation. They predict that electrons become trapped as solitons at the domain wall. The size and energy of the solitons are determined by both Hartree and spin-orbit interactions. This paper also discuss how electrical transport takes place through the domain wall.
We will not discuss the details of these theories in this thesis as we cannot prove that either one of the theories is right. Instead we focus on the behaviour of the resistance experimentally. In particular we will consider in great detail the anisotropic effects which appear at level crossings when current and in-plane magnetic field directions are varied.

5.4 Sample, setup geometry and experimental method

There has been a report of large anisotropic magneto-transport in Si/SiGe heterostructures where the opposite spin levels from two different valleys coincide [10]. Subsequent studies of high mobility $Al_xGa_{1-x}As/GaAs/Al_xGa_{1-x}As$ wide quantum well (QW) structures with two occupied sub-bands have also shown similar effects [11]. In both experiments only one single Hall bar oriented along one particular crystal direction was studied. A theory has also been developed to explain these results by taking into account the effect of an (isotropic) surface roughness [2], i.e. a non-flatness of the 2DES. Below we outline the experimental method used to study anisotropic effects and compare our results with this theory.

5.4.1 Experimental setup

Since the symmetry breaking groundstates occur below T_c, which is expected to be of order 0.5-1.0 K [49], the measurements were conducted in a cryostat with a ^{3}He insert reaching a base temperature of 250 mK. The measurements were conducted in the linear response regime. L-shaped Hallbar structures were fabricated from the MBE grown samples as described in the previous chapter. The samples are cleaved from a small area at the centre of the wafer to a size which allows two samples, each with similar growth characteristics, to be mounted in the same chip carrier. Sample rotation can be achieved *in situ* at low temperature. In a typical measurement, the 2DES is first placed perpendicular to the magnetic field and magneto-resistance is then measured. This allows characterisation of the sample, i.e. carrier density and mobility can be determined. The sample is then rotated and the magnetoresistance is measured again. As the sample is rotated through a Landau level crossing, a series of curves is obtained as shown in figure 5.4. Figure 5.4a) plots R_{xx} as a function of total magnetic field B_{tot} for a series of different tilt angles close to a Landau level coincidence. The current is directed parallel to the [110] crystal direction and the in-plane magnetic field is parallel to the current. The spike in the resistance develops as the sample is tilted through the crossing. In figure 5.4b), 30 of these data traces are normalised to the perpendicular component of the magnetic field $B_\perp$ and the longitudinal resistance is plotted (in colourscale) versus tiltangle θ and perpendicular magnetic field. The Landau level crossing is clearly identified. Note that the range in angle in which the crossing is seen is rather small. The spike appears and finally disappears in an angle range of only 2°. The sample is then brought to room temperature and rotated by 90°around the normal to the 2DES. The measurement was repeated with the sample in the new orientation, i.e. with the in-plane magnetic field component perpendicular to the current direction (figure 5.4c). By comparing Figures 5.4b) and c), a strong anisotropy can be seen when the in-plane field direction changed. We stress here that this result is completely reproducible from cooldown to cooldown, i.e. we have verified the results in both orientations more than once.

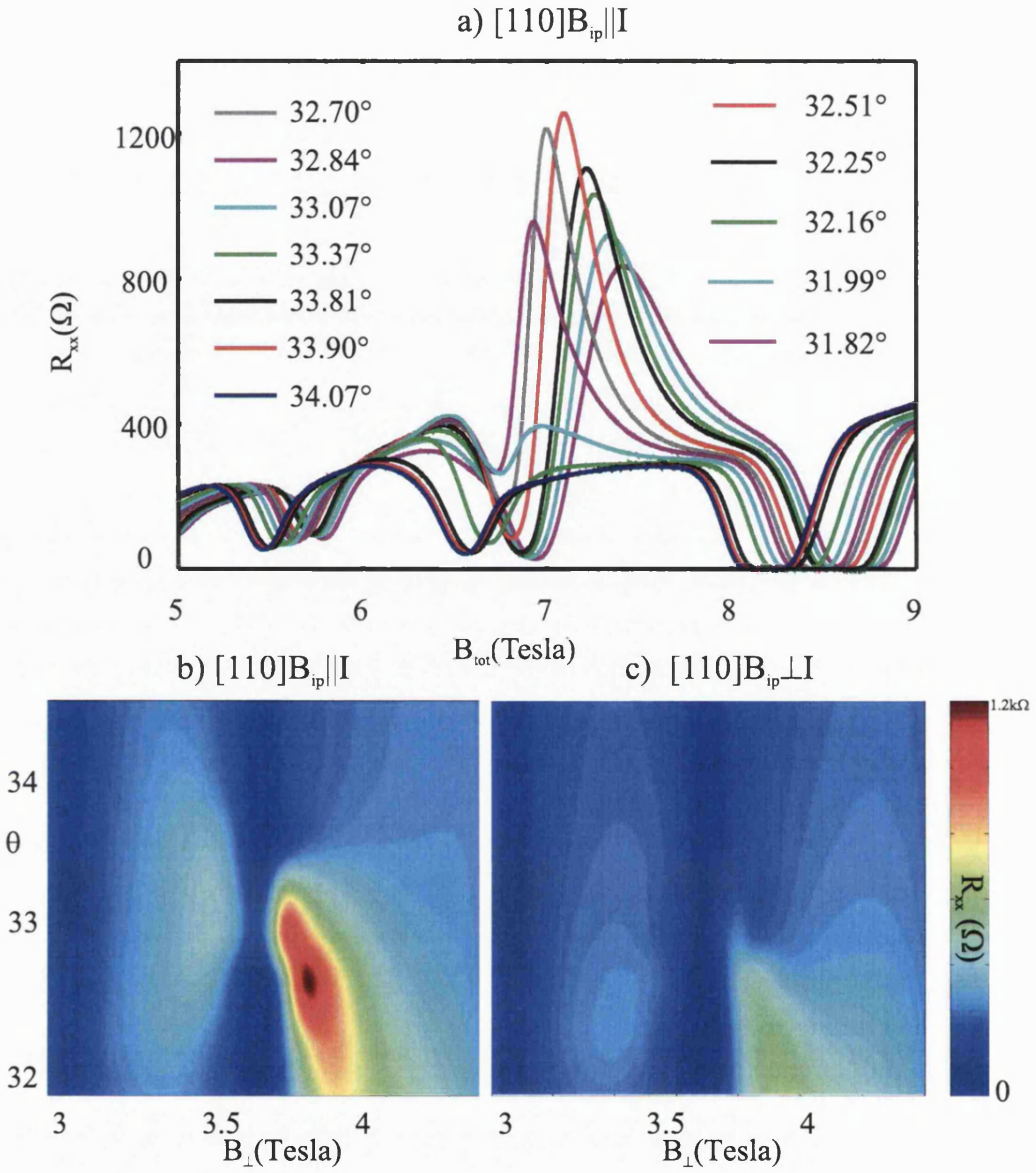

Figure 5.4: a) R_{xx} as function of total magnetic field B_{tot} for a series of different tilt angles close to a coincidence of two Landau levels. b) Colour plot of 30 of such magneto-resistance traces normalised to $B_{\perp}$ versus angle θ and $B_{\perp}$. The value of R_{xx} is indicated on the colour axis. The sample was then brought to room temperature and the chip carrier was rotated by 90°around the normal to the 2DES plane. The measurements were repeated with the sample in the new orientation, i.e. the in-plane magnetic field is now perpendicular to the current. These data are shown in c). A comparison of figure b) and c) reveals a large anisotropy upon rotating the in-plane field by 90°.

5.5 Strong anisotropic effects at $\nu = 5$

The anisotropy is a very strong effect. The resistance can change by a factor of 4 upon rotation of the in-plane magnetic field by 90°. A further investigation is thus required. Since our Hallbars are L-shaped, a better (but not complete) understanding of the anisotropy can be obtained by comparing data for current along [110] and [1$\bar{1}$0] with both in-plane field perpendicular and parallel to the current (giving a total of 4 data sets). These data sets are shown in figure 5.5. Figure 5.6 plots a cut through the data of figure 5.5 that allows an easier comparison.

Figures 5.5 and 5.6 show the resistance data at the $\nu = 5$ crossing. The Landau levels involved in this crossing can be determined from the values of the cyclotron, spin and valley energies as determined in the previous chapter. The Landau levels which in this case cross are the $\langle 0, X, \uparrow \rangle$ and $\langle 2, X, \downarrow \rangle$ levels. In the top of figure 5.5 an AFM scan of the surface of the wafer is seen. As is common for high mobility samples, this surface is not flat, but consists of elongated islands that are approximately 5 nm high, have a width of typically 500 nm along the [110] direction and a length of $\sim$3 μm along the [1$\bar{1}$0] direction. This distinct surface anisotropy arises because adatom diffusion along [110] differs from that along [1$\bar{1}$0]. For the data in column A, the in-plane magnetic field was along the [110] direction, for the data in column B it was along the [1$\bar{1}$0] direction. The middle part of the figure compares the colour-coded longitudinal resistance with current along the [110] direction for in-plane fields parallel (column A) and perpendicular (column B) to the current. These data were previously shown in figures 5.4b) and c) and show a very pronounced anisotropy. In the lower part of the figure, data with the current along the [1$\bar{1}$0] direction is plotted. We compare once more data with the in-plane magnetic field perpendicular to the the current and data with the in-plane magnetic field parallel to the current. This time, a much smaller anisotropy is seen (see also the cuts through the data in figure 5.6). Again, the resistance with the in-plane magnetic field parallel to the current has a larger value than the resistance with the in-plane magnetic field perpendicular to the current. Figure 5.6 plots a cut through the data of figure 5.5 (along the white dashed line) that allows an easier comparison. In the top of this figure, the gradient of the surface in the direction of the in-plane magnetic field is plotted. This gradient was obtained by a numerical differentiation the AFM image.

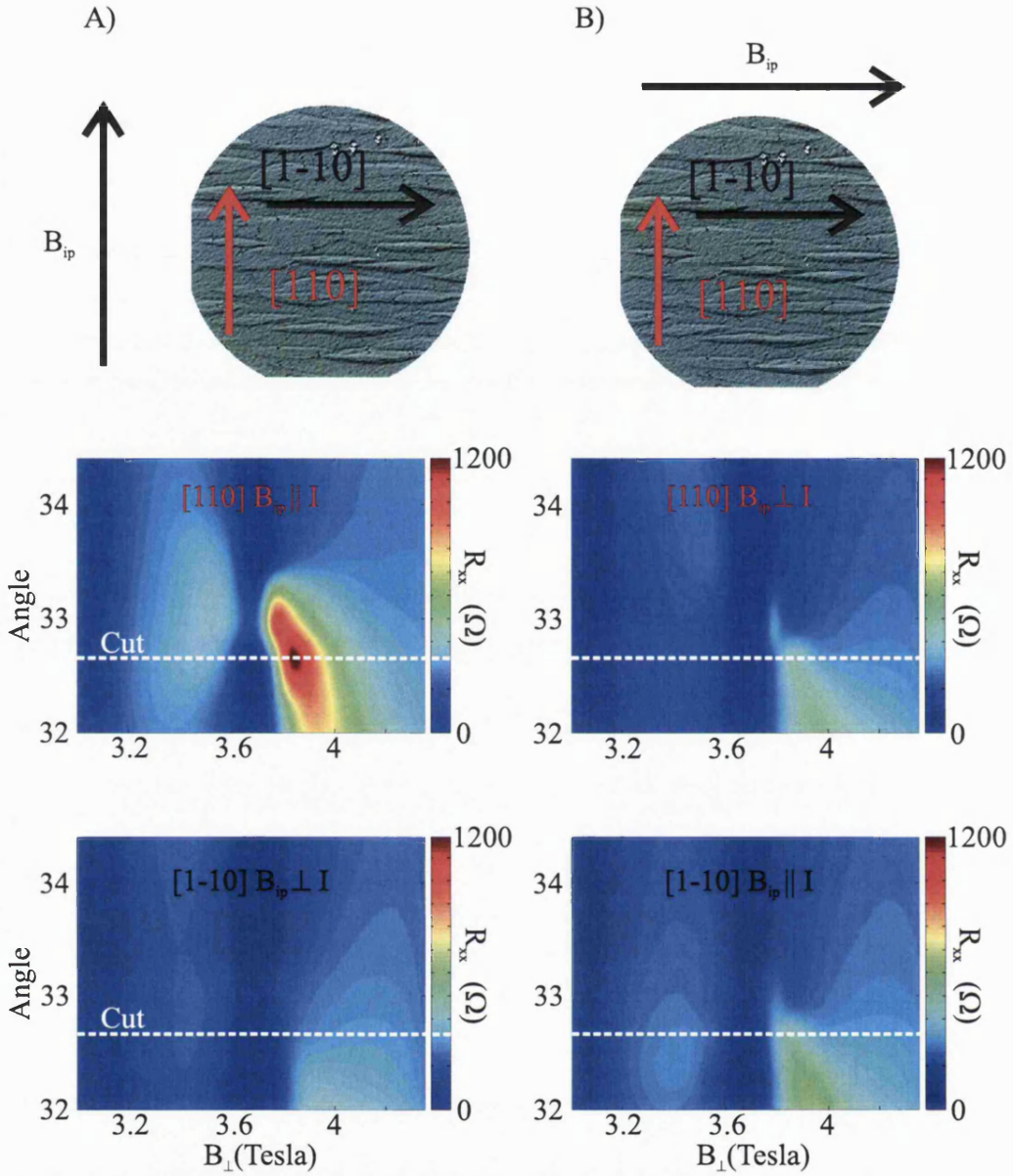

Figure 5.5: Column A) shows the data taken in a set of tilted field measurements as a function of $B_\perp$. The sample was then brought back to room temperature, rotated in the insert by 90°, the tilt mechanism was reset to zero and then returned to base temperature. Column B) shows the data taken subsequently in the new orientation. At the top of each column, the orientation of the current direction relative to the sample surface and the direction of the in-plane magnetic field are shown. The red label corresponds to current along [110] and the black label to current along $[1\bar{1}0]$. Cuts through the data along the white dashed lines are shown, in figure 5.6.

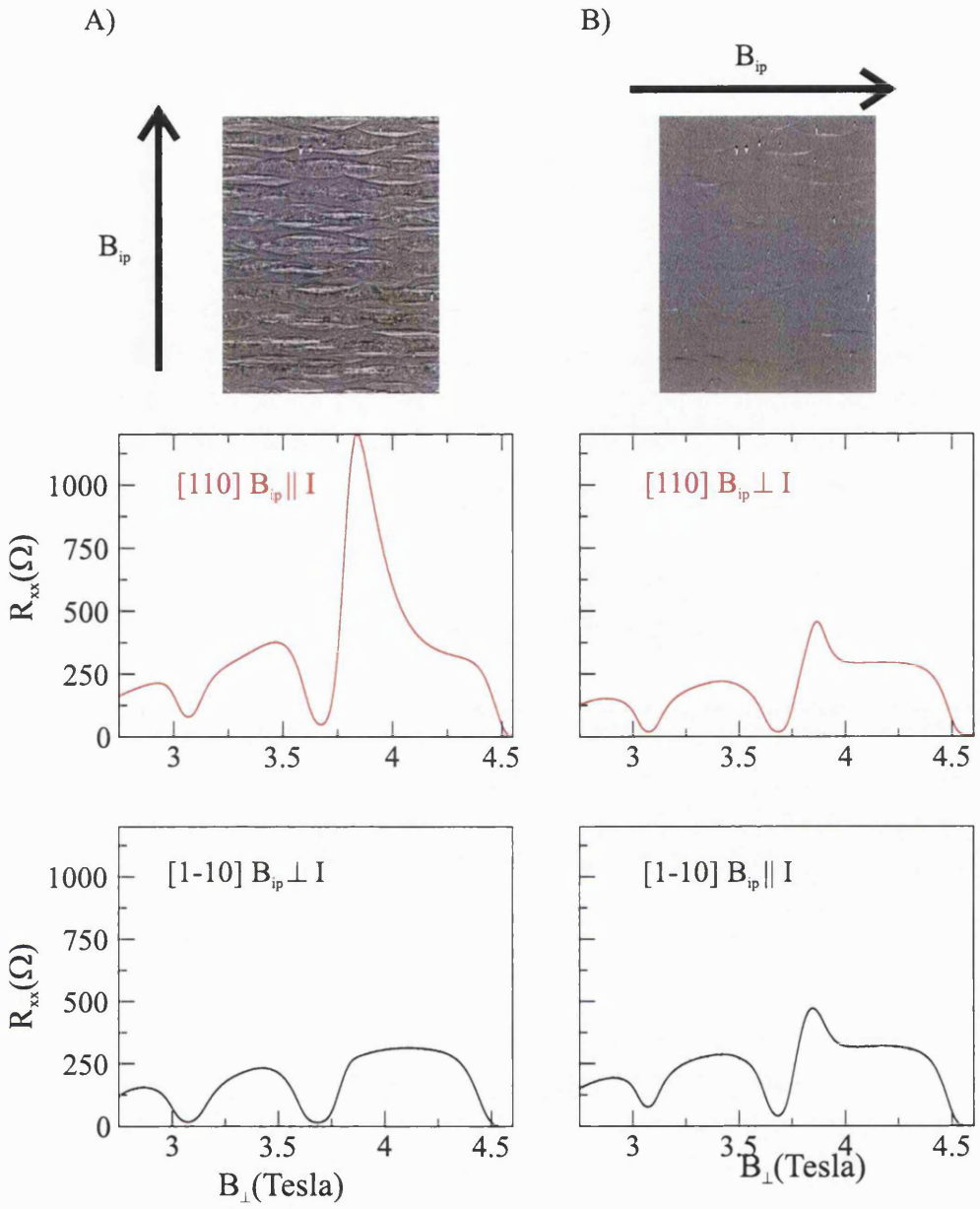

Figure 5.6: The single B-field traces along the white dashed lines indicated in figure 5.5. The upper sections show the gradient of the surface roughness in the direction of the in-plane field obtained from AFM measurements as applicable for each column. Again the plots are colour coded, red for current along [110] and black for current along $[1\bar{1}0]$. This data clearly shows that the resistance is highest when the gradient of the surface in the direction of the in-plane magnetic field is large and the current is parallel to the in-plane field direction. Although difficult to determine quantitatively, this behaviour could be explained in terms of the theory as described by Chalker *et al.*

5.6 Theory of surface roughness

Chalker *et.al* presented a theoretical work [2] that explains the resistance anisotropy observed in previous experiments carried out by other groups [10],[11]. This theory proposes that the transport anisotropy reflects the anisotropic domain formation induced by a random field arising from the (in their case) isotropic surface roughness. It is expected that in a sample (such as those used in this work) with intrinsic anisotropic surface roughness the random field anisotropy will be enhanced. As we have seen in the above (figure 5.6), the resistance is large when the current is forced to flow across the large gradient of the surface in the direction of the in-plane magnetic field (figure 5.6 middle, column A) and small when the current is forced to flow along the small gradient of the surface in the direction of the in-plane magnetic field (figure 5.6 middle, column B). This theory could therefore possibly be appropriate to describe our data.

We recall that in the single particle description one level in the system has the energy

$$E_1 = \left(N + \frac{1}{2}\right)\frac{\hbar e B_\perp}{m^*} \pm \frac{1}{2} \mid g^* \mid \mu_B \frac{B_\perp}{sin\theta} \pm \frac{\Delta_{\text{valley}}}{2} \tag{5.3}$$

and the second

$$E_2 = \left(N' + \frac{1}{2}\right)\frac{\hbar e B_\perp}{m^*} \pm \frac{1}{2} \mid g^* \mid \mu_B \frac{B_\perp}{sin\theta} \pm \frac{\Delta_{\text{valley}}}{2}, \tag{5.4}$$

where E_1 and E_2 are the energies of the two coinciding levels, N and N' are the respective Landau level indices, g^* is the effective g-factor and Δ_{valley} is the valley spitting. The separation of the two crossing levels falls to zero at the coincidence. At a combined filling factor of unity for the crossing levels, the inclusion of exchange interactions leads to a first order transition between ground states in which one or the other level is filled. If we represent the two Landau levels that are crossing by a pseudo-spin, the interactions are ferromagnetic with Ising anisotropy. The total magnetic field now acts on the pseudo-spin as an effective Zeeman field. The theory argues that the anisotropy seen in the measurements can be explained in terms of anisotropic domain formation.

The theory starts with the energy functional

$$E = \int (-DS_z^2 + J \mid \nabla \mathbf{S} \mid^2 + \delta J \mid \partial_n \mathbf{S}(\mathbf{r}) \mid^2 - hS_z) d^2\mathbf{r}, \tag{5.5}$$

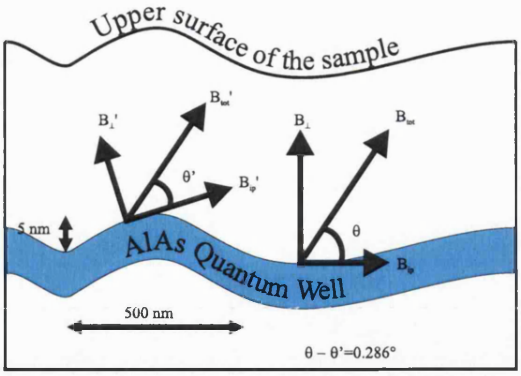

Figure 5.7: Schematic indication of how the non-flatness of the quantum well changes locally the angle between the 2DES and the total magnetic field. As the transition occurs only in a very small range of angles of about 1°, the changes in the local angle of 0.3°induced by the roughness, could have a significant influence on the transport.

where $D > 0$ represents the Ising anisotropy, J is spin stiffness and $\partial_n \equiv \hat{\mathbf{n}}\nabla$ acts in the direction of the in-plane field. δJ represents spatial anisotropy in the spin stiffness. The effective Zeeman field acting on the pseudospins is h. The strength of h varies through zero as the tilt angle θ of the sample varies through the Landau level crossing point. The strength of h depends also on B_{tot} and on carrier density n, but, as is claimed in the theory, the most important source of disorder is randomness in h caused by roughness. Taking h to fluctuate about mean value of zero with amplitude Δ and correlation length $= l$ and supposing l greater than the domain wall width $w = \sqrt{J/D}$, the boundary between the weak and the strong disorder regime lies at $l\Delta \sim \sqrt{JD}$.

For weak disorder, the domain size ξ is much larger than l and domain morphology depends , amongst other things, on the difference in energy per unit length of domain wall parallel or perpendicular to the in-plane magnetic field component. For the case of strong disorder the domain pattern is governed by $sgn(h)$.

It is now necessary to identify a microscopic origin of the random Zeeman field. The theory argues that surface roughness changes the local value of θ and therefore the local value of h. This is schematically outlined in figure 5.7. A surface roughness with an amplitude of $\pm$ 2.5 nm and length of $l \sim 500$ nm, as appropriate for our samples, gives local changes in tilt angle of at least a few tenths of a degree. Note that the experimentally determined range of angle over which the spike is observed is only $\sim$ 1 degree. The random field originating from the surface roughness thus constitutes intermediate to strong disorder. The do-

main formation caused by this mechanism could thus account for the transport anisotropy although it is difficult to determine quantitatively. Note that it is the gradient of the surface in the direction of the in-plane magnetic field that plays the important role. Note also that in our samples this gradient is rather different along the [110] and the [1$\bar{1}$0] directions (see figure 5.6 top). With the above in mind, we now reexamine the data in figure 5.5 and figure 5.6. When the in-plane magnetic field is along the [110] direction, a large gradient with an orientation perpendicular to the in-plane magnetic field appears (see figure 5.6, column A). If the current is now forced to flow along the [110] direction, the theory predicts that the resistance is high. This is indeed observed. When the in-plane magnetic field is along the [1$\bar{1}$0] direction, there is only a small gradient and the resistance with current along the [110] direction should be small. Once more, this is observed in the experiment. On the other hand, when the current is along the [1$\bar{1}$0] direction and the in-plane field is along the [110] direction (column A, bottom), the current flows along the elongated domains and the resistance should be small. This is indeed observed. However, this resistance is still expected to be a bit larger, than that in the situation where the in-plane magnetic field is along [1$\bar{1}$0]. This last prediction is, however, opposite to what we observe in the experiment.

In order to be able to make a more definite statement about the applicability of the theory to our experiment, we have investigated two other Landau level crossings. One with levels arising from different valleys, and one with levels arising from the same valley. Moreover, in an attempt to average out the effect of the anisotropic surface roughness, that could complicate the data analysis, we used Hallbars oriented along the [100] and [010] crystal directions, i.e. along a 45°angle with respect to the anisotropic surface roughness. This assures, that both measurements with the in-plane field parallel to the current and those with the in-plane field perpendicular to the current see the same average gradient of the surface roughness.

5.7 Landau level crossings at ν=6 and ν=7

In this section the crossings between two other pairs of Landau levels is discussed and it is found that the mechanism of the domain formation is not in agreement with the theory presented in the previous chapter. Here we observe the crossings at filling factors $\nu = 6$ and $\nu = 7$. The crossings are observed in the perpendicular

magnetic field region of 2.5 to 3.2 Tesla with the total magnetic field being tilted from the sample normal by 20 to 24°. Using the approximate cyclotron, Zeeman and valley energies as determined in the previous chapter, we identify the crossing levels. At ν=6 the N=0 spin down Landau level from the lowest energy valley crosses the N=2 spin up Landau level from the higher energy valley. At ν=7, the N=0 spin down Landau level from the lowest valley crosses the N=3 spin up Landau level of the same valley.

The sample for this experiment was cut from the same wafer as the samples in section 5.5 but now the L-shaped Hallbar is structured such that the two current directions are along [010] and [100]. A topographic image of the surface is shown together with a diagram of the sample layout in figure 5.8a). Note that the sample layout is different now: the two current directions are now oriented at an angle of 45°with respect to the characteristic roughness orientation. The gradient of the surface roughness along the [010] and the [100] directions is thus very similar. The measurements were conducted under similar conditions as those presented in the previous section. Colour-coded resistance measurements for several combinations of in-plane field, tilt angle and current directions are shown in the five panels c) to g) of figure 5.8.

The main finding is that for neither one of the crossings the theory is applicable. Moreover, the anisotropy in the longitudinal resistance is different for both crossings. At ν=6 we observe that the large resistance spike appears when the in-plane magnetic field is perpendicular to the direction of the current flow, while virtually no enhanced resistance is measured when the in-plane magnetic field is parallel to the current. For the transition at ν=7 on the other hand, the resistance spike is measured when the in-plane magnetic field is parallel to the direction of the current flow, and virtually nothing is seen when the in-plane magnetic field is perpendicular to the current. This observation holds both for transport along the [010] direction and for transport along the [100] direction. To check that for both orientations of the in-plane magnetic field, the crossing of the levels is present (i.e. to exclude possible orbital effects caused by the in-plane magnetic field), we also measured a complete set of data with the in-plane magnetic field along the [110] direction, i.e. under 45°with respect to the current direction. In this case both transitions can be seen simultaneously, which excludes orbital effects.

For example, let us consider panel c). Here the in-plane magnetic field is parallel to the current that is oriented along the [010]-direction. The crossing at ν=7

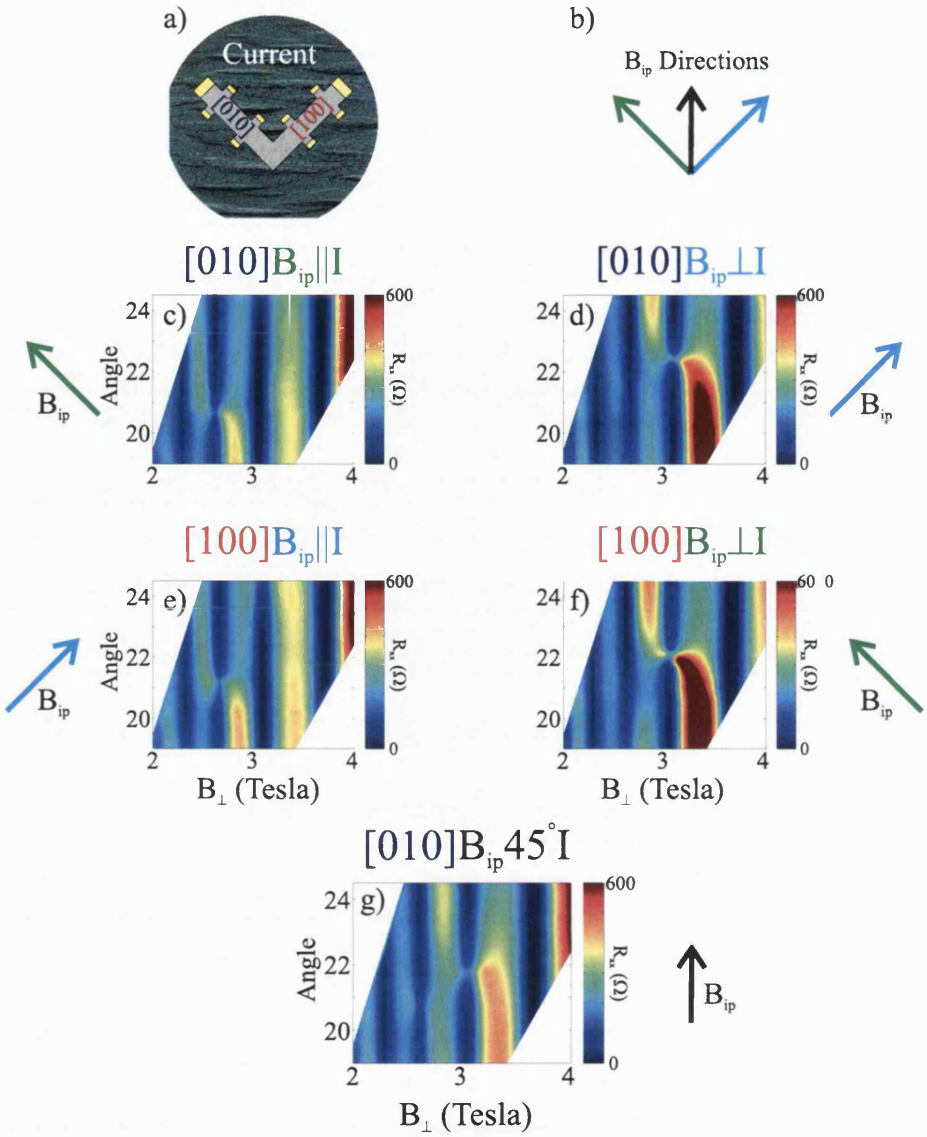

Figure 5.8: a) Orientation of the sample with respect to the surface roughness. The current directions are colour coded and this colour coding is also used in the following figure labels. b) Colour coding of the direction of the in-plane field. This colour coding is also used in the figure labels. c) and d) plot data for current along the [010]-direction. In c) the in-plane B-field is parallel to the current and a Landau crossing is clearly visible at $\nu = 7$ (at 2.6 Tesla and 20.8°). Simply changing the in-plane B-field direction such that it is perpendicular to the current, gives the result shown on in d). Here the Landau level crossing at $\nu = 7$ is hardly visible. Instead a clear crossing is now observed at $\nu = 6$ (at 3.2 Tesla and 22.2°). In e) and f) identical behaviour is observed for current along the [100]-direction. Using a simple symmetry argument, it can be assumed that both crossings should be visible when the in-plane field is applied at 45°to both current directions. This is indeed observed in g) where the in-plane field is along the [110]-direction.

is clearly visible at 2.6 Tesla and 20.8°. This anomaly is much smaller (if not invisible) when the in-plane magnetic field is oriented perpendicular to the same [010] current direction, as is seen in panel d). In panel d) on the other hand, we now see a large resistance anomaly at ν=6 at 3.2 Tesla and 22.2°. This ν=6 crossing can hardly be observed in the data in panel c).

Panels e) and f) reproduce the same result but now the current is driven along the [100]-direction. In panel e) the in-plane magnetic field is parallel to the [100]-direction and we predominantly see the $\nu = 7$ structure as seen in c). This is expected because the situations of c) and e) are equivalent, i.e. both have the in-plane magnetic field in the direction of current-flow. Similarly, panel f) strongly resembles panel d), which are also equivalent situations, i.e. in-plane magnetic field is perpendicular to the direction of current-flow.

To check that the level crossings at ν=6 and ν=7 are present in all the above situations (i.e. that the level scheme is not dependent on the direction of the in-plane magnetic field), we have measured a complete set of data with the in-plane magnetic field under a 45°angle with respect to the current. Indeed, in panel g) we observe the level crossings a both $\nu = 6$ and $\nu = 7$ simultaneously, proving that orbital effects do not play a role.

From the above theory and from most of the results in the previous section, one would have expected that the domain formation would be the same for the two current directions, since the gradient of the surface roughness in the direction of the in-plane field is the same. The $\nu = 6$ and the $\nu = 7$ Landau level crossings should have thus shown a similar resistance anomaly for all experimental situations of figure 5.8, except possibly for the data of panel g). Since this is clearly not the case, at least one other ingredient is needed to explain the data.

The data in this figure indicates that the surface roughness is not the most important factor for the domain formation. Instead, when this surface roughness is averaged out, we find that the direction of the in-plane field with respect to the current alone is relevant. To complicate matters more, the direction of the domains seems to be along the in-plane magnetic field for the ν=6 Landau level crossing but perpendicular to the in-plane magnetic field for the ν=7 Landau level crossing.

It is not possible to make any definite statement about the relevant difference

between the three Landau level crossings studied. All three crossings involve levels with opposite spin directions. We note here that for the odd filling factor crossings at $\nu = 5$ and $\nu = 7$ two identical valley quantum numbers are involved, while for $\nu = 6$ the crossing levels originate from different valleys. The $\nu = 7$ crossing differs from the other two because the Landau indices of the crossing levels are N=0 and N=3, while the other two crossings involve Landau levels with quantum numbers N=0 and N=2.

One possible explanation for the behaviour of this system could be contained in the interaction of electronic orbitals. In tilted magnetic fields the ellipticity of the orbitals varies as a function of the tilt angle relative to the Fermi surface axis. The rate at which two Landau levels cross each other is therfore a function of the change in the ellipticity of the two involved orbitals.

5.8 Width dependence of the strong resistance spike at ν=5 observed with current and in-plane field along [110]

In the above the resistance maximum at the Landau level crossings was attributed to the separation of the 2DES into domains. The domain boundaries were considered to be the source of the high resistance. The size of the domains is completely unknown, in fact there is no direct proof that distinct domains really exist, since no imaging technique was ever applied to this resistance anomaly. In an attempt to estimate the possible domain size, we have studied Hall bar samples with varying widths down to 2 μm. We hoped to observe large changes in the amplitude of the resistance peak, when the sample width becomes comparable to the characteristic domain size.

For this study, we fabricated Hall bars with a width of 10, 5, 3 and 2 μm. 2 μm is the smallest possible size achievable with contact mask optical lithography. The distance between the voltage probes L was 10 μm. The Hall bars were fabricated from a different wafer but the 2DES of this wafer had a comparable density as the previous samples. The $\nu = 5$ crossing in this wafer is observed at 5 Tesla and at an angle of 32°. We studied only the current direction along [110] and the in-plane magnetic field was applied parallel to the current. This is the situation

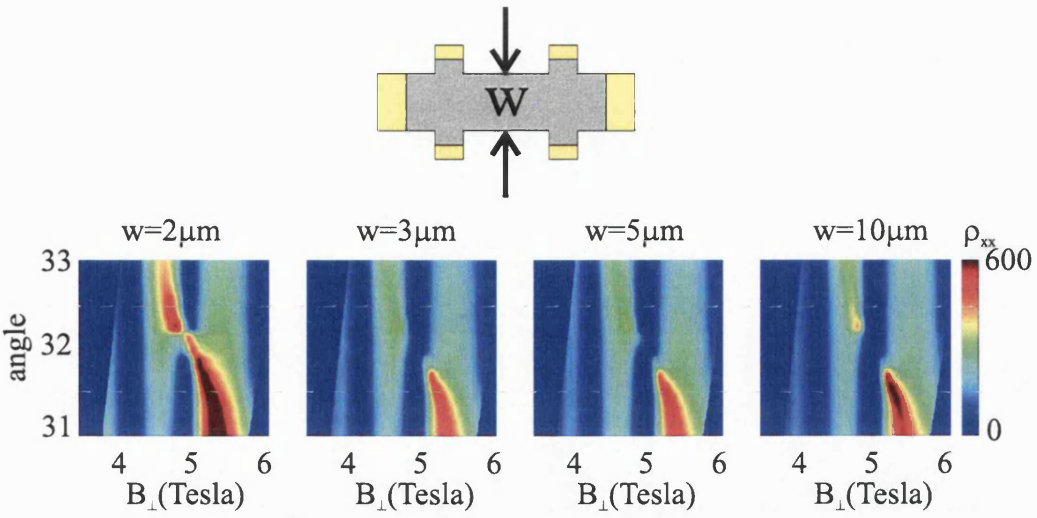

Figure 5.9: The width dependence of the longitudinal resistivity for a range of Hall bar widths. The data indicate that between 2μm and 3μm Hall bar width, there is a strong increase in ρ_{xx} at the crossing. This preliminary data set shows that further investigations should be conducted to obtain details of domain structure and size.

for which the resistance anomaly was the strongest (see section 5.7).

Figure 5.9 plots the colour coded longitudinal resistance as a function of perpendicular magnetic field and tilt angle. The four panels correspond to the four sample widths studied. The first observation is that the resistance anomaly is clearly visible in all four samples. The detailed behaviour of the resistance peak, however, varies drastically from narrow to wide Hall bar widths. The peak is strongest for the narrowest sample. Moreover, it is striking to see how the resistance peak causes the disappearance of the ν=5 quantum Hall effect minimum with decreasing sample size.

Although there is clearly a size effect on the amplitude of the resistance spike observed at the transition, it is not straightforward to extract a domain size from these experiments. Naively, one would have expected that the resistance changes in steps depending if one or several domain boundaries just fit into the sample width. Such behaviour can be observed between 2 μm and 3 μm width Hallbars. However, the data for 3 to 10 μm are very similar. If the characteristic domain size would be of order 2 μm, they should however, still show some change. Therefore further studies on narrower samples with smaller distance between the voltage probes are needed.

5.9 Conclusion

The resistance anomalies at three crossings of Landau levels in AlAs 2DES Hall bar structures were studied by measuring the longitudinal resistance along four different crystal directions with currents both perpendicular and parallel to the applied in-plane magnetic field. Our AlAs samples display significant anisotropic surface roughness. The experimental results are compared with a theory that takes this surface roughness into account. Not all experimental findings are in agreement with this theory. Our experimental findings are summarised below.

- The resistance peaks at filling factors $\nu = 5$, $\nu = 6$ and $\nu = 7$ were studied.
- All these peaks were found to be strongly anisotropic, i.e. the resistance changes significantly if the in-plane magnetic field is rotated by 90°.
- At $\nu = 5$ the maximum resistance was observed for current along the [110]-direction when the in-plane field was applied parallel to the current.
- At $\nu = 6$ the resistance peak was largest when the in-plane field was applied perpendicular to the current. This is observed for both [100]- and [010]-current directions.
- At $\nu = 7$ the resistance peak was largest when the in-plane field was applied parallel to the current. This is observed for both [100]- and [010]-current directions.
- The $\nu = 5$ result is in qualitative agreement with a previous theory that considers the interplay of surface roughness and in-plane field.
- The $\nu = 6$ and $\nu = 7$ results are not covered by this theory because the current directions were chosen such that the magnitude of the gradient of the surface roughness was identical for all measurements.
- The results indicate that the surface roughness is not the main cause of the observed anisotropies.
- At $\nu = 6$ and $\nu = 7$ the direction of the in-plane field determines the domain orientation.
- The domains at $\nu = 6$ and $\nu = 7$ appear to be orientated perpendicular to each other for the same in-plane field orientation.

- The sample size affects the magnitude of the resistance peaks which become larger with decreasing sample width.

Part III

Coupled 2D electron-hole systems

Chapter 6

Coupled Two Dimensional Electron-Hole Systems

Abstract

This chapter discusses the fabrication of coupled 2D electron-hole systems with a non-equilibrium technique by means of focused ion beam implantation during a MBE growth interrupt. By applying a bias of order of the bandgap between the n and the p-sides of the sample, the 2D systems can be induced. Coupled electron-hole systems are of interest, since at low temperatures and at low and equal densities the electrons and holes will form (indirect) excitons. At low temperatures these excitons are predicted to undergo condensation into a superfluid through a Kosterlitz-Thouless phase transition[53].

6.1 The samples

Three types of samples were fabricated. In the first type of sample, the FIB is used to isolate certain areas of a p-doped buried layer, in order to fabricate separate contacts to the lower 2D hole system. Shallow n-contacts to the upper 2D system are made by alloying very thin NiAuGe contacts. Both the quality of the 2DHS and that of the 2DES are good in these samples. Furthermore, the

high quality of the barrier allowed samples to be successfully characterised by means of transport and capacitance measurements. The data show clearly that the simultaneous existence of electron and hole systems is possible, exactly as predicted. However low and equal densities cannot be achieved with this type of sample, since the 2D hole system accumulates at a lower interlayer bias than the 2D electron system. The backgate turned out to be of limited use, since it is likely that the field lines end on poorly mobile charges in the implanted region. This successful experiment provided the necessary information to allow the continuation of this work and the design of the sample was then reconsidered using the results obtained.

For the second type of sample, the FIB is equipped with a custom built Au/Si/Be source and the p-contacts are directly implanted during the MBE growth interrupt. Despite many attempts, the subsequent overgrowth always produced a barrier between the 2D hole and the 2D electron system that was not of sufficient quality. Secondary ion mass spectroscopy showed that this is due to segregation of the implanted Be ions with the growth front during the overgrowth.

For the third type of sample, the structure is "inverted", i.e. the 2DES is now the lower 2D system. The FIB with the custom built source is used to directly implant the n-contacts with Si. This produced a barrier of sufficient quality after overgrowth. Shallow p-contacts that do not diffuse through the barrier turned out to be very difficult to fabricate. Contacts were fabricated to the 2DHS by means of a so-called tunnel-contact of TiAu that was deposited on an extremely heavily p-doped top layer ($>5 \times 10^{19}$ cm^{-3}). This top layer contacts a less heavily doped layer, which contacts the undoped layer that in turn contacts the 2DHS. Various test structures were grown, and every individual step of the fabrication has been checked successfully. This project required the development and optimisation of many different technologies which must be integrated in order to achieve useful sample fabrication. Due to challenges of high mobility MBE growth and the limited quantity of custom made FIB source material, only one full sample was grown and awaits to be measured.

6.2 Theory of exciton condensation

An exciton is a quasi-particle that can be thought of as an electron and a hole in a bound state. This is similar to the case of the hydrogen atom but here the proton in the nucleus is now replaced by a hole. When the density of an exciton gas is low, $na_B^d \ll 1$ (where n is the exciton density, d the dimensionality and a_B the exciton Bohr radius), the excitons can be considered as weakly interacting Bose particles. Condensation of these particles is analogous to the Bose-Einstein condensation of 3D bosons [54, 55]. At the other end of the density scale when $na_B^d \gg 1$ the excitons are analogous to Cooper pairs except that the coupling between electrons and holes is Coulombic and not phonon mediated. In this case theory shows that the exciton condensate is insulating, the so-called excitonic insulator. This state is analogous to the BCS superconducting state [56, 14] except that due to the charge neutrality of e-h pairs the state is insulating. Condensation occurs when excitons are cooled below a critical temperature (T_c) in the low density case. T_c is proportional to $1/m_x$ (where m_x is the boson mass, in this case the exciton mass). As the excitons in a semiconductor are much lighter than the Alkali atoms, condensation should occur at much more elevated temperatures.

In many optical experiments, excitons are produced that have excess energy and the exciton temperature can greatly exceed that of the lattice. The exciton temperature is then determined by the ratio of exciton relaxation rate to exciton recombination rate. Therefore systems with a long exciton lifetime are selected to allow lowest exciton temperature. Within this Ph.D project recombination must also be low. This is achieved by having minimal leakage current through the barrier so that all recombination is indirect and thus very inefficient. Furthermore, compared to optical systems the lifetime of the excitons in our samples is $\approx 10^5$ higher than that in the optical experiments.

Theory predicts that the system of indirect excitons can condense into a superfluid. This condensation should occur through a Kosterlitz-Thouless phase transition with the transition temperature T_c given by $\pi\hbar^2 n_s/2k_B\mu$; n_s is the density of electron-hole pairs and μ their effective mass [57, 58]. For a density of 10^{10} cm^{-2}, a hole mass of 0.5 m_0 and an electron mass of 0.067 m_0 appropriate for the AlGaAs system, this T_c is 2.35 K. This is within the measurable limits and allows a number of experiments to be carried out since the carrier density in the two layers of our sample can be controlled by the use of front and back gates.

6.3 MBE growth and FIB implantation of the first type of 2DES-2DHS samples

A diagram of this sample structure is shown in figure 6.1. First a 500 nm GaAs buffer layer followed by 100 nm Si-doped (2×10^{18} cm^{-3}) GaAs layer to act as a n-doped backgate is grown. A second buffer of 300 nm undoped GaAs and a 100 nm C-doped (2×10^{18}cm^{-3}) GaAs layer for the production of p-contacts are grown. An As_2 cap layer, which finalises the first growth sequence, is produced with a GaAs cracker cell at 830 °C with a shutter time of 30 seconds. The As_2 cap protects the surface of the sample from contaminants such as carbon during the transfer of the sample through a UHV ($\approx 10^{-10}$ bar) transfer tunnel to the FIB chamber. Using the FIB, Si-ions are locally implanted. The ions penetrate the As_2-layer and overcompensate the C-doping, producing selective isolation in the implanted regions. Au alignment markers are also implanted for alignment in subsequent processing steps. The sample is then transferred back to the growth chamber and the As_2-layer with almost all contaminants that have adsorbed onto it during transfe, is evaporated as the sample is returned to growth temperature. Then 300 nm GaAs with C-doping gradually decreasing from 10^{17} to 5×10^{16} cm^{-3} is grown, followed by 40 nm undoped GaAs. Next a 14, 15 or 20 nm $Al_{0.8}Ga_{0.2}As$ barrier is grown followed by 50 nm undoped GaAs and a 300 nm GaAs layer with Si-doping gradually increasing from 10^{16} to 10^{17} cm^{-3}. The overgrowth sequence is finalised by growing 200 nm Si-doped (2×10^{18} cm^{-3}) GaAs.

After growth the sample must be annealed with the Rapid Thermal Annealer (RTA) to 800 °C for 5 s to activate the implanted Si ions. The annealing must be carried out with the sample sandwiched between two pieces of undoped GaAs wafer; this prevents the As on the surface of the sample from evaporating. After many tests ($\approx$ 20 wafers), this optimised design was reached. A photomicrograph of the e-h sample, from above, is shown in figure 6.2. Contact pads for the upper and lower 2D system are indicated. The front gate pad metalisation extends over the length of the mesa. The back gate contact is not shown in this picture.

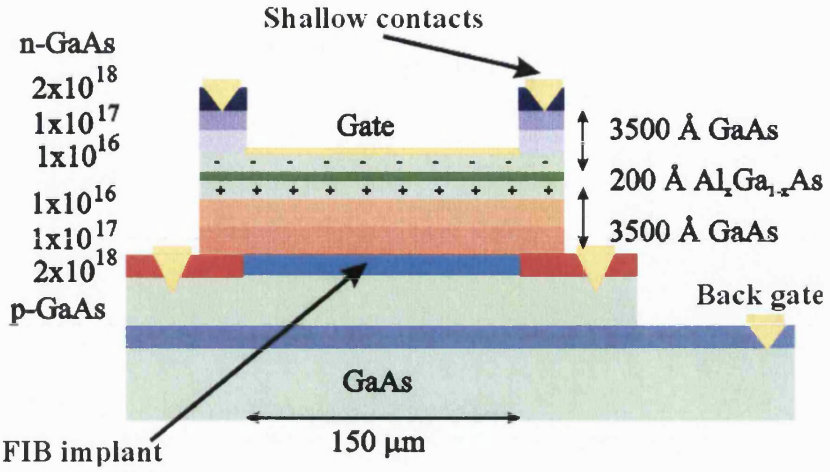

Figure 6.1: Schematic optimised layer composition for the coupled 2D e-h samples. During an MBE growth interrupt, the FIB is used to isolate certain areas in the buried p-doped bottom layer. After overgrowth the sample is processed and standard p-contacts and shallow n-contacts are used to contact the 2D hole and 2D electron systems, that appear upon application of a bias (of order the bandgap) between the p and n-contacts.

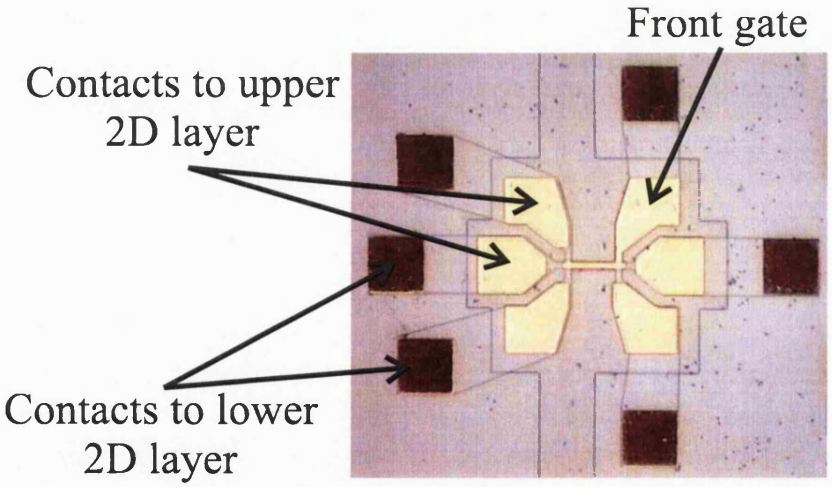

Figure 6.2: Photograph of the e-h sample. Contacts for the upper and lower 2D system are indicated. The front gate extends over the length of the mesa. The back gate contact is not shown

6.3.1 Testing the samples

The first stage of testing is at 4.2 K without magnetic field. This is completed in a ^{4}He dewar; the sample is placed in a measurement head and slowly cooled in the ^{4}He liquid. The contact resistances are measured using a source measure unit (Keithley 236 SMU). The breakdown voltage of the barrier is measured, i.e. the voltage at which a leakage current appears is determined. The interlayer leakage current for the 15 nm barrier samples was $\approx$ 300 pA/mm^2 at 1.6 V. This corresponds to a tunnelling lifetime of 0.4 s, which is more than 5 orders of magnitude larger than the lifetime of excitons in a typical optical experiments. For the 20 nm barrier samples tunnelling lifetimes in excess of 15 s were obtained, while excitons in the 14 nm barrier sample still had a lifetime of 0.05 s. All in all, very good barriers are produced.

For the next test the transistor characteristics of both the *n*- and *p*-channels are measured with different interlayer voltages applied (see figure 6.3). These tests are only preliminary and are used to ascertain that the sample is of sufficient quality to study further. All three acceptable wafers (with 20, 15 and 14 nm thin barriers) have been tested. An example of the transistor characteristics of the 15 nm barrier samples is shown in figure 6.3. Both *p*-channel and *n*-channel contacts are Ohmic, evident by the initial linear increase of the current with source-drain voltage V_D. The sample behaves as a perfect enhancement mode transistor. It is also noted that the holes accumulate at the barrier at $V_{Gate} \approx -1.53$ V; a much lower voltage than that required for the electrons (-1.60 V). This means that above the implanted region the hole density at a certain V_{Gate} will be higher than the electron density.

A backgate was included in the structure to allow the hole layer density to be tuned. This backgate, however, was only isolated from the *p*-contacts up to bias voltages of 0.3 V, which corresponds to the Schottky barrier between the Au/Zn/Au contacts and the *n*-doped backgate. For larger biases, current starts to flow between the backgate and the *p*-contacts. With 0.3 V however, the hole density is hardly influenced, probably because most of the field lines end on poorly mobile charges in the FIB-implanted region between the backgate and the 2DHS (see figure 6.1). Matched and low densities can thus not be produced with this sample design.

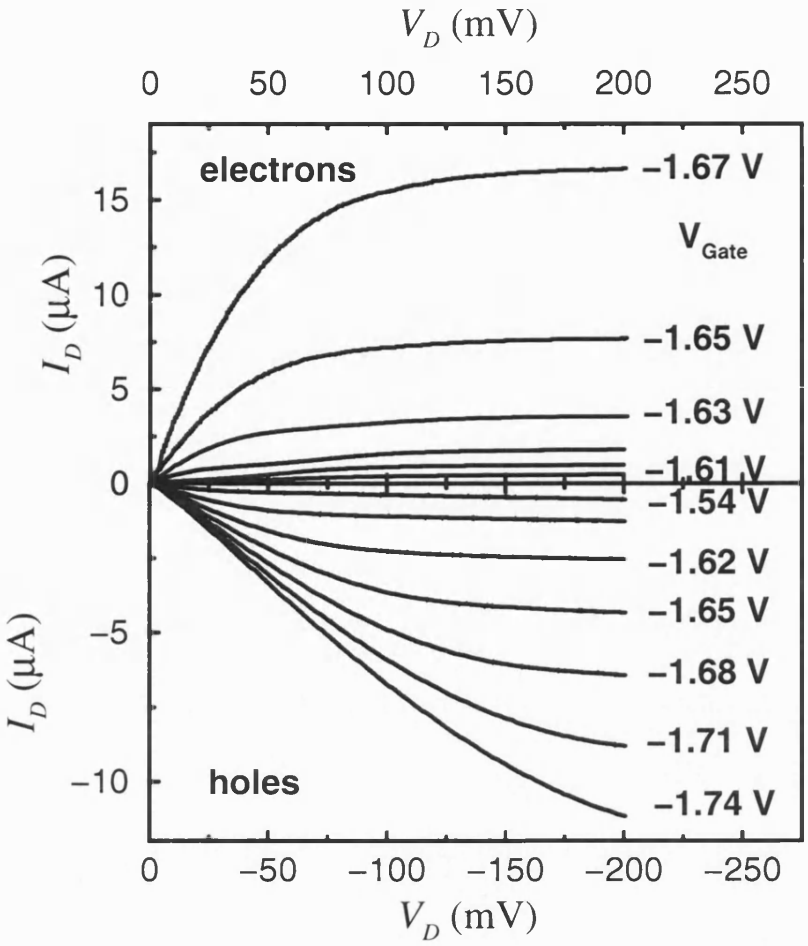

Figure 6.3: Transistor characteristics of both n and p-channels of an e-h sample. The structure behaves as a perfect enhancement mode transistor.

6.3.2 Characterising the samples

The quality of the 2D systems was characterised by measuring the mobility as a function of carrier density. By measuring ρ_{xx} and ρ_{xy} versus magnetic field, the mobilities and the carrier densities of the layers can be determined. An example of a ρ_{xx} and ρ_{xy} versus magnetic field plot from the 2DHS of the 20 nm barrier sample, for one particular inter-layer bias, is shown in figure 6.4. At low fields $R_{xy} = 1/nq$, with n the carrier density and q the charge of the carriers. R_{xy} can thus be used to determine the carrier density. The mobility can then be

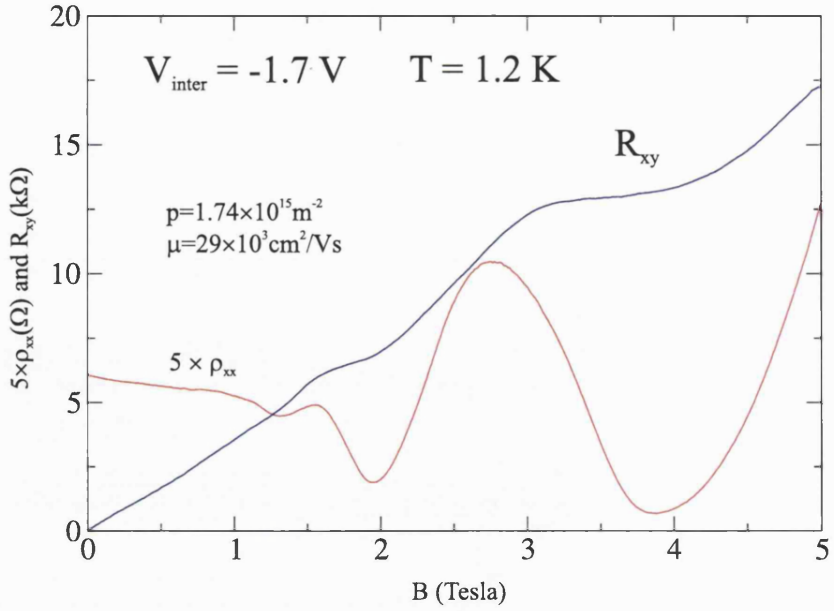

Figure 6.4: Longitudinal resistance (red) and Hall resistance (blue) of the 2DHS versus magnetic field at an interlayer bias of 1.7 V and a temperature of 1.2 K. From the Hall resistance the carrier density is determined and from the zero field longitudinal resistance the mobility is then calculated.

determined from the longitudinal resistance. It is given by

$$\mu = \frac{\mathrm{R}_{xy}(1\mathrm{T})}{\rho_{xx}(\mathrm{B}{=}0)}. \tag{6.1}$$

By repeating the ρ_{xx} and ρ_{xy} versus magnetic field sweep for a range of interlayer bias voltages, the mobility versus carrier density plot shown in figure 6.5 was produced. This plot shows the mobility versus carrier density of both the 2DES and 2DHS. We note that both 2D systems are present simultaneously, but that for each density point the electrons need a slightly larger interlayer bias than the holes. The density in each of the 2D systems were varied by connecting the gates to the respective source contacts and changing the interlayer bias. At carrier densities below 2×10^{15} m^{-2}, the hole mobility is proportional to $n^{0.77}$ and it displays a maximum around 3×10^{15} m^{-2}. Such power law behaviour is commonly observed in high mobility samples and values of the exponent below 1 indicate that the dominant scattering mechanism is remote impurity scattering. The electron mobility also follows a power law behaviour. However its exponent is higher (≈ 1), most likely because the electron system forms at the inverted interface or because local impurity scattering has a significant effect. The absolute

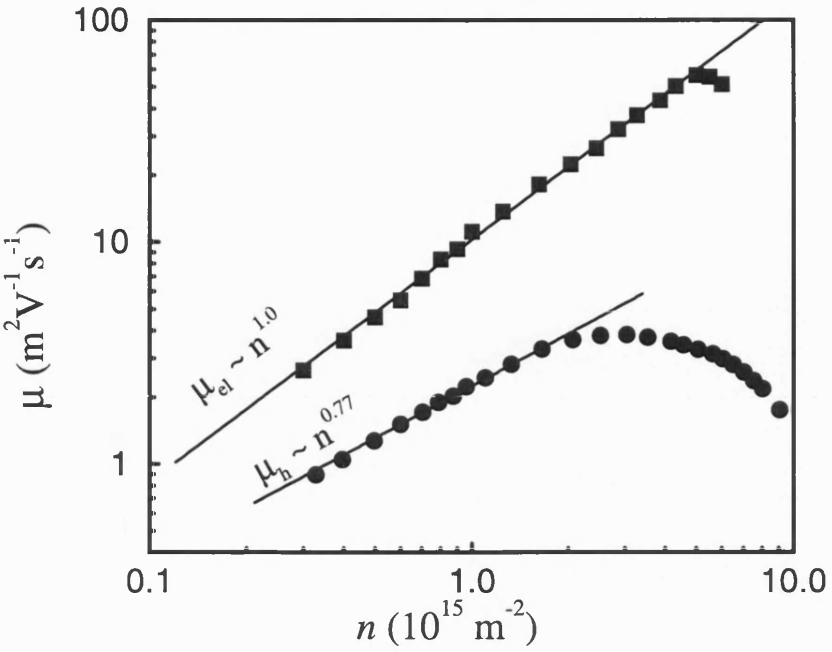

Figure 6.5: Mobility versus carrier density of both 2DES and 2DHS at 1.2K. Below densities of 3×10^{15} m^{-2}, the hole mobility follows a power law with exponent of 0.77 indicating remote impurity scattering as the dominant scattering mechanism. For electrons the power law is observed over the entire range of density, but its exponent is higher, indicating interface scattering or direct impurity scattering as the dominant scattering mechanism.

value of both the electron and hole mobility in these structures is $\approx$ 50-70 % of those obtained in our optimised standard single 2D heterostructures grown in the same MBE-machine.

6.3.3 Capacitance measurements of coupled 2D electron-hole samples

In order to obtain directly information about the density of states of the 2D systems in the structure, on the best samples, the capacitance versus interlayer voltage characteristics were determined. To this end the capacitance was measured in a bridge geometry (see figure 6.6) through a full phase analysis of the measurement signal. An AC measurement voltage (0.1-1 mV) was superimposed on the DC interlayer bias voltage ($\approx$ 1.6 V) through an adder and measurement frequencies ranged from 30 to 420 Hz. In the samples with a metal front gate,

$C_{vgl} \approx C_{Probe} \approx 200$ pF - 1 nF

$f = 30$ - 500 Hz

$V_{AC} = 1$ mV

$R_m = 10$ - 100 kΩ

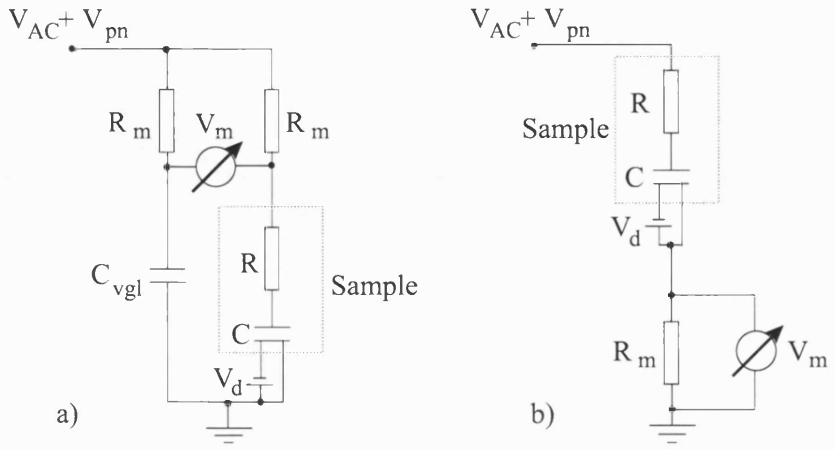

Figure 6.6: Schematic drawing of the two set-ups used to measure the capacitance of the coupled 2D electron-hole system as a function of interlayer bias, magnetic field and temperature.

the front gate was on the same potential as all the electron contacts and the back gate was shorted to all hole layer contacts.

Figure 6.7 plots the capacitance in zero magnetic field of the full 20 nm barrier sample (dotted line). It is compared with a sample (SISFET) fabricated from the same wafer but from a piece that is not implanted with the FIB, i.e. this sample has only one contact to the 2D hole system. The full sample displays two treshold voltages: one around -1.54 V which corresponds to the bias at which the 2DHS forms as determined from the transistor characteristics (see figure 6.3) and one around -1.62 V at which the electrons accumulate. The SISFET without implantation on the other hand, displays only one threshold. This implies that both 2D system form simultaneously. Note that since the areas of both samples is not the same, the absolute magnitude of the capacitance differs in this plot.

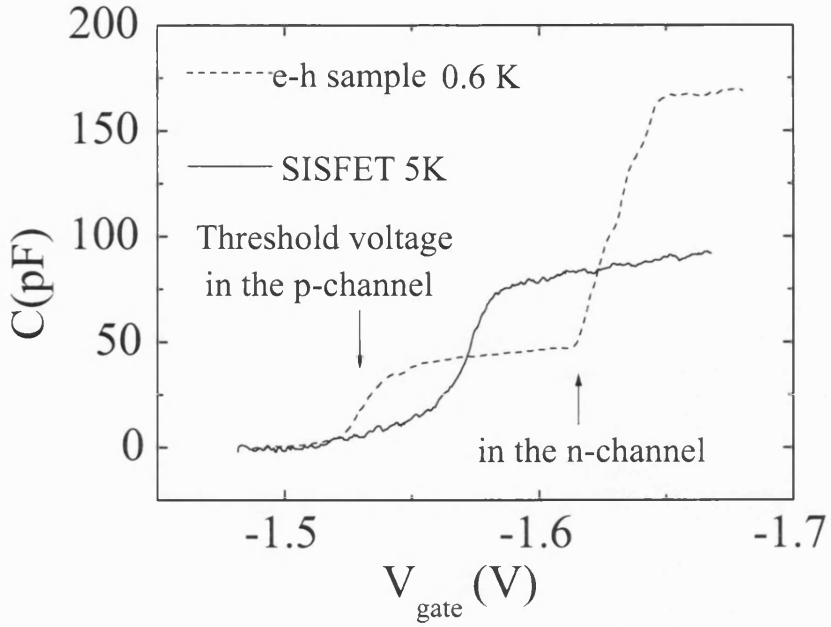

Figure 6.7: Capacitance versus interlayer voltage showing that the accumulation of holes occurs at a lower interlayer voltage than that of electrons in the full e-h sample (dotted line). In the test samples without implantation (SISFETs) only one threshold is observed, i.e. holes and electrons accumulate simultaneously.

6.3.4 Magneto-capacitance measurements of coupled 2D electron-hole samples

The longitudinal resistance of the 2D systems depends only on the density of extended states. The capacitance, on the other hand, depends on the true thermodynamic density of states, i.e. it also includes the density of localised states and possible interaction effects. Therefore magneto-capacitance data were measured on the full coupled 2D electron-hole samples. Figure 6.8 plots the magneto capacitance of a 15 nm barrier sample for various interlayer voltages, i.e. for various densities of the 2D systems. Even at a low interlayer bias of -1.60 V, clear 1/B periodic oscillations are seen, signalling the quantisation of the density of states into Landau levels. From the periodicity of these oscillations, the carrier density is determined. This is compared with the densities obtained from the Hall resistance data measured on each of the 2D systems. It is found that the oscillations in the capacitance are due to the density of states of the electrons and that no oscillatory component due to the hole system is present (note that at a fixed interlayer bias, the hole density is higher than the electron density). This is

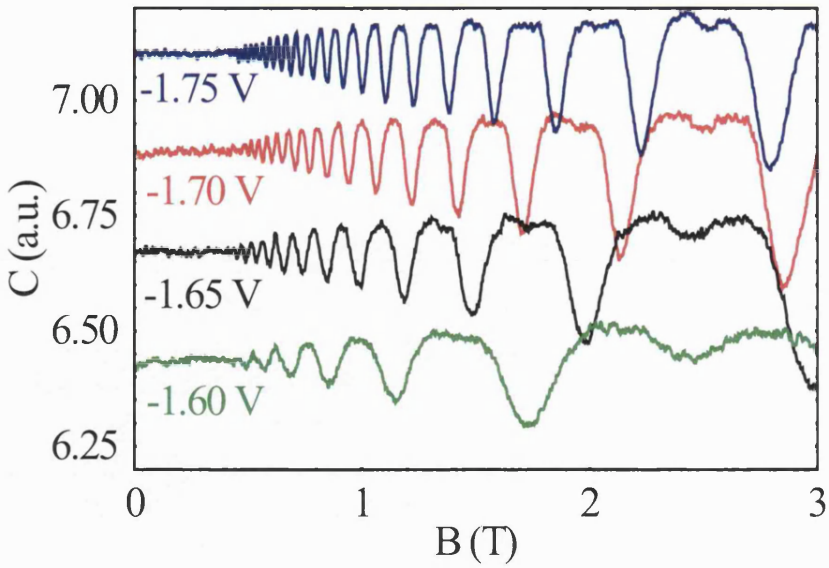

Figure 6.8: Magneto-capacitance of the 15nm barrier sample. Oscillations originate from the 2DES. No oscillations from the 2DHS are observed.

confirmed in an experiment at fixed interlayer bias that uses the frontgate to tune the electron density. Indeed, the period of the capacitance oscillations changes as the electron density is changed by the frontgate. Most likely no oscillations due to the 2D hole system observed, because the Fermi energy of the holes is much lower than that of the electrons (because of their much heavier effective mass) and because the hole mobility is not so high. Unfortunately, the capacitance data thus reveal no additional information on the *coupled* 2D electron-hole system.

6.4 MBE growth and FIB implantation of the second type of 2DES-2DHS samples

Since low AND equal densities of the 2D systems could not be made in the above samples and since it was found out that this is due to the earlier accumulation of a 2D system above the implanted region, another design was made. It was decided to use the FIB during an MBE growth interrupt to implant Beryllium to make the *p*-contacts to the lower 2D system. Since in this design there is no implanted region between the backgate and the 2DHS, full control of the individual densities in both 2D systems should be possible. Although it is known

that Be is a difficult material to incorporate in the GaAs crystal, it was hoped that, by reducing the growth temperature of the first layers after implantation, segregation of the Be atoms with the growth front would not occur. In the following layers, the growth temperature would then be increased to maintain a good quality 2D hole system. Despite several attempts, no samples could be produced with a leakage-free barrier. Typical breakdown voltages were about 0.3-0.4 V; more than a factor of 4 too low. Subsequent secondary ion mass spectrometry revealed that the Be had still significantly segregrated with the growth front, even at the low growth temperatures.

6.5 MBE growth, FIB implantation and testing of the third type of 2DES-2DHS samples

Our final attempt at producing coupled 2D electron-hole samples was by "inverting" the structure. This means that the 2D electron system was the lower 2D carrier system. The FIB was used to write the n-contacts to the lower layer using Si ions. After various implantation dose tests, this turned out to be a success. Also the back gate (now a p-doped layer) could be used to change the density in the 2D electron system.

As a next step, shallow contacts to the upper 2D system (now the 2DHS) needed to be fabricated. This turned out to be problematic, since even very thin Au/Zn/Au contacts penetrated the barrier after annealing. As a consequence, the breakdown voltage of the barrier was very low (about 0.3 V). The trick that worked for shallow n-contacts thus doesn't work for shallow p-contacts. Consequently we searched for p-contacts that do not need annealing. This means that the electrons from these contacts need to overcome the Schottky barrier of the GaAs. By fabricating a top layer with an extremely high p-doping (in excess of 5×10^{19} cm^{-3}), unannealed TiAu contacts can be used (200 Å Ti, 1000 Å Au). To achieve this very high doping level, the carbon cell in the MBE machine is ramped to its maximum heating current and the GaAs growth of the top layer is interrupted for 5 out of 6 seconds while the Carbon shutter remains open. Like this, a sufficiently high p-doping was achieved to fabricate Ohmic so-called "tunnel"-contacts to the upper GaAs layer. This upper layer then contacts the less doped layer below it, which contacts the undoped layer that contacts the

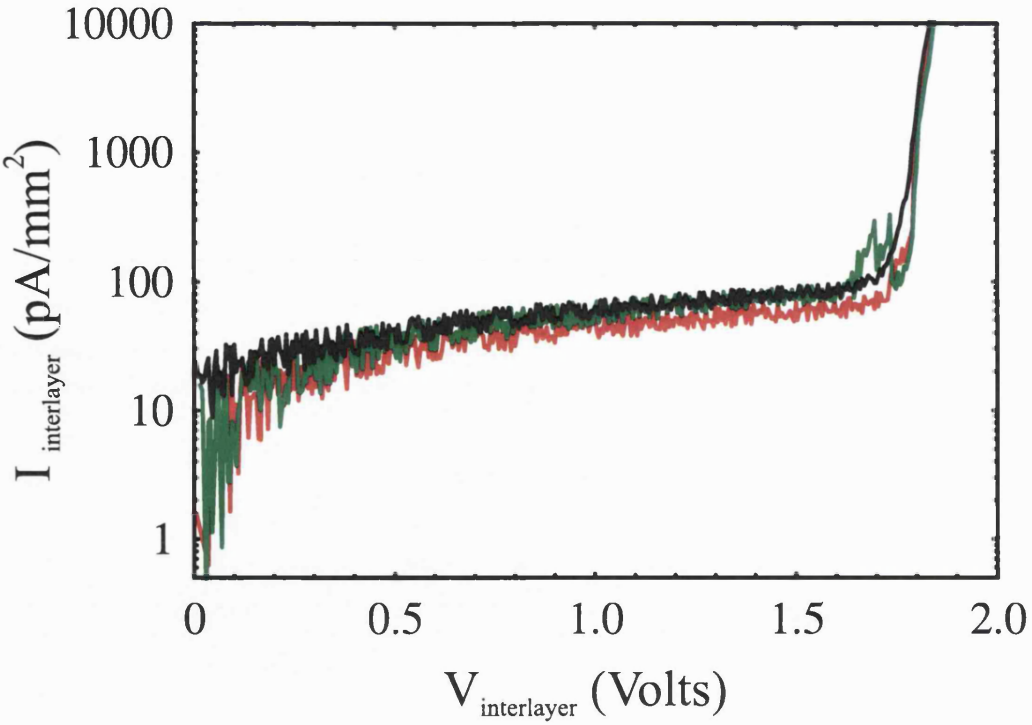

Figure 6.9: Leakage current versus interlayer bias for 3 mesas fabricated from an inverted 15 nm barrier sample.

2DHS.

Figure 6.9 shows that samples produced in this way had sufficently high barrier. Leakage currents at 1.65 V interlayer bias did not exceed 100 pA/mm^2. Moreover, both the contacts to the 2D electron system as well as those to the 2D hole system are Ohmic as is evident from the initial linear increase of the current with source-drain voltage in figure 6.10. Finally, the 2D channels accumulate at nearly the same interlayer bias. Unfortunately, in this test structure no backgate was incorporated. One final structure, that included a backgate, was grown and awaits to be processed and studied.

6.6 Conclusion

A first type of coupled 2D electron-hole system was produced by isolating specific areas in a doped layer by means of FIB implantation during an MBE growth interrupt. This type of sample was tested and studied extensively. It was observed

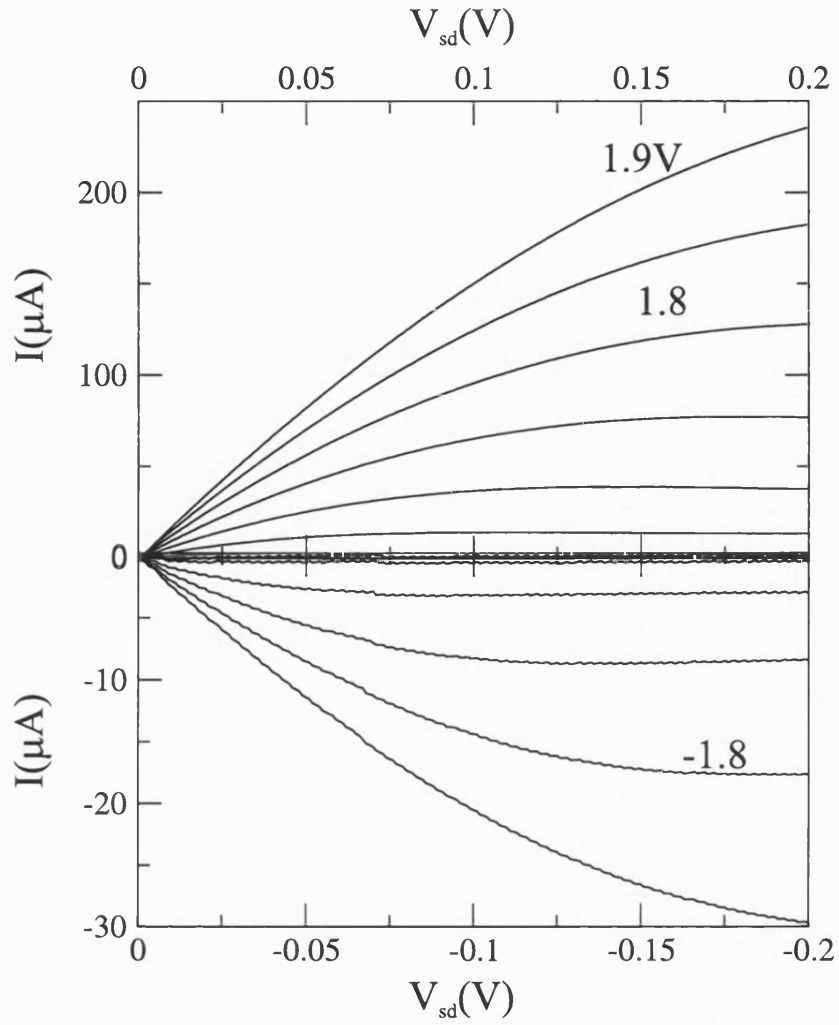

Figure 6.10: Transistor characteristics of an inverted 15 nm barrier sample. Contacts to both the 2DHS and the 2DES are Ohmic, as seen from the initial linear increase of the source-drain current with source drain bias. Holes and electrons accumulate at practically the same interlayer bias in this inverted structure.

that holes accumulate at a lower interlayer bias than the electrons and that the backgate could not be used to produce low AND equal densities. The sample structure was then inverted and the FIB was used to directly write contacts to the lower layer (now the electron layer) during a growth interrupt. Shallow p-contacts that do not need annealing and leave the barrier intact were fabricated. The separate parts of the structure were successfully tested and a sample without backgate revealed Ohmic contacts, good barrier quality and good enhancement mode transistor characteristics. Moreover, electrons and holes accumulate at virtually the same interlayer bias.

Chapter 7

Summary and Conclusions

The aim of the work discussed in this thesis is to study coupled quantum systems using state of the art MBE and FIB samples. Although two very different material systems, in which different types of quantum interactions were studied, the project successfully demonstrates that the high mobility MBE and FIB technology developed here is an invaluable tool for fabricating ultra high quality samples, where a multitude of quantum interactions can be observed.

7.1 AlAs quantum well structures

The AlAs QW structures fabricated demonstrate electron mobilities unsurpassed by those found in the literature and this system is ideal for studying the quantum interactions between quantum states with differing spin quantum numbers. The interesting and complex phenomena observed in tilted field magnetotransport measurements exhibit features which are not explained by an existing theory which considers the influence surface roughness. The data in fact indicate that the surface roughness is not the most important factor for ferromagnetic domain formation. In the measurement configuration where the surface roughness is averaged out and should therefore not be an important factor, we find that the direction of the in-plane field with respect to the current is relevant and the direction of the domains appears to be along the in-plane magnetic field for the ν=6 Landau level crossing but, perpendicular to the in-plane magnetic field for the ν=7 Landau level crossing. The data taken around $\nu = 5$, for a configuration

in which the surface roughness cannot be neglected, is in qualitative agreement with the aforementioned theory.

The domain boundaries are here considered to be the source of the high resistance. Naively, one would have expected that the resistance amplitude changes in steps depending on the number of domains which fit into the sample width. To estimate the possible domain size, we have studied the $\nu = 5$ Landau level crossing with current and in-plane field direction along [110], since in this configuration the resistance anomaly was the strongest. Although a clear width dependence on the amplitude of the resistance spike at the transition was observed between 2 μm and 3 μm, the data for 3 μm to 10 μm are very similar and it is not possible to extract a domain size from these experiments.

Further studies requiring a larger sample set with narrower Hall bar widths and smaller inter voltage probe distances have not been conducted. The use of quantum point contact sample may prove useful in future experiments, since then the relevant width would be a tunable parameter and finite domain size effects could possibly be observed.

It is hoped that, due to the supreme quality of the samples fabricated in this work and the versatility of a system with very large g-factor in tilted magnetic field measurements, further research will be conducted to clarify the precise origin of the magneto-transport anisotropy and to determine the micromagnetic structure of these samples as well as further details of the quantum interaction effects.

7.2 Coupled two dimensional electron-hole systems

The second project in this thesis discusses a very different coupled quantum system. In this study the two quantum states are spatially separated 2D electron and 2D hole systems. The two layers are coupled with each other across a thin superlattice barrier layer sequence by way of the Coulombic interaction. This system is technologically more challenging than that described in the previous section since now two distinct quantum systems separated by a 'leak free" potential require independent contacts. A technique is used, where a bias voltage

on the order of the bandgap, applied between the n and the p-sides of the sample, provides the correct band profile for the accumulation of the two quantum states on either side of the barrier. It is expected that, at low temperatures and low and equal densities, the electrons and holes will form (indirect) excitons, which are predicted to undergo condensation into a superfluid, through a Kosterlitz-Thouless phase transition. Although this interesting state of matter has not been observed, much work has been completed in developing samples which provide optimal conditions for realising it. Three types of samples were fabricated.

In the first type of sample, the FIB is used to isolate certain areas of a p-doped buried layer, in order to fabricate separate contacts to the lower 2D hole system. Shallow n-contacts to the upper 2D system are made by alloying very thin NiAuGe contacts. The samples are characterised by means of transport and capacitance measurements. Both the quality of the 2DHS and that of the 2DES are good, but it was found that low *and* equal densities cannot be achieved with this type of sample, since the 2D hole system accumulates at a lower interlayer bias than the 2D electron system. The fabricated backgate did not function as the field lines end on poorly mobile charges in the implanted region.

For the second type of sample, the FIB is equipped with a custom built Au/Si/Be source and the p-contacts are directly implanted during the MBE growth interrupt. Despite many attempts, the subsequent overgrowth always produced a barrier between the 2D hole and the 2D electron system that was of insufficient quality. Secondary ion mass spectroscopy showed that this is due to segregation of the implanted Be ions with the growth front during the overgrowth, which turns out to be a known and, as yet, unsolved problem.

For the third type of sample, the structure is 'inverted', i.e. the 2DES is now the lower 2D system. The FIB with the custom built source is used to directly implant the n-contacts with Si. This produced a barrier of sufficient quality after overgrowth. Shallow p-contacts that do not diffuse through the barrier turned out to be very difficult to fabricate. Contacts were fabricated to the 2DHS by means of a so-called tunnel-contact of TiAu that was deposited on an extremely heavily p-doped top layer ($>5 \times 10^{19}$ cm^{-3}). This top layer contacts a less heavily doped layer, which contacts the undoped layer that in turn contacts the 2DHG. Various test structures were grown, and every individual step of the fabrication has been checked successfully.

7.3 Future prospects

In part II of this thesis we described the research conducted on AlAs QW structures. Not all the experimental results are in agreement with the theory. A theoretical study of possible orbital effects would be useful and may explain the behaviour of the results reported here. It is hoped that further experiments using AlAs QW structures with quantum point contacts will allow the study of finite domain size effects.

In part III we discussed the fabrication of coupled 2D electron-hole systems. The MBE system used for the growth of these structures is in the process of being replaced by a new system. It is hoped that samples from the new setup will allow the measurement of the interesting physics predicted by theory.

The work described in this thesis confirms that the study of quantum state interactions using advanced molecular beam epitaxy focused ion beam structures reveals new and interesting phenomena previously not measured or predicted by theory.

References

[1] V. Piazza, V. Pellegrini, F. Beltram, W. Wegscheider, T. Jungwirth, and A. H. MacDonald. First-order phase transitions in a quantum Hall ferromagnet. *Nature*, 402:638–641, December 1999.

[2] J. T. Chalker, D. G. Polyakov, F. Evers, A. D. Mirlin, and P. Wölfle. Quantum Hall ferromagnets, cooperative transport anisotropy, and the random field Ising model. *Physical Review Letters*, 66(16):161317, October 2002.

[3] W. Ketterle. *Les Prix Nobel, The Nobel Prizes 2001.* Nobel Foundation, Stockholm, 2002.

[4] K. v. Klitzing. *Nobel Lectures, 1981-1990.* World Scientific Publishing Co., Singapore, 1993.

[5] H. Bachmair, E. O. Göbel, G. Hein, J. Melcher, B. Schumacher, J. Schurr, L. Schweitzer, and P. Warnecke. The von Klitzing resistance standard. *Physica E Low-Dimensional Systems and Nanostructures*, 20:14–23, December 2003.

[6] B. Jeckelmann and B. Jeanneret. The quantum Hall effect as an electrical resistance standard. *Measurement Science and Technology*, 14:1229–1236, August 2003.

[7] A. Hartland. The Quantum Hall Effect and Resistance Standards. *Metrologia*, 29:175–190, January 1992.

[8] R. Haug and D. Weiss. Proceedings of the International Symposium "Quantum Hall Effect: Past, Present and Future" held in Stuttgart, Germany 2-5 July 2003. *Physica E Low-Dimensional Systems and Nanostructures*, 20:D5+, December 2003.

[9] R.B. Laughlin. *Nobel Lectures, Physics 1996-2000.* World Scientific Publishing Co., Singapore, 2002.

[10] U. Zeitler, H. W. Schumacher, A. G. Jansen, and R. J. Haug. Magnetoresistance Anisotropy in Si /SiGe in Tilted Magnetic Fields: Experimental Evidence for a Stripe-Phase Formation. *Physical Review Letters*, 86:866–869, January 2001.

[11] W. Pan, H. L. Stormer, D. C. Tsui, L. N. Pfeiffer, K. W. Baldwin, and K. W. West. Highly anisotropic transport in the integer quantum Hall effect. *Physical Review B*, 64(12):121305, September 2001.

[12] K. Vakili, Y. P. Shkolnikov, E. Tutuc, E. P. Poortere, and M. Shayegan. Realization of an Interacting Two-Valley AlAs Bilayer System. *Physical Review Letters*, 92(18):186404, May 2004.

[13] David Millar, Ian Millar, John Millar, and Margaret Millar. *The Cambridge Dictionary of Scientists.* Cambridge University Press, 2002.

[14] David Pines and J.Robert Schrieffer. *Theory of Superconductivity (Advanced Books Classics S.).* Perseus Books, 1999.

[15] B. P. Zakharchenya and V. Y. Frenkel. History of the theoretical prediction and experimental discovery of the exciton. *Physics of the Solid State*, 36:469–474, March 1994.

[16] X. Xia, X. M. Chen, and J. J. Quinn. Magnetoexcitons in a GaSb-AlSb-InAs quantum-well structure. *Physical Review B*, 46:7212–7215, September 1992.

[17] L. V. Butov, A. C. Gossard, and D. S. Chemla. Macroscopically ordered state in an exciton system. *Nature*, 418:751–754, August 2002.

[18] L. V. Butov. Topical Review: Condensation and pattern formation in cold exciton gases in coupled quantum wells. *Journal of the Physics of Condensed Matter*, 16:1577, December 2004.

[19] L. Butov. Exciton Condensation in Semiconductor Coupled Quantum Wells. *APS Meeting Abstracts*, page H7001, March 2003.

[20] S. de-Leon and B. Laikhtman. Exciton wave function, binding energy, and lifetime in InAs/GaSb coupled quantum wells. *Physical Review B*, 61:2874–2887, January 2000.

[21] L. V. Butov and A. I. Filin. Anomalous transport and luminescence of indirect excitons in AlAs/GaAs coupled quantum wells as evidence for exciton condensation. *Physical Review B*, 58:1980–2000, July 1998.

[22] James Clerk Maxwell. *Treatise on Electricity and Magnetism, Vol. 1.* Dover Publications, 1954.

[23] E.H. Hall. On a new action of the magnet on electric currents. *American Journal of Mathematics*, 2:287–292, 1879.

[24] P.Drude. Zur elektronentheorie iii. *Annalen der Physik 7*, page 687692, 1902.

[25] K. V. Klitzing, G. Dorda, and M. Pepper. New Method for High-Accuracy Determination of the Fine-Structure Constant Based on Quantized Hall Resistance. *Physical Review Letters*, 45:494–497, August 1980.

[26] Laughlin R.B. Fractional quantization of the hall effect. *Presented at the 3rd Intern. Winterschool on New Develop. in Solid State Phys., Salzburg, 26 Feb. - 2 Mar*, feb 1984.

[27] C. W. J. Beenakker. Edge channels for the fractional quantum Hall effect. *Physical Review Letters*, 64:216–219, January 1990.

[28] A.M. Chang. A unified transport theory for the integral and fractional quantum hall effects. *Solid State Communication*, 74:216, jan 1990.

[29] D. B. Chklovskii, B. I. Shklovskii, and L. I. Glazman. Electrostatics of edge channels. *Physical Review B*, 46:4026–4034, August 1992.

[30] D. B. Chklovskii, K. A. Matveev, and B. I. Shklovskii. Ballistic conductance of interacting electrons in the quantum Hall regime. *Physical Review B*, pages 12605–12617, May 1993.

[31] D. B. Chklovskii and P. A. Lee. Transport properties between quantum Hall plateaus. *Physical Review B*, 48:18060–18078, December 1993.

[32] J. Weis, J. Wei, and K. V. Klitzing. Single-electron transistor probes two-dimensional electron system in high magnetic field. *Physica E Low-Dimentional Systems and Nanostructures*, 3:23–29, 1998.

[33] E. Ahlswede, J. Weis, K. v. Klitzing, and K. Eberl. Hall potential distribution in the quantum Hall regime in the vicinity of a potential probe contact. *Physica E Low-Dimensional Systems and Nanostructures*, 12:165–168, January 2002.

[34] E. Ahlswede, P. Weitz, J. Weis, K. von Klitzing, and K. Eberl. Hall potential profiles in the quantum Hall regime measured by a scanning force microscope. *Physica B Condensed Matter*, 298:562–566, April 2001.

[35] P. Weitz, E. Ahlswede, J. Weis, K. V. Klitzing, and K. Eberl. Hall-potential investigations under quantum Hall conditions using scanning force microscopy. *Physica E Low-Dimensional Systems and Nanostructures*, 6:247–250, February 2000.

[36] B. A. Joyce. Molecular beam epitaxy. *Physics Education*, 16:328–332, November 1981.

[37] A.Zangwill. *Physics at Surfaces.* Cambridge University Press, Cambridge, 1988.

[38] L. Royer. Recherches experimentales sur l'epitaxie ou orientation mutuelle de cristaux d'espes differentes. *Bulletin de la Societe Française Mineralogie et de Cristallographie*, 51:7, 1928.

[39] Y. Ishikawa et al. MBE growth of GaAs and III-V alloys. *Journal of Vacuum Science and Technology A*, 9(2):250, 1991.

[40] Ming-Zhu Huang and W. T. Ching. A minimal basis semi-ab initio approach to the band structures of semiconductors. *Journal of Physics and Chemistry of Solids*, 46:977, 1985.

[41] K. Maezawa and T. Mizutani. Effective mass and ground state of alas quantum wells studied by magnetoresistance measurements. *Journal of Applied Physics*, 71:296, 1992.

[42] M. Schulte, J. G. Lok, G. Denninger, and W. Dietsche. Electron Spin Resonance on a Two-Dimensional Electron Gas in a Single AlAs Quantum Well. *Physical Review Letters*, 94(13):137601, April 2005.

[43] S. Adachi. GaAs, AlAs, and Al(x)Ga(1-x)As - Material parameters for use in research and device applications. *Journal of Applied Physics*, 58:1, August 1985.

[44] E. P. de Poortere, Y. P. Shkolnikov, E. Tutuc, S. J. Papadakis, M. Shayegan, E. Palm, and T. Murphy. Enhanced electron mobility and high order fractional quantum Hall states in AlAs quantum wells. *Applied Physics Letters*, 80:1583–1585, March 2002.

[45] S. Yamada, K. Maezawa, W. T. Yuen, and R. A. Stradling. X conduction two-dimensional subband structure and order in AlGaAs/AlAs quantum wells. *Physica B Condensed Matter*, 201:295–300, July 1994.

[46] A. K. Saxena. The conduction band structure and deep levels in $Ga_{1-x}Al_xAs$ alloys from a high-pressure experiment . *Journal of Physics C Solid State Physics*, 13:4323–4334, August 1980.

[47] Y. P. Shkolnikov, E. P. de Poortere, E. Tutuc, and M. Shayegan. Valley Splitting of AlAs Two-Dimensional Electrons in a Perpendicular Magnetic Field. *Physical Review Letters*, 89(22):226805, November 2002.

[48] E. Kisker. *Metallic Magnetism.* Springer-Verlag, Berlin, 1987.

[49] T. Jungwirth and A. H. MacDonald. Pseudospin anisotropy classification of quantum Hall ferromagnets. *Physical Review B*, 63(3):035305, January 2001.

[50] P. M. Chaikin and T. C. Lubensky. *Principles of Condensed Matter Physics.* Cambridge University Press, Cambridge, 1995.

[51] E. P. de Poortere, E. Tutuc, R. Pillarisetty, S. Melinte, and M. Shayegan. Magnetism and pseudo-magnetism in quantum Hall systems. *Physica E Low-Dimensional Systems and Nanostructures*, 20:123–132, December 2003.

[52] L. Brey and C. Tejedor. Spins, charges, and currents at domain walls in a quantum Hall Ising ferromagnet. *Physical Review B*, 66(4):041308, July 2002.

[53] J.M. Kosterlitz and D.J. Thouless. Ordering, metastability and phase transitions in two-dimensional systems. *Journal of Physics C: Solid State Physics*, 6:1181, 1973.

[54] K. Zalewski. A very brief review of Bose-Einstein correlations. *Nuclear Physics B Proceedings Supplements*, 96:23–30, April 2001.

[55] A. Griffin, D. W. Snoke, and S. Stringari. Bose-einstein condensation. *Review articles originating from an international workshop held in Levico Terme, Italy, 31 May - 4 June, 1993*, 1995.

[56] J.B. Ketterson and S.N. Song. *Superconductivity.* Cambridge University Press, Cambridge, 1999.

[57] L. V. Butov, A. Zrenner, G. Abstreiter, G. Böhm, and G. Weimann. Condensation of indirect excitons in coupled AlAs/GaAs quantum wells. *Physical Review Letters*, 73(2):304–307, July 1994.

[58] T. Fukuzawa, E. E. Mendez, and J. M. Hong. Phase transition of an exciton system in GaAs coupled quantum wells. *Physical Review Letters*, 64(25):3066–3069, June 1990.

Appendix

Electron-hole device fabrication: Photolithography and sample processing

After the MBE growth, FIB implantation and overgrowth, the samples are cleaved into 3.5 mm by 4 mm pieces using a diamond scribe and then cleaned to remove any small particles resulting from the cleaving as follows:

- Acetone flush
- 2 mins in acetone ultrasound bath
- Acetone flush
- 30s acetone bath
- 15s acetone bath
- 5s Acetone bath
- 20s Isopropanol dip
- Blow dry with N_2

The samples are placed on a photo resist spinner and S1805 photo resist is applied with a syringe. The samples are spin coated at 4500 rpm for 30 s and then baked for 2 minutes on a 90 °C hotplate or for 20 minutes in furnace at 85 °C; this produces a layer $\approx$ 300–400 nm thick. The first lithography step is difficult since the alignment marks are only visible when illuminated under a 45° angle so the alignment instrument is adapted to include a filtered cold light source lamp. The

samples are aligned to a chromium/quartz mask, exposed for 30–60 s and then developed in a solution of one part AZ351B developer and four parts H_2O for 30–60 s. The first etch process is performed to allow contacts to the *p*-layer, the etch depth is 750 nm using a etching solution 1 ml H_2SO_4, 8 ml H_2O_2, 160 ml H_2O (about 220 nm/minute).

The second lithography step is performed to produce the back gate contacts. The photo resist layer is applied and baked as before. Following a 22 s illumination the sample is put in chlorobenzene for 3 minutes and then dried in an oven at 85 °C for 10 minutes; this causes the photo resist to have an undercut profile. The sample is developed as before and then etched through to the backgate layer ($\approx$ 1100 nm deep). The standard *n*-type (1054 Å Au, 584 Å Ge, 400 Å Ni) contacts to the backgate are produced in a vacuum chamber by evaporating the metals in electrically heated crucibles. The deposition rate is measured by a oscillating quartz crystal whose resonant frequency changes when material is deposited on its surface; this rate is then controlled by varying the current through the crucible. After evaporation the photoresist is removed in acetone. This lift-off process is possible due to the undercut photoresist profile. Annealing at 440 °C for 30 s in forming gas at 300 mbar diffuses and activates the contact material.

The lithography for the *p*-type contacts is similar to that for the *n*-type contacts. Prior to the evaporation the samples are cleaned in O_2 plasma for 30 seconds, 2 minutes in semicoclean and 5 s in 30 % HCl. 50 Å Au, 280 Å Zn and 250 Å Au are evaporated thermally in the *p*-contact evaporator followed by the liftoff process. The annealing conditions for these contacts are in 300 mbar forming gas with a heating ramp of 8.3 °C/s to 250 °C, a wait of 30 s and 8.3 °C/s to 420 °C, and finally a wait of 30 s before rapid cooling.

Very shallow *n*-type contacts to the 2DEG are required since the contact material should not penetrate the barrier layer. This is achieved by reducing the amount of material evaporated to 20 Å Au, 10Å Ge and 8Å Ni and annealing at only 340°C for 30 s in forming-gas at 300 mbar.

The frontgate is produced by firstly etching the most heavily doped GaAs layers away to separate the *n*-contacts from each other. 100Å Ti, 1000Å Au is evaporated under rotation and a tilt angle of about 20°; this minimises the lateral distance between the gate and the *n*-contacts.

The final step of processing the samples is to etch the mesa. Reactive ion etching (RIE) is used because it ensures that a straight etch profile is produced and that the metal from the frontgate doesn't short circuit the barrier. Since the Schottky barrier between the TiAu frontgate and the GaAs is ≈ 0.7 V it is not high enough to isolate the interlayer voltage of ≈ 1.6 V. The samples are mounted in and bonded to chip carriers before testing.

Publications

Closely spaced and separately contacted two-dimensional electron and hole gases by *in situ* focused-ion implantation

M. Pohlt, M. Lynass,[a] J. G. S. Lok,[b] W. Dietsche,[c] K. v. Klitzing, and K. Eberl
Max-Planck Institut für Festkörperforschung, Heisenbergstrasse 1, 70569 Stuttgart, Germany

R. Mühle
Swiss Federal Institute of Technology, Zürich, ETH Zentrum, 8092 Zürich, Switzerland

(Received 6 April 2001; accepted for publication 24 January 2002)

Separately contacted layers of a two-dimensional (2D) electron gas and a 2D hole gas have been prepared in GaAs, which are separated by AlGaAs barriers down to 15 nm thickness. The molecular-beam-epitaxial growth was interrupted just before growth of the double-layer structure in order to use *in situ* focused-ion-beam implantation to pattern contacts which extend underneath the barrier. The two charge gases form upon biasing the *p*- and *n*-type contacts underneath and above the barrier in the forward direction and show independent transistor-like behavior. © *2002 American Institute of Physics.* [DOI: 10.1063/1.1463698]

There has been great interest over the last years in fabricating closely spaced two-dimensional (2D) electron and 2D hole systems. If the distance between the oppositely charged layers can be decreased to about 10–20 nm, then one should be able to observe phenomena like bound states of spatially separated electrons and holes. A gas of such indirect excitons could even condense into a superfluid as was proposed by several authors.[1]

The crucial point in preparing such systems is the small distance between the two charge layers which makes their preparation virtually impossible if one relies solely on doping of conventional semiconductors because of the high built-in electric field. Several routes have been followed to circumvent this problem. One possibility is the use of the InAs–GaSb heterostructures which have a large band offset leading to equilibrium 2D electron (2DEG) and 2D hole gases (2DHG) in close proximity.[2] However, many proposed experiments require separate contacts to the two layers, which are very difficult to produce in this system. Furthermore, the mean-free paths of the holes and electrons are usually relatively short and the carrier concentrations are frequently too high to form a low-density exciton gas, which is a prerequisite of the searched superfluidity effects. Another rather successful route to closely spaced layers is the optical excitation of carriers in double quantum wells. The application of an electric field separates the electrons and holes. Interaction effects between the two are usually studied using the luminescence, and indications of Bose–Einstein condensation have indeed been observed.[3] However, the lack of electrical contacts to the optically excited charges make transport measurements impossible. Furthermore, only systems where the recombination lifetime is sufficiently short to cause sufficient luminescence can be studied this way.

An alternative is the use of nonequilibrium methods, which means that a voltage is applied between the two layers compensating the band bending between the positive and negative charges. These techniques rely obviously on separate contacts to the two layers, because the charge gases themselves form only after an electric field has been applied. The contacts should thus overlap with the barrier region or should at least be perfectly aligned. Two nonequilibrium designs have been published.[4,5] The most difficult part are the contacts to the bottom charge layer, which was either done by implantation using the gate as a self-aligned mask or by evaporation from the side of the structure and subsequent diffusion.

Here, we present another very reliable technology for preparing spatially separated 2DEG and 2DHG systems at barrier thicknesses down to 15 nm. A growth interruption in the molecular-beam-expitaxy (MBE) process is used to transfer the sample into a focused-ion-beam (FIB) system, where the contacts to the lower charge gas are implanted prior to the growth of the double layer structure. Our device structure is shown schematically in Fig. 1(a). The 2DEG and the 2DHG form on top and below the AlGaAs barrier (marked in black) by the application of a voltage between the electron contacts on the top of the structure and the hole contacts below the barrier. The extension of the *p*-doped contact region under the barrier is the crucial point of this design and is achieved by the FIB implantation.[6] An *n*-type gate at the very bottom of the structure and a metallic front gate allow the adjustment of the two carrier concentrations.

The following growth and implantation sequence turned out to be successful. A 500 nm GaAs bufferlayer is grown on top of a semi-insulating substrate. Next, a 100 nm Si-doped (2×10^{18} cm^{-3}) GaAs layer is grown as the back gate, followed by 300 nm undoped GaAs and 100 nm C-doped (2×10^{18} cm^{-3}) GaAs for *p*-contacts. After UHV-transfer to the FIB chamber, parts of this layer are isolated by Si^+ implantation (10^{12} cm^{-2} at 30 keV). Then, 300 nm GaAs with C doping gradually decreasing from 10^{17} to 5×10^{16} cm^{-3} is grown, followed by 40 nm undoped GaAs. Next, a 15 nm $Al_{0.8}Ga_{0.2}As$ barrier is grown followed by 50 nm undoped GaAs and a 300 nm GaAs layer with Si doping gradually increasing from 10^{16} to 10^{17} cm^{-3}. The structure is finished by growing 200 nm Si-doped (2×10^{18} cm^{-3}) GaAs.

[a]Also at: University of Bath, Bath, U.K.
[b]Electronic mail: lok@fkf.mpg.de
[c]Electronic mail: dietsche@fkf.mpg.de

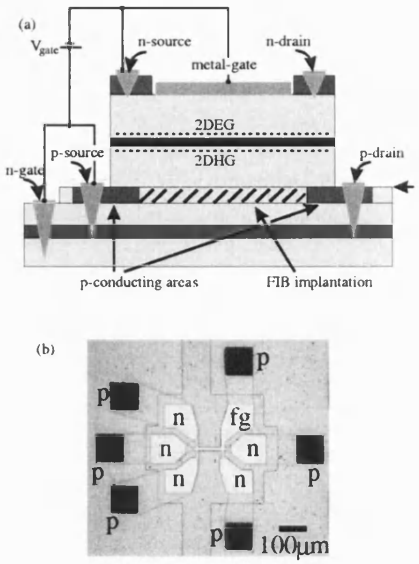

FIG. 1. (a) Sample structure. 2DEG and the 2DHG form on the upper and the lower side of the AlGaAs barrier (black) after a voltage V_{gate} has been applied between the p and n contacts. The p contacts are structured by Si implantation (hatched area) using a FIB system in a MBE growth interruption. The arrow marks the layer of the growth interruption. (b) Photograph of a device allowing separate transport measurements of the 2DEG and the 2DHG. "p" and "n" mark the p- and n-type contacts. "fg" connects to the front gate. The area structure extending from the top to the bottom of the picture has been etched down through the p-type contact layer. The contact to the back gate is not visible in this picture.

Strong efforts had to be made to avoid contamination during the transfer process to and from the FIB chamber. The pressure in the transfer tunnel is typically 10^{-9} mbar, which causes contamination with carbon and oxygen as revealed by secondary ion mass spectroscopy (SIMS). The oxygen can be removed after return to the MBE by a heat treatment at 630 °C for 15 min. The carbon, however, could only be removed by depositing an As_2 layer *before* the transfer to the FIB. This was done using a GaAs cracker cell at 830 °C for 30 s with the substrate at room temperature. After return to the growth chamber, the As_2 cap disappears together with the contaminants at temperatures above 350 °C. Using this procedure, SIMS data did not show residual carbon contamination.

The Si ions easily penetrate the As_2 layer and overcompensate the C doping of the p-contact layer. Alternatively, one could have used a p-type implantation, e.g., Be ions to form the p-type contacts. This was tested but was not successful due to the Be segregation during the GaAs overgrowth leading to leakage through the barrier. For alignment of the implanted regions with the subsequent photolithography, we implant Au marks with high doses that are easily visible after overgrowth.

After completion of the MBE growth, the samples are annealed at 800 °C for 5 s in order to activate the implanted Si donors. Then, the devices are prepared conventionally. First, the p-type contacts are made with alloyed Au(5 nm)/Zn(30 nm)/Au(25 nm) after removing most of the material atop the p-contact regions. Then, the shallow n-type contacts are made, alloying very thin Au/Ge/Ni layers of only 3 nm total thickness annealed at 320 °C for 30 s. This way, the n-type contacts at the top do not diffuse into the barrier. Fabrication of the front gate is performed in two steps with one lithography: first, the most heavily doped GaAs layers (which are conducting at low temperature) are etched away, separating the n contacts from each other. Then, a Ti/Au metallization is evaporated with the same mask under rotation and a tilt angle of about 20°, which minimizes the lateral distance between the gate and the n-contacts. In a last step the mesa is defined with reactive ion etching. This prevents any metallization from the contacts or the front gate to make an unintentional contact with the region under the barrier and is crucial because the Schottky barriers are no sufficient isolation to the relatively high voltage between 2DEG and 2DHG. A photograph of the completed structure is shown in Fig. 1(b).

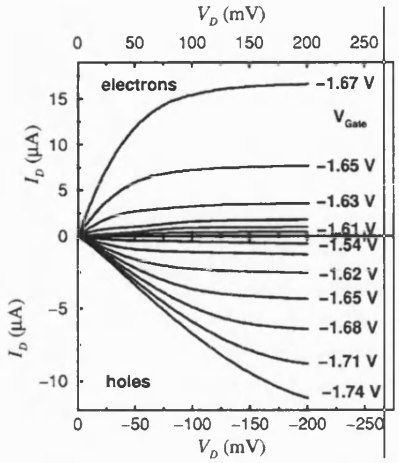

FIG. 2. Transistor-like characteristics of 2DEG and the 2DHG forming at the two sides of an AlGaAs barrier with 15 nm thickness.

The samples obtained this way contain two channels which are populated by applying a voltage between the front- and the back-gate with the source contacts of both channels connected to the respective gate. The output characteristics of the p and n channels are shown in Fig. 2 and are measured with the p-source contact on ground, the n-source contact on V_{gate}, and the drain contacts on potential V_D with respect to the potential on the source contact. During the $I(V)$ measurements in the p channel, the drain in the n channel is on V_{gate}, and during measurements in the n channel the drain in the p channel is on ground. The barrier of the sample is 15.3 nm $Al_{0.8}Ga_{0.2}As$. The transport data compare rather favorably with earlier efforts to obtain coupled electron and hole gases using *in situ* FIB implantation.[7] The contacts to both channels are completely Ohmic, as is visible in Fig. 2 from the initially linear increase of the currents with the source–drain voltage. No conductivity is measurable at voltages below the respective threshold voltage, indicating that there are no parallel conductance channels.

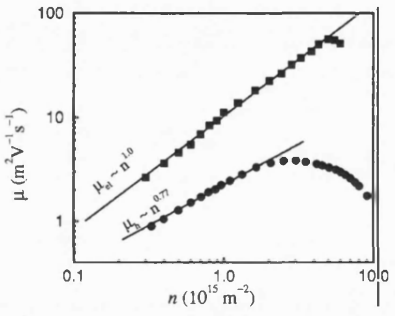

FIG. 3. Mobility of 2DHG and 2DEG vs density at 4.2 K.

Each of the two charge gases behaves like an enhancement-mode transistor, with a threshold voltage of -1.60 V for the n channel and -1.52 V for the p channel. The slightly different thresholds originate probably from different charging of the two gates and the respective doped regions between them and the actual active layers, because in structures where the most heavily doped region between the n contacts is not etched away, the electrons and holes accumulate simultaneously. The interlayer leakage current for the 15 nm barrier samples is about 300 pA/mm^2 at 1.6 V. This corresponds to a tunneling lifetime of 0.4 s, which is many orders of magnitude longer than observed with 2DEG/2DHG systems generated by optical excitation. Magnetotransport measurements of the two charge gases (not shown) exhibit the typical Shubnikov de Haas oscillations in the longitudinal resistance, proving their two-dimensional nature.

Figure 3 plots mobility versus density of the 2D gases at 4.2 K. The densities are varied by connecting the gates to their respective source contacts and changing the bias on the front gate and the electron source contact. Below 2×10^{15} m^{-2}, the hole mobility is proportional to $n^{0.77}$ and it displays a maximum around 3×10^{15} m^{-2}. Such power-law behavior is commonly observed and values of the exponent below 1 indicate a good quality 2D gas.[8] The electron mobility follows also a power-law behavior. However, its exponent is higher (~1), most likely because the electron gas forms at the inverted interface. The absolute values of both the electron and hole mobility in our structures are about 50%–70% of those obtained in standard heterostructures grown in the same MBE machine.

We further note that the hole mobility decreases slightly (2%–3%) when the electrons accumulate. At a first glance this seems counterintuitive, since the electrons can screen the random potential fluctuation the holes scatter on. However, upon electron accumulation, the potential profile in the growth direction changes, because the holes are no longer induced by the front gate, but by the 2DEG itself (which is much closer), and correspondingly, the holes move a bit closer to the interface. This probably accounts for the slight decrease in the hole mobility.

In conclusion, we have prepared spatially separated 2D electron and 2D hole gases with distances down to 15 nm using FIB implantation during MBE growth interruption. Carrier concentrations in the two layers can be varied from 10^{14} up to nearly 10^{16} m^{-2}. Both transport and capacitance measurements are possible with these devices and will be used to study the interaction effects between the layers.

The authors thank U. Sivan and K. Muraki for helpful discussions and W. Wegscheider for the growth of several wafers in the course of this work. The contributions of H. Rubel and C. Jörger at the early stages of the project are gratefully acknowledged. This research is supported by the BMBF and TMR No. ERBFMRX-CT98-0180.

[1] P. B. Littlewood and X. Zhu, Phys. Scr., T **68**, 56 (1996).
[2] E. E. Mendez, L. Esaki, and L. L. Chang, Phys. Rev. Lett. **55**, 2216 (1985).
[3] T. Fukuzawa, E. E. Mendez, and J. M. Hong, Phys. Rev. Lett. **64**, 3066 (1990); J. A. Kash, M. Zachau, E. E. Mendez, J. M. Hong, and T. Fukuzawa, *ibid.* **66**, 2247 (1991); L. V. Butov, A. Zrenner, G. Abstreiter, G. Bhm, and G Weimann, *ibid.* **73**, 304 (1994).
[4] U. Sivan, P. M. Solomon, and H. Shtrikman, Phys. Rev. Lett. **68**, 1196 (1992).
[5] B. E. Kane, J. P. Eisenstein, W. Wegscheider, L. N. Pfeiffer, and K. W. West, Appl. Phys. Lett. **65**, 3266 (1996).
[6] Orsay Physics FIB column with integrated optical microscope.
[7] S. Vijendran, P. J. A. Sazio, H. E. Beere, G. A. C. Jones, D. A. Ritchie, and C. E Norman, J. Vac. Sci. Technol. B **17**, 3226 (1999).
[8] M. Shayegan, V. J. Goldman, C. Jiang, T. Sajoto, and M. Santos, Appl. Phys. Lett. **52**, 1086 (1988); L. Pfeiffer, K. W. West, H. L. Störmer, and K. W. Baldwin, *ibid.* **55**, 1888 (1989); B. E. Kane, L. N. Pfeiffer, K. W. West, and C. K. Harnett, *ibid.* **63**, 2132 (1993).

Available online at www.sciencedirect.com
SCIENCE DIRECT
ELSEVIER
Physica E 22 (2004) 94–97
PHYSICA E
www.elsevier.com/locate/physe

Quantum Hall ferromagnetism of AlAs 2D electrons

J.G.S. Lok*, M. Lynass, W. Dietsche, K. von Klitzing, M. Hauser

Max-Planck Insitut für Festkörperforschung, Heisenbergstrasse 1, Stuttgart 70569, Germany

Abstract

We present magneto-transport measurements in tilted magnetic fields on high mobility ($\mu = 300.000\ \mathrm{cm}^2/\mathrm{V\,s}$) AlAs two-dimensional electron systems. Our samples show integer and fractional quantum Hall effects. In titled magnetic fields, at the crossings of Landau levels with opposite spin, the resistance shows a spike if the crossing occurs near integer filling or is significantly enhanced otherwise. The position of the spike displays a hysteresis below 350 mK that reaches more than 0.1 T at 20 mK. From the position of the crossing in the ($B_{\mathrm{tot}}, B_{\mathrm{perp}}$)-plane the difference in exchange energy of the crossing levels is determined and found to be a non-linear function of the perpendicular magnetic field.

PACS: 73.63.Hs; 75.47.−m; 75.60.Ch

Keywords: AlAs 2DES; Quantum Hall effects; Quantum Hall ferromagnetism

Recently there has been renewed interest in the physics occurring when two Landau levels with opposite spin in a semiconductor become degenerate. The two-dimensional electron system (2DES) in a semiconductor offers full control of the density of the carriers (and thus also of the spins) and, at the Landau level crossing, it serves as a model system for studying magnetism in two dimensions. If the exchange interaction between carriers in the same Landau level is larger than that of carriers in different Landau levels, the system shows Ising anisotropy and many of the physical properties are hysteretic. Because of the analogy with ferromagnetic metals, the subject has been labelled quantum Hall ferromagnetism.

Crossings of Landau levels with opposite spin have been realised in a variety of different material systems, including wide GaAs quantum wells (QWs) [1,2], bilayer GaAs QW [3], AlAs 2DESs [4], SiGe QW [5] magnetic semiconductors [6] and in GaAs 2DESs in the fractional quantum Hall regime [7–11]. In a typical experiment the perpendicular magnetic field is kept constant (i.e. the filling factor (ν) is fixed) and an in-plane magnetic field is added. The in-plane field only influences the spin energy and not the cyclotron energy, and it is changed such that levels with opposite spin become degenerate. Among the above systems the AlAs 2DES is particularly suited because the large effective cyclotron mass (0.51–0.46m_e [12,13]) and the large g-factor (+1.9 [14]) allow crossings to be obtained at moderate tilt angles of the sample in the magnetic field, thus minimising the influence of the parallel field component on the orbital motion.

Our wafers are grown on (1 0 0) substrates, volume doped with Si on both sides of a 15 nm AlAs QW which is flanked by $Al_{0.45}Ga_{0.55}As$ barriers. The electrons in the AlAs are confined to the X-valleys. In

* Corresponding author. Fax: +49-711-689-1010.
E-mail address: lok@fkf.mpg.de (J.G.S. Lok).

1386-9477/$ - see front matter © 2003 Elsevier B.V. All rights reserved.
doi:10.1016/j.physe.2003.11.224

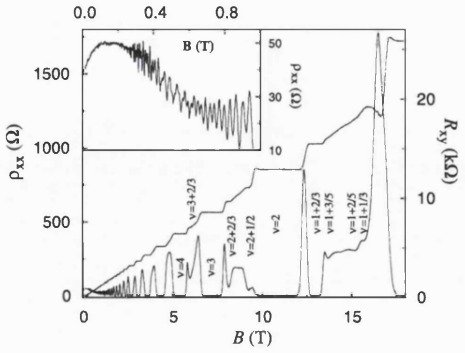

Fig. 1. Longitudinal and Hall resistance vs. magnetic field at $T = 20$ mK. Inset shows the positive magneto-resistance and the low field Shubnikov–de Haas oscillations.

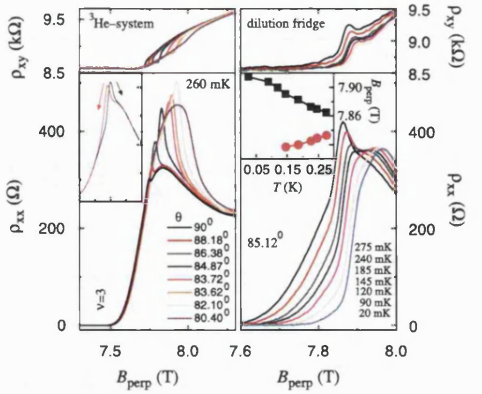

Fig. 2. Left: Hall resistance (top) and longitudinal resistance (bottom) vs. perpendicular magnetic field (B-sweep up) around $\nu = 3$ at 260 mK for various angles between magnetic field and plane of the 2DES. At the crossing of the Landau levels a spike develops in the resistance. Inset shows the hysteresis between B-sweep up and B-sweep down ($\theta = 84.87°$). Right: temperature dependence of R_{xy} (top) and the spike in ρ_{xx} (bottom) with the B-field being swept up, showing a clear shift to higher B_{perp} for lower T. Inset: hysteresis of the phase transition.

these QWs only the in-plane valleys are occupied. The quality of our AlAs 2DESs is evidenced by their high mobility: at 0.25 K and a carrier density (n) of 4.5×10^{15} m^{-2} we obtain a mobility (μ) of 310.000 cm^2/V s, which compares favourably with the best results found in literature [15]. Our samples are 80 μm wide Hall bars, aligned along the [1 1 0] axis and contacted with AuGeNi alloyed contacts. Samples are mounted on an rotator that allows in situ rotation. They are either immersed in the mixture of a dilution refrigerator or mounted at the cold finger of a ^{3}He-system. In the former set-up the current direction is under a 45° angle with the in-plane field component, in the latter the current direction is perpendicular to it. Magneto-transport measurements were taken with a 1–10 nA AC current at 18.54 Hz.

Fig. 1 plots longitudinal and Hall resistance vs. magnetic field oriented perpendicular to the 2DES of one of our samples at 20 mK ($n = 5.3 \times 10^{15}$ m^{-2}; $\mu = 290.000$ cm^2/V s). In high magnetic fields (> 2 T), the integer quantum Hall effect is fully developed, i.e. the Hall resistance displays quantised plateaus and the longitudinal resistance becomes zero. Additionally at certain fractional fillings ($\frac{11}{3}$, $\frac{8}{3}$, $\frac{7}{3}$, $\frac{5}{3}$, $\frac{8}{5}$, $\frac{7}{5}$ and $\frac{4}{3}$), the fractional quantum Hall effect develops. In low magnetic fields (inset Fig. 1) the longitudinal resistance first shows positive magneto-resistance. From 0.2 T onwards Shubnikov–de Haas oscillations start and a clear beating is seen that originates from the interference of Landau levels from the two occupied valleys. Scattering of electrons between these two valleys could be responsible for the positive magneto-resistance (see Ref. [16] and references therein). Alternatively weak anti-localisation could play a role.

Magneto-resistance traces were taken for many different angles (θ) between the magnetic field and the plane of the 2DES. Fig. 2 plots few of such traces near $\nu = 3$ vs. perpendicular magnetic field. At $\theta = 90°$ a small kink in the flank of ρ_{xx} on the high magnetic field side of the $\nu = 3$ minimum appears. Simultaneously the Hall resistance shows a step-like structure. By slightly tilting the sample in the magnetic field, the kink in ρ_{xx} develops into a spike and slowly shifts to higher perpendicular magnetic fields upon decreasing θ. Finally around $\theta = 80.4°$, the spike turns into a broad maximum, whose amplitude is still significantly enhanced compared to the maximum at $\theta = 90°$. The spike in ρ_{xx} marks the magnetic field at which a level crossing occurs. The *position* of the spike in ρ_{xx} is slightly hysteretic. The inset shows that it appears in higher magnetic fields when the field is swept up than when it is swept down. Also, the amplitude of the spike

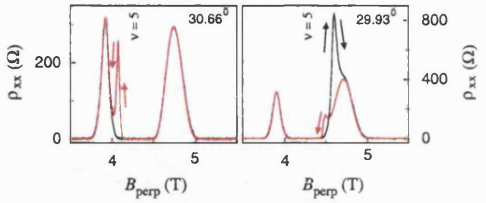

Fig. 3. Longitudinal resistance for up and down sweeps around $\nu = 5$ for two angles.

depends on sweep direction. For the data shown in Fig. 2 it is lower on the sweep down. However, contrary to [4] for crossings that occur on the low magnetic field side of integer filling factor (Fig. 3), the amplitude is larger for the sweep down. In fact, for several of the crossings near $\sin(\theta) = 0.5$ up sweeps may not show any spike at all, while the down sweeps show a spike that is nearly as high as the resistance at the centre of the bordering Landau level (Fig. 3). The inset in the right part of Fig. 2 plots the temperature dependence of the hysteresis, which reaches more than 0.1 T at 20 mK. Below 150 mK, for the B-sweep down, the spike disappears into the $\nu=3$ minimum and cannot be traced anymore. Fig. 2 right panel bottom, plots $\rho_{xx}(\theta = 85.12°)$ vs. B_{perp} for B-sweeps to higher magnetic fields for various temperatures. A clear shift of the spike to higher B_{perp} for lower T is observed. In this set-up the Hall resistance (top) also displays a spike. Whether this results from the different orientation of the rotation axis or from the different cooldown [17] is at present not clear.

The current understanding of transport at the level crossings is as follows. Without a level crossing, when the Fermi energy lies in the localised states between two Landau levels, no backscattering is possible, i.e. the Hall resistance is quantised and the longitudinal resistance is zero. At the level crossing however, the gap disappears and one would intuitively expect to measure a finite resistance, but not a spike. However, if the intra-Landau level exchange energy is larger than the inter-Landau level exchange energy, instead of having a continuous mixture of the 2 crossing levels, an infinitesimal amount of disorder [19] already forces the 2D system to break up into macroscopic domains containing either one of these levels [20,21]. The spike in the resistance then originates from backscattering of electrons across the sample *along* the domain walls separating the two levels. At zero temperature the domains are pinned by the random potential fluctuations that cause slight density (and thus filling factor) variations. When the magnetic field is swept, the system is not able to instantaneously reach the thermodynamically stable state and transport shows a hysteresis. Once the temperature becomes comparable to the barrier height separating the metastable states from one another ($\approx$ 350 mK in our samples), the 2DES quickly reaches thermodynamic equilibrium and the hysteresis disappears. Away from integer filling factor, there is already a lot of backscattering possible without any crossing levels, as there is a finite density of extended states (DOS) at the Fermi energy. The crossing of two levels then simply results in a twice larger DOS and thus in an enhanced resistance.

Although the main features of the crossings can be explained with the above model, several puzzling issues remain. In [4] it was noted that no more peaks at Landau level crossings are observed in the high density regime (3.5×10^{15} m$^{-2} < n < 5.2 \times 10^{15}$ m^{-2}). This contrasts to our data at $n = 5.3 \times 10^{15}$ m^{-2}. However, we only observe these peaks if the crossing occurs in the flanks of ρ_{xx} around integer filling and not if the crossing happens in the middle of the ρ_{xx}-minimum. One could argue that since ρ_{xx} becomes zero, the spike should also become tiny as was observed in the composite Fermion ferromagnetic transition [11]. We tried to verify this, but for temperatures up to 600 mK, the spike does not appear. Alternatively, it could be that since at higher density the mobility is also higher (and thus disorder is lower), at the transition the sample breaks up into larger domains, which leads to fewer domain walls and thus to less backscattering. This can however not explain the observation of the spike only in the flanks of the minima near integer filling which seems to suggest that a finite DOS at E_F is required for the observation of a spike. Also the hysteresis of ρ_{xx} at the transition is different in the high density regime. Whereas at low n it is mostly in the amplitude of the spike and only a few mT in its position [4,17], we observe also in the position a large hysteresis (up to 0.1 T).

The spikes and enhanced resistance that mark the various crossings of Landau levels are followed as the sample is tilted in the magnetic field and their

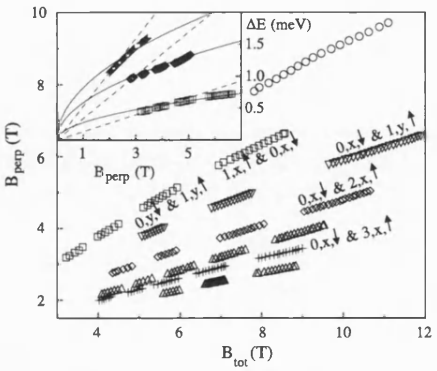

Fig. 4. Position of the various Landau level crossings in the $(B_{\mathrm{tot}}, B_{\mathrm{perp}})$-plane. Inset plots the (non-linear) exchange energy difference for the crossings of LL belonging to the same valley. Same symbols are used as in the main figure.

position in the $(B_{\mathrm{tot}}, B_{\mathrm{perp}})$-plane is plotted in Fig. 4. From the low magnetic field data (not shown) we extract the valley splitting ($\sim$ 0.16 meV/T B_{perp}) and the (low field) g-factor[1] ($\sim 1.93 g_0$). This allows the identification of the crossing levels, a few of which are indicated in Fig. 4 (notation: N, valley, spin; the X-valley is the lowest in energy). Once the levels are identified, their position is measured and the mass and bare g-factor are known, the difference in their exchange energies (ΔE) can be determined. For the $1,\mathrm{x},\uparrow$ and $0,\mathrm{x},\downarrow$ crossing, ΔE equals $\hbar\omega_{\mathrm{c}} - g_0\mu_{\mathrm{B}}B_{\mathrm{tot}}$. Using $g_0 = 1.9$ and $m^* = 0.46m_{\mathrm{e}}$, ΔE for the crossings of Landau levels (LL) from the same valley are plotted in the inset of Fig. 4 with the same symbols as in the main part of the figure. Contrary to [4], ΔE is not a linear function of the perpendicular field. Instead, for the crossings of LL with indices that differ by 1 and 2 (□ and ◇), a $\sqrt{B_{\mathrm{perp}}}$-dependence describes the data much better. For the crossings of LL with an index that differs by 3 (+) this $\sqrt{B_{\mathrm{perp}}}$ is somewhat too weak to produces a good fit. A $\sqrt{B_{\mathrm{perp}}}$-dependence (and not a linear dependence) is actually what one would expect, since the origin of the g-factor enhancement is the Coulomb energy ($e^2/4\pi\varepsilon l_{\mathrm{B}}$), that scales with $\sqrt{B_{\mathrm{perp}}}$. Also the difference in magnitude of the three ΔE branches can be qualitatively understood. The g-factor enhancement is caused by the net number of polarised Landau levels below the Fermi energy and this is 2, 4 and 6 for the branches indicated with □, ◇ and +, respectively. Dividing ΔE by these numbers however, does not lead to one universal curve.

Summarising, we have investigated crossings of Landau levels with opposite spin in high mobility AlAs 2DES in the high density regime by tilted magneto-transport measurements. The crossings are observed as spikes in the resistance appearing in the flanks of the minima around integer filling factor. At low T the position of the spikes is hysteretic (up to 0.1 T at 20 mK). From the position of the crossings in the $(B_{\mathrm{perp}}, B_{\mathrm{tot}})$-plane the difference in exchange energy of the crossing levels is determined and found to be a non linear function of the perpendicular field.

We thank J. Weis for the use of his dilution refrigerator system and BMBF for financial support.

[1] We do not know which in-plane valleys is lowest in energy, but from the extrapolation of the experimentally determined valley splitting in low magnetic fields using the method outlined in Ref. [18], we know that the valley splitting is smaller than the (enhanced) spin splitting.

References

[1] V. Piazza, et al., Nature 402 (1999) 638.
[2] W. Pan, et al., Phys. Rev. B 64 121305(R).
[3] K. Muraki, T. Saku, Y. Hirayama, Phys. Rev. Lett. 87 (2001) 196801.
[4] E.P. de Poortere, et al., Science 290 (2000) 1546.
[5] U. Zeitler, et al., Phys. Rev. Lett. 86 (2001) 866.
[6] J. Jaroszynski, et al., Phys. Rev. Lett. 89 (2002) 266802.
[7] H. Cho, et al., Phys. Rev. Lett. 81 (1998) 2522.
[8] J. Eom, et al., Science 289 (2000) 2320.
[9] J.H. Smet, et al., Phys. Rev. Lett. 86 (2001) 2412.
[10] J.H. Smet, et al., Nature 415 (2002) 281.
[11] S. Kraus, et al., Phys. Rev. Lett. 89 (2002) 266801.
[12] T.P. Smith III, et al., Surf. Sci. 196 (1988) 287.
[13] T.S. Lay, et al., Appl. Phys. Lett. 62 (1993) 3120.
[14] H.W. van Kesteren, et al., Phys. Rev. Lett. 61 (1988) 129.
[15] E.P. de Poortere, et al., Appl. Phys. Lett. 80 (2002) 1583.
[16] Y. Yaish, et al., Phys. Rev. Lett. 84 (2000) 4954.
[17] E.P. de Poortere, cond-mat/0304507 (2003).
[18] Y.P. Shkolnikov, et al., Phys. Rev. Lett. 89 (2002) 226805.
[19] Y. Imry, S.K. Ma, Phys. Rev. Lett. 35 (1975) 1399.
[20] T. Jungwirth, A.H. MacDonald, Phys. Rev. B 64 (2000) 035305.
[21] T. Jungwirth, et al., Phys. Rev. Lett. 87 (2001) 216801.

Acknowledgements

I would like to express my gratitude to my host supervisor, Professor Werner Dietsche, whose expertise, understanding, and patience, added considerably to my experience at the Max Planck Institute. I appreciate his vast knowledge in many areas and his assistance in writing this thesis.

I would like to thank Professor Simon Bending, my supervisor at the University of Bath, for visiting me regularly in Germany and for being at the right place at the right time when I needed his support.

Thanks also goes to Professor K.von Klitzing for allowing me to conduct my research in his group.

I would like to specially thank Dr. Sjoerd Lok for the assistance he provided at all levels of the research project and for his efforts in the horrible task of correcting and editing this thesis.

I want to thank R. Muehle for teaching me how to fabricate LMIS AuSiBe FIB sources.

I must also acknowledge my colleagues in Stuttgart: Dr Stefan Kraus, for putting up with me in the office and for his help in deciphering the wonders of German culture; Dr Omar Stern, for his companionship and good cheer both at work and play; Fred Schwerdt, for never allowing there to be a dull moment in the strange world of molecular beam epitaxy and Dr Afif Siddiki for his friendship and great music.

I would like to thank Eleonora Storace for all her help and for making me get this thesis finished.

Finally, I want to thank my parents who have supported me all my life.

Curriculum Vitae

- **2001-2005**
  Doctor of Philosophy
  Max-Planck-Institute for Solid State Research.
  Thesis Title: Novel Physics in Two Dimensional Charge Carrier Structures.

- **1997-2001**
  Bachelor of Science with honours in physics with placement year.
  University of Bath.
  Final year project: Hall Sensor Gradiometer for Magnetocardiography.

- **1997**
  University Foundation Year
  Coventry University

- **1990-1997**
  Military Service

- **1986-1989**
  GCSE Examinations
  Markethill High School